UNIVERSITY of CALIFORNIA
Santa Barbara

MOCVD Growth Technologies for Applications in AlGaN/GaN High Electron Mobility Transistors

A dissertation submitted in partial satisfaction of the
requirements for the degree of

Doctor of Philosophy

in

Electrical and Computer Engineering

by

Sten J. Heikman

Committee in charge:

Professor Umesh K. Mishra, Co - Chair
Professor Steven P. DenBaars, Co - Chair
Professor Evelyn L. Hu
Professor Shuji Nakamura

September 2002

The dissertation of Sten J. Heikman is approved:

_____

_____

_____

_____

Chair

September 2002

MOCVD Growth Technologies for Applications in AlGaN/GaN

High Electron Mobility Transistors

by

Sten J. Heikman

Acknowledgements

IT has been a very rewarding experience to be part of the highly successful nitride research program at UCSB. My advisor Prof. Umesh Mishra has been a truly awesome boss, giving good advice and many ideas, while at the same time giving me freedom to explore my own ideas. My co-advisor Prof. Steven DenBaars early on gave me the opportunity to work in his world class MOCVD lab, and to get deeply involved with the hardware, which has fit my practical inclination well. I was also fortunate to have on my Ph.D committee Prof. Evelyn Hu and Prof. Shuji Nakamura, who are two of the corner-stones of the nitride research community.

MOCVD growth of HEMTs has been an integral part of my work, and I am very grateful to Dr. Stacia Keller, fellow HEMT grower and mentor, who has taught me almost everything I know about MOCVD growth. Many thanks to other growers and processing experts: Dario, Rob, Likun, Naiqian, Alessandro, Lee, Paidi, Hongtao, Gia, Rama, Ching-Hui, Jane, YiFeng, Yulia, and DJ. I would also like to thank my fellow MOCVD growers, with whom I have spent countless late growth nights, and/or countless hours of machine trouble shooting and repairs: Stacia, Tom, Tal, Huili, Ilan, Andreas, Monica, Gia, Mike, Brendan, James, Paul, Hugues, Yae, Eric, Jon, and Patrick. Thanks also to Brian; without his technical skills the lab would not function. Thanks are also due to Jack, Brian T, Bob, Neil, and Mike A, in the cleanroom, and to Cathy, Lee, and Masika, for all things administrative.

Many thanks go to my office mates (in no particular order): James, Rob, Vicki, Dan, DJ, Bruce, Likun, Huili, Pengcheng, Jim, Nadia, Young Tim, Ariel, Hongtao, Naiqian, Dario, Paolo, Ale, Yingda, Ilan, Chris, Matt, Michael, Jason, Joe, Haijiang, Mary, Justin, Amir, Can, Lee, Rama, Gia, Amit, Prashant, and Peter, who all have contributed to a chaotic but creative working environment. I have been told that the office is very quiet when I am not there myself, so perhaps *I* have been the source of all the chaos…

I would like to acknowledge Dr. Frank Bertram and Prof. Jurgen Christen, at Otto-von-Guericke Universität Magdeburg, Germany, for the cathodoluminescence measurements on one of my samples.

Finally I would like to acknowledge the financial support from the Air Force Office of Scientific Research and the Office of Naval Research.

Last but not least: I am deeply indebted to my friends, family, and my girlfriend Birgit, for support, encouragement, and understanding.

Curriculum Vitæ

Sten J. Heikman

EDUCATION

Civilingenjör, Applied Physics and Electrical Engineering, Linköping University, Sweden, December 1998

Master of Science in Electrical and Computer Engineering, University of Massachusetts, Amherst, September 1998

Doctor of Philosophy in Electrical and Computer Engineering, University of California, Santa Barbara, September 2002 (expected)

PROFESSIONAL EMPLOYMENT

1998 - 2002 Research assistant, Department of Electrical and Computer Engineering, University of California, Santa Barbara

PUBLICATIONS

S. Heikman, S. Keller, T. Mates, S. P. DenBaars, and U. K. Mishra, "Growth and characteristics of Fe-doped GaN", *to be published in Journal of Crystal Growth*, 2002.

S. Heikman, S. Keller, S. P. DenBaars, and U. K. Mishra, "Growth of Fe-doped semi-insulating GaN by metalorganic chemical vapor deposition", *Applied Physics Letters*, vol. 81, no. 3, p. 439, 2002.

S. Keller, **S. Heikman**, L. Shen, I. P. Smorchkova, S. P. DenBaars, and U. K. Mishra, "GaN-GaN junctions with ultrathin AlN interlayers: Expanding heterojunction design", *Applied Physics Letters*, vol. 80, no. 23, p. 4387, 2002.

A. Jimnez, D. Buttari, D. Jena, R. Coffie, **S. Heikman**, N. Q. Zhang, L. Shen, E. Calleja, E. Munoz, J. Speck, and U. K. Mishra, "Effect of p-doped overlayer thickness on RF-dispersion in GaN junction FETs", *IEEE Electron Device Letters*, vol. 23, no. 6, p. 306, 2002.

D. Buttari, A. Chini, G. Meneghesso, E. Zanoni, B. Moran, **S. Heikman**, N. Q. Zhang, L. Shen, R. Coffie, S. P. DenBaars, and U. K. Mishra, "Systematic characterization of Cl_2 reactive ion etching for improved ohmics in AlGaN/GaN HEMTs", *IEEE Electron Device Letters*, vol. 23, no. 2, p. 76, 2002.

L. Shen, I. P. Smochkova, D. S. Green, **S. Heikman**, and U. K. Mishra, "GaN planar-doped-barrier electron emitter with piezoelectric surface barrier lowering", p. 223,

2001. Proceedings of the 14th International Vacuum Microelectronics Conference Davis, CA, USA 12-16 Aug. 2001 Piscataway, NJ, USA IEEE.

S. Keller, **S. Heikman**, I. Ben-Yaacov, L. Shen, S. P. Den Baars, and U. K. Mishra, "Indium surfactant assisted growth of AlN/GaN heterostructures by metal-organic chemical vapor deposition", *Physica Status Solidi A*, vol. 188, no. 2, p. 775, 2001.

S. Heikman, S. Keller, B. Moran, R. Coffie, S. P. DenBaars, and U. K. Mishra, "Mass transport regrowth of GaN for ohmic contacts to AlGaN/GaN", *Physica Status Solidi A*, vol. 188, no. 1, p. 355, 2001.

S. Keller, **S. Heikman**, I. Ben-Yaacov, L. Shen, S. P. DenBaars, and U. K. Mishra, "Indium-surfactant-assisted growth of high-mobility AlN/GaN multilayer structures by metalorganic chemical vapor deposition", *Applied Physics Letters*, vol. 79, no. 21, p. 3449, 2001.

I. P. Smorchkova, L. Chen, T. Mates, L. Shen, **S. Heikman**, B. Moran, S. Keller, S. P. DenBaars, J. S. Speck, and U. K. Mishra, "AlN/GaN and (Al,Ga)N/AlN/GaN two-dimensional electron gas structures grown by plasma-assisted molecular-beam epitaxy", *Journal of Applied Physics*, vol. 90, no. 10, p. 5196, 2001.

D. S. Green, **S. Heikman**, B. Heying, P. R. Tavernier, J. S. Speck, D. R. Clarke, S. P. Den Baars, and U. K. Mishra, "Molecular beam epitaxy of InGaN/GaN heterostructures for green luminescence", p. 371, 2000. Proceedings of the IEEE Twenty-Seventh International Symposium on Compound Semiconductors Monterey, CA, USA 2-5 Oct. 2000 Piscataway, NJ, USA IEEE.

L. Shen, **S. Heikman**, B. Moran, R. Coffie, N. Q. Zhang, D. Buttari, I. P. Smorchkova, S. Keller, S. P. DenBaars, and U. K. Mishra, "AlGaN/AlN/GaN high-power microwave HEMT", *IEEE Electron Device Letters*, vol. 22, no. 10, p. 457, 2001.

H. Xing, S. Keller, Y. F. Wu, L. McCarthy, I. P. Smorchkova, D. Buttari, R. Coffie, D. S. Green, G. Parish, **S. Heikman**, L. Shen, N. Zhang, J. J. Xu, B. P. Keller, S. P. DenBaars, and U. K. Mishra, "Gallium nitride based transistors", *Journal of Physics: Condensed Matter*, vol. 13, no. 32, p. 7139, 2001.

S. Heikman, S. Keller, S. P. DenBaars, and U. K. Mishra, "Mass transport regrowth of GaN for ohmic contacts to AlGaN/GaN", *Applied Physics Letters*, vol. 78, no. 19, p. 2876, 2001.

S. Heikman, S. P. DenBaars, and U. K. Mishra, "Selective area mass transport regrowth of gallium nitride", *Japanese Journal of Applied Physics, Part 1*, vol. 40, no. 2A, p. 565, 2001.

J. J. Xu, S. Keller, G. Parish, **S. Heikman**, U. K. Mishra, and R. A. York, "A 3-10-GHz GaN-based flip-chip integrated broad-band power amplifier", *IEEE Transac-*

tions on Microwave Theory and Techniques, vol. 48, no. 12, p. 2573, 2000.

I. P. Smorchkova, S. Keller, **S. Heikman**, C. R. Elsass, B. Heying, P. Fini, J. S. Speck, and U. K. Mishra, "Two-dimensional electron-gas AlN/GaN heterostructures with extremely thin AlN barriers", *Applied Physics Letters*, vol. 77, no. 24, pp. 3998–4000, 2000.

N. Q. Zhang, S. Keller, G. Parish, **S. Heikman**, S. P. DenBaars, and U. K. Mishra, "High breakdown GaN HEMT with overlapping gate structure", *IEEE Electron Device Letters*, vol. 21, no. 9, p. 421, 2000.

J. J. Xu, S. Keller, G. Perish, **S. Heikman**, U. K. Mishra, and R. A. York, "A 3-10 GHz LCR-matched power amplifier using flip-chip mounted AlGaN/GaN HEMTs", vol. 2, p. 959, 2000. IEEE MTT-S International Microwave Symposium Digest Boston, MA, USA 11-16 June 2000 Piscataway, NJ, USA IEEE.

S. Keller, G. Parish, P. T. Fini, **S. Heikman**, C. H. Chen, N. Zhang, S. P. DenBaars, U. K. Mishra, and Y. F. Wu, "Metalorganic chemical vapor deposition of high mobility AlGaN/GaN heterostructures", *Journal of Applied Physics*, vol. 86, no. 10, p. 5850, 1999.

J. J. Xu, W. Yi-Feng, S. Keller, **S. Heikman**, B. J. Thibeault, U. K. Mishra, and R. A. York, "1-8-GHz GaN-based power amplifier using flip-chip bonding", *IEEE Microwave and Guided Wave Letters*, vol. 9, no. 7, p. 277, 1999.

S. Heikman, "Metalorganic chemical vapor deposition of gallium nitride using ammonia and dimethylhydrazine", *unpublished M. Sc. thesis, University of Massachusetts, Amherst*, 1998.

Abstract

MOCVD Growth Technologies for Applications in AlGaN/GaN

High Electron Mobility Transistors

by

Sten J. Heikman

The AlGaN/GaN high electron mobility transistor (HEMT) has evolved tremendously in the last nine years since its first demonstration. However, before commercialization, more work is needed to improve stability, efficiency, and manufacturability. This work is focused on the development and use of selective area growth (SAG) by metalorganic chemical vapor deposition, for new device designs aimed at improving said properties. The growth of the planar AlGaN/GaN device structure is also discussed, with emphasis on the semi-insulating base-layer, and the use of Fe doping to develop a high quality semi-insulating process with improved stability.

'Non-planar SAG' involves a selective etch into the HEMT structure before growth, and allows contact between regrowth and the HEMT channel, which is essential for device applications. Non-planar SAG is studied extensively in this work, with emphasis on the region of interest for devices, close to the regrowth mask. The growth evolution of GaN and AlGaN is studied, as well as AlGaN alloy compo-

sition, and impurity incorporation as a function of temperature and mask material. Due to the non-planar nature of the samples, mass-transport of material may occur during sample heat-up, which needs to be avoided for well-controlled growth in the near-mask region. Mass-transport is also explored as a growth technique of its own, with advantages in simplicity and speed, since it does not require a Ga precursor.

Several device designs, utilizing both mass-transport growth and regular non-planar SAG, are implemented, most importantly aimed at reducing the source and drain contact resistance and access resistance. Some of the designs show great potential, and may with some further optimization have a real impact on the next generation devices.

Contents

1 Introduction

IN the last nine years, AlGaN/GaN high electron mobility transistors (HEMT's) have evolved tremendously, from the first modest demonstration in 1993,[1] to today's high performance devices that are approaching commercialization. The AlGaN/GaN system offers many advantages over Si and other III-V compound semiconductors, for high power high frequency operation. The high conduction band discontinuity, in combination with strong polarization effects,[2] gives rise to large sheet charge densities at the AlGaN/GaN interface, well in excess of 1×10^{13} cm^{-2} for a 35% Al composition. The high bandgaps of GaN and AlGaN provide for large breakdown fields, and the thermal stability of the materials allows for a high temperature of operation. These excellent properties have led to the demonstrations of devices, with current densities as high as 1.5 A/mm,[3] breakdown voltages over 1 kV,[4], power densities of 11.2 W/mm at 10 GHz,[5] and total pulsed total output powers of 50 W.[6]

The devices have demonstrated impressive performance in the basic figures of merit, but they typically lack the finer properties needed for many applications.

Crude output power may be sufficient for some applications, but for the very important area of communications, properties such as efficiency, linearity, and low noise, are as important as output power. There is currently a shift in focus in the AlGaN/GaN HEMT research community towards these issues, as they need to be addressed before the technology can be commercialized.

1.1 This Work

The unifying theme of this dissertation is the development and study of the AlGaN/GaN HEMT from a growth perspective. Metalorganic chemical vapor deposition (MOCVD) was used exclusively as growth technique, due to the maturity of this technique in general, and the precedent set by this technique for HEMT growths at UCSB. Part of the work consisted of the growth of the planar HEMT structures, building on many years of experience of the UCSB HEMT team, but the HEMT growth forms a relatively small part of this dissertation, since many aspects have already been covered in various publications over the years.

The main focus of this dissertation is the development and use of selective area growth techniques, for use as a design tool to improve AlGaN/GaN HEMTs. The current nitride processing technology, in particular wet etching, is far behind the GaAs and InP technologies, which has for long limited the kinds of device designs that can be fabricated in the AlGaN/GaN system. The use of selective area growth (SAG) in HEMT fabrication allows more advanced device designs to be im-

plemented, which may be required to solve the issues that presently stand in the way of device commercialization.

The SAG technique of most interest for HEMT applications, called 'non-planar SAG' in this dissertation, involves a selective etch into the HEMT structure, before the SAG is performed. Non-planar SAG allows direct contact between the regrown material and the device channel through the etched sidewall. Non-planar SAG is studied extensively in this work, with particular emphasis on the properties of the region closest to the regrowth mask, since this is the region of most interest for HEMT applications. Mass-transport effects, which may occur during sample heat-up, are also studied, not only as a by-product of non-planar SAG, but also as an interesting growth technique of its own. The development of the non-planar SAG and the mass-transport growth, is aimed towards HEMT applications, but it can also be regarded as stand-alone basic research.

Part of this work was also to apply the developed growth techniques to actual device applications. A number of shortcomings in today's AlGaN/GaN HEMTs are identified, and various device designs involving SAG are implemented to address the problems. Some of the designs show great potential, and may have a real impact on the next generation devices, with some further optimization. The devices also serve to illustrate concepts, showing what is important in device design, and sets the path for more streamlined fabrication processes to be developed in the future.

There is a strong emphasis on experimental work in this dissertation, a necessity

due to the topic chosen, and due to the relative immaturity of the nitride materials.

1.2 Related Research

At UCSB we have the relatively unique position of being very strong in both material growth of nitride semiconductors, and in device processing and understanding of devices properties. This combination is necessary to undertake the kind of work presented in this dissertation, and this is why previously very little work has been done in this field.

So far, a majority of the work on selective area growth of GaN has been focused on epitaxial lateral overgrowth (ELO) techniques for dislocation reduction, resulting in a wealth of knowledge. Regular SAG of GaN (on planar samples) has, since its first demonstrations,[7, 8] resulted in various 3-dimensional structures, including hexagonal pyramids,[9] optical waveguides,[10] and hexagonal microprisms.[11] SAG of AlGaN has also been demonstrated,[8, 12, 13, 14, 15] but the selectivity has in some cases been reported to be poor.

Non-planar SAG of GaN and AlGaN has been used for fabrication of buried-ridge laser diodes.[12, 13] In addition, non-planar SAG of n^+-GaN for ohmic contact formation to AlGaN/GaN HEMTs has been demonstrated at UCSB,[16, 17] and elsewhere.[18] However, to date there has been no reports on detailed characterization of the growths, and on the occurrence of mass-transport growth associated

with non-planar SAG. In the InP and GaAs material systems on the other hand, non-planar SAG is relatively well studied, as reported in references [19, 20, 21] for example.

1.3 Dissertation Synopsis

In Chapter 2, the growth of planar AlGaN/GaN HEMT structures on sapphire is discussed. Since many aspects of the HEMT growths are routine by now, and have been covered in other publications,[22] only the novel aspects, contributed as part of this work, are covered in detail. Specifically, the work on the semi-insulating base-layer is reported, including the history, the problems, the solution, and characterization of the results. As a result of transferring the growth process to a larger scale growth system, a high quality semi-insulating base-layer could no longer be grown. In response to this, Fe doping of GaN was developed to enable reproducible growth of high quality semi-insulating films. The doping behavior of Fe was characterized, and the electrical activity of the dopant was investigated. Finally, the performance of HEMTs grown using the newly developed semi-insulating process is discussed.

As the non-planar selective area growth work was commenced, it was discovered that mass-transport effects can cause growth at the mask edges during short anneals, without external supply of Ga growth species; this is the topic of Chapter 3. The principle behind the mass-transport growth is discussed, and experiments are per-

formed to clarify the mechanisms. The influence of the annealing conditions on the growth morphology is studied, along with the lateral range of the effect. Furthermore, autodoping effects from the SiO_2 mask is investigated, and quantified, with two separate techniques.

The regular non-planar selective area growth, performed under conditions to avoid mass-transport growth, is reported in Chapter 4. The emphasis of the experiments is to understand the properties of the growth near the mesa edge, since this is the region of most importance for HEMT applications. The growth evolution of GaN and $Al_{0.1}Ga_{0.9}N$ near the mask edge is studied, by interrupted growths. Lateral variations in the alloy composition of the AlGaN is also investigated, with cathodoluminescence microscopy. Using two different TLM techniques, the lateral distribution of impurities, for Si-doped, and nominally undoped growth, is investigated, and the influence of the growth temperature and the mask material is clarified. A low-profile selective area growth technique is also developed, in which the benefits of both non-planar SAG, and mass-transport growth, are combined, resulting in a large lateral extent of the growth, and no vertical growth above the original sample surface.

In Chapter 5, the developed mass-transport growth and non-planar SAG are put to use in device applications. A number of issues with today's AlGaN/GaN HEMTs are discussed, and various device designs involving SAG are suggested to solve the problems. The most important suggestion is the reduction of source and drain ac-

cess/contact resistances, to address the soft current saturation, high knee voltage, g_m compression, and low f_T. The resistance reduction is accomplished with selective area growth of high conductivity material in the contact regions, and part of the access regions. The concept is demonstrated by both mass-transport growth, and low-profile SAG, showing contact resistances down to 0.3 Ωmm, with the possibility of extreme lateral scaling. Other device applications include drain regrowth, for control of RF dispersion, and AlGaN source regrowth, for increased f_T by hot electron injection into the HEMT channel. The drain regrowth device worked as intended, but suffered from low breakdown voltages. The source regrowth device did not show the intended improvement in f_T, probably due to large parasitic source and drain resistances. One problem, that hampered the progress of the device work, was a high resistance associated with current transport from the regrowth regions into the HEMT channel. The problem occurred inconsistently, and was in part related to photo-resist residues under the regrowth mask. At the end of Chapter 5, suggestions for future work are presented, in particular on how to address the problem with the current transport across the regrowth edge.

In Chapter 6, the future work suggested in the previous chapters is summarized. Some additional ideas are also presented, which are not directly related to AlGaN/GaN HEMTs, the focus of this dissertation, but are still of scientific interest.

References

[1] M. A. Khan, A. Bhattarai, J. N. Kuznia, and D. T. Olson *Appl. Phys. Lett.*, vol. 63, p. 1214, 1993.

[2] O. Ambacher, B. Foutz, J. Smart, J. R. Shealy, N. G. Weimann, K. Chu, M. Murphy, A. J. Sierakowski, W. J. Schaff, L. F. Eastman, R. Dimitrov, A. Mitchell, and M. Stutzmann *J. Appl. Phys.*, vol. 87, p. 334, 2000.

[3] J. S. Moon, M. Micovic, P. Janke, P. Hashimoto, W. S. Wong, R. D. Widman, L. McCray, A. Kurdoghlian, and C. Nguyen *Electron. Lett.*, vol. 37, p. 528, 2001.

[4] N. Q. Zhang, B. Moran, S. P. DenBaars, U. K. Mishra, X. W. Wang, and T. P. Ma *Physica Status Solidi A*, vol. 188, p. 213, 2001.

[5] J. R. Shealy, V. Kaper, V. Tilak, T. Prunty, J. A. Smart, B. Green, and L. F. Eastman *Journal of Physics: Condensed Matter*, vol. 14, p. 3499, 2002.

[6] J. W. Palmour, S. T. Sheppard, R. P. Smith, S. T. Allen, W. L. Pribble, T. J. Smith, Z. Ring, J. J. Sumakeris, A. W. Saxler, and J. W. Milligan *IEDM Tech. Digest*, p. 385, 2001.

[7] M. Nagahara, S. Miyoshi, H. Yaguchi, K. Onabe, Y. Shiraki, and R. Ito *Japan. J. Appl. Phys.*, vol. 33, p. 694, 1993.

[8] Y. Kato, S. Kitamura, K. Hiramatsu, and N. Sawaki *J. Crystal Growth*, vol. 144, p. 133, 1994.

[9] R. D. Underwood, D. Kapolnek, B. P. Keller, S. Keller, S. P. DenBaars, and U. K. Mishra *Solid State Electron.*, vol. 41, p. 243, 1997.

[10] T. Tanaka, K. Uchida, A. Watanabe, and S. Minagawa *Appl. Phys. Lett.*, vol. 68, p. 976, 1996.

[11] T. Akasaka, Y. Kobayashi, S. Ando, and N. Kobayashi *Appl. Phys. Lett.*, vol. 71, p. 2196, 1997.

[12] T. Asano, K. Yanashima, T. Asatsuma, T. Hino, T. Yamaguchi, S. Tomiya, K. Funato, T. Kobayashi, and M. Ikeda *Phys. Stat. Sol. A*, vol. 176, p. 23, 1999.

[13] M. Yang, M. Cho, C. Kim, J. Yi, J. Jeon, S. Khym, M. Kim, Y. Choi, S. J. Leem, and Y. H. Lee *J. Crystal Growth*, vol. 226, p. 73, 2001.

[14] N. Maeda, T. Saitoh, K. Tusubaki, and N. Kobayashi *Phys. Stat. Sol. A*, vol. 188, p. 223, 2001.

[15] T. Kato, Y. Honda, Y. Kawaguchi, M. Yamagushi, and N. Sawaki *Jpn. J. Appl. Phys.*, vol. 40, p. 1896, 2001.

[16] C. H. Chen, S. Keller, G. Parish, R. Vetury, P. Kozodoy, E. L. Hu, S. P. DenBaars, and U. K. Mishra *Appl. Phys. Lett.*, vol. 73, p. 3147, 1998.

[17] Y.-F. Wu, D. Kapolnek, P. Kozodoy, B. Thibeault, S. Keller, B. Keller, S. Denbaars, and U. Mishra in *IEEE Twenty-Fourth International Symposium on Compound Semiconductors*, (San Diego, CA, USA), p. 431, IEEE, 1998.

[18] H. Kawai, M. Hara, F. Nakamura, and S. Imanaga *Electron. Lett.*, vol. 34, p. 592, 1998.

[19] R. T. Huang, C. L. Jiang, A. Appelbaum, D. Renner, and S. W. Zehr *J. Electron. Mater.*, vol. 19, p. 1313, 1990.

[20] K. Nakai, T. Sanada, and S. Yamakoshi *J. Crystal Growth*, vol. 93, p. 248, 1988.

[21] K. Goto, M. Takemi, T. Miura, A. Takemoto, and Y. Mihashi *J. Electron. Mater.*, vol. 25, p. 411, 1996.

[22] S. Keller, Y. F. Wu, G. Parish, N. Zhang, J. J. Xu, B. P. Keller, S. P. DenBaars, and U. K. Mishra *IEEE Trans. Electron Dev.*, vol. 48, p. 552, 2001.

2

High Electron Mobility Transistors

DEVICE applications, towards which this entire dissertation is aimed, required a steady supply of device quality material. Since AlGaN/GaN high electron mobility transistor (HEMT) wafers were not commercially available, they had to be grown locally. This chapter provides the background on the growth of the HEMT material by MOCVD.

HEMT growth is a continuous project at UCSB, which has been going on for many years, resulting in many great advances. At the time I joined the HEMT team, high performance HEMTs were routinely grown, however, on a relatively small scale. I got involved in the effort of scaling up the process, to satisfy the needs of the general HEMT fabrication program at UCSB.

After providing some background in §2.1, the problems encountered in scaling up the process are described. Specifically, the growth of semi-insulating GaN on sapphire turned out to be a problem, as outlined in §2.2. In §2.3 a new approach to solve the problem is presented, involving Fe doping of GaN. Finally, in §2.4, the performance of the HEMTs utilizing the newly developed semi-insulating process is

discussed.

I would like to credit a few people for their help with the work in this chapter. Dr. Stacia Keller, who has been heading the AlGaN/GaN HEMT growth effort at UCSB for many years, helped out with some of the growths, and provided me with guidance and many valuable ideas. Furthermore, I performed very little of the device processing myself; it was mostly done by Dr. Dario Buttari, Robert Coffie, Naiqian Zhang, Likun Shen, and Alessandro Chini.

2.1 Introduction

The growth of AlGaN/GaN HEMTs is in principle very simple. The structure consists only of a thin AlGaN layer on top of a semi-insulating GaN base-layer. A 2-dimensional electron gas (2DEG) accumulates at the AlGaN/GaN interface, attracted by a strong polarization difference at the interface.[1] No n-type doping is necessary to achieve a 2DEG; the origin of the charge is still a controversy, but it most likely originates from surface donors.[2] The growth of the AlGaN is relatively well established, and has been published previously,[3] and will consequently not be discussed here. The growth of the semi-insulating base-layer on the other hand is non-trivial, and it will be the main focus of this chapter.

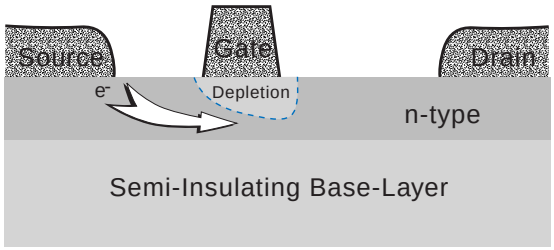

Figure 2.1: Field effect transistor showing the pinch-off of the channel between the gate depletion region, and the semi-insulating base-layer.

2.1.1 The Need for a Semi-Insulating Base-Layer

The family of field effect transistors (FETs) consists of many device types, including the junction FET, metal semi-conductor FET (MESFET), metal oxide semiconductor FET (MOSFET), and the heterostructure FET (HFET), also known as the high electron mobility transistor (HEMT). In all FETs, a positive bias on the drain electrode causes electrons to flow from the source electrode to the drain electrode. The gate serves to modulate the current, through a bias-dependent depletion of the channel region, as illustrated in Fig. 2.1. By fully depleting the device channel, the current can be pinched-off. To enable a sharp pinch-off, the conductivity between source and drain, through the underlying base-layer, must be eliminated. For standard Si MOSFETs, the base-layer is of the opposite conductivity type to the source and drain implant regions, forming an pnp (or npn) junction below pinch-off that blocks the current. This is possible in the MOSFET because the channel is created by charge inversion, but for other FET structures this option is not available. Instead,

the base-layer must serve as a back barrier, against which the gate can deplete the channel. This requires the base-layer to be either of the conductivity type opposite to the channel, or to be semi-insulating. For RF operation, a conductive base-layer is undesirable, since capacitive coupling between contact pads and the buffer constitute large parasitic elements, which degrade RF performance. The best choice is therefore a semi-insulating base-layer.

2.1.2 Substrate Choice

The development of the selective area growth techniques, and their applications to HEMTs, consumed large quantities of HEMT material, and therefore the cost of producing the HEMT wafers had to be minimized. Through the development of AlGaN/GaN HEMTs, two substrates have dominated: sapphire and SiC. Sapphire is the traditional substrate for MOCVD of GaN, and it is reasonably cheap at $\sim$ \$100 per 2" wafer. The drawback of sapphire is its low thermal conductivity, which makes it difficult to dissipate heat from devices during operation. The alternative substrate, SiC, was for long not suitable for RF devices, due to electrical conductivity in the substrate. In 1999 the first semi-insulating SiC substrates became available, and SiC has since become the leading substrate for high-power devices, due to its high thermal conductivity. High cost is the major drawback for SiC substrates; currently semi-insulating 4H-SiC retails for $\sim$ \$4000 per 2" wafer, which is 40 times the cost of sapphire. The price will probably go down over time, as the yield of the

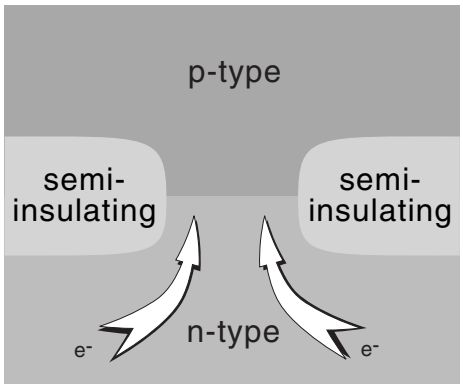

Figure 2.2: Vertical device structures utilizing semi-insulating material to achieve lateral current confinement. Examples include buried ridge lasers, and the current aperture vertical electron transistor.[4]

process goes up, the demand increases, and as more manufacturers emerge on the market. However, for the work described in this dissertation, and other HEMT work performed at UCSB at the same time, it was decided that most growths would have to be performed on sapphire substrate; only the power-critical applications would be grown on SiC substrate.

2.2 Semi-Insulating GaN

Semi-insulating GaN is the foundation of many nitride based device structures. Lateral conduction devices, such as the AlGaN/GaN HEMT, require semi-insulating material beneath the device structure to enable sharp current pinch-off. In vertical devices, semi-insulating material may be used for lateral current confinement, as illustrated in Fig. 2.2. Examples of such devices include the AlGaN/GaN current

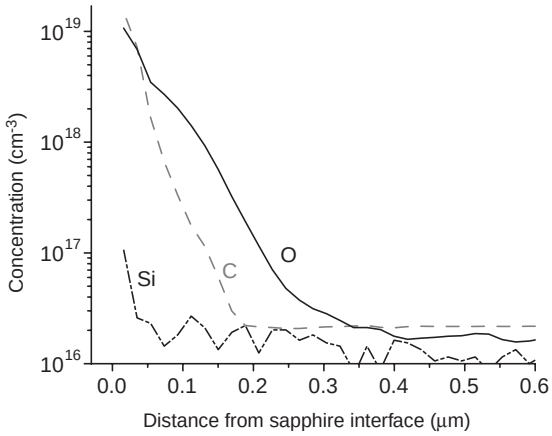

Figure 2.3: SIMS plot of a GaN film grown on sapphire substrate, in the region near the sapphire interface.

aperture vertical transistor,[4] and within opto-electronic applications, lateral current confinement is needed for buried ridge laser structures. Moreover, for electrical characterization test structures, *e.g.* Hall effect measurement structures, the tested layer has to be isolated from underlying conduction paths. A p-n junction is commonly used for isolation, but a semi-insulating base-layer is preferable since it eliminates the problem of dislocation leakage[5] to the base-layer.

2.2.1 GaN on Sapphire

Nominally undoped GaN grown by MOCVD on sapphire substrate typically shows n-type conductivity, presumably due to doping by residual oxygen impurities.[6, 7] Fig. 2.3 shows a SIMS profile obtained from a GaN film, near the sapphire interface. During the initial stages of GaN growth on sapphire, the substrate itself is a

source of oxygen through thermal etching and/or diffusion, which results in a highly oxygen doped region near the sapphire interface.[8, 9] Away from the sapphire interface, the n-type impurity levels are relatively low, below the SIMS detection limit. To grow semi-insulating material the residual donors have to be compensated by acceptor states, commonly done either by introducing high densities of threading dislocations, or by choosing growth conditions that result in high levels of carbon impurities, leading to the formation of deep acceptor states.[10, 11] High dislocation densities are often undesirable in the structure on top of the semi-insulating base layer, either because of the direct effect on transport properties,[12] or because of the effect on surface morphology[13] and consequently the interface roughness of any heterostructures that may be present. Excessive dislocation densities in the active structure can be avoided if the base layer is compensated with acceptor like point defects, such as carbon, instead of extended defects. Unfortunately, the growth conditions that favor carbon impurity incorporation, e. g. low pressure or low temperature, typically also lead to high dislocation densities.

2.2.2 History of Semi-Insulating GaN at UCSB

For the first several years of the AlGaN/GaN HEMT work at UCSB, the semi-insulating buffers were grown on sapphire, utilizing enhanced dislocation densities, to compensate the residual impurities. The nitride MOCVD reactor used at this time had certain properties that made growth of semi-insulating material relatively easy.

The most important characteristic was a relatively fast coalescence rate during the initial 3D-island phase of the growth on sapphire. The oxygen impurity originating from the sapphire is limited to the 3D-island growth phase, assuming the oxygen is produced from thermal etching of the sapphire, which only occurs while parts of the sapphire surface is exposed. An early coalescence therefore results in less oxygen at the sapphire interface, requiring less dislocations to achieve semi-insulating properties.

A few years ago, in response to an increased need for HEMT material, a new reactor with higher wafer capacity was installed. When starting to characterize the new reactor, it soon became clear that the new reactor had quite different properties compared to the old reactor. For example, the coalescence rate was much slower than in the old reactor, causing increased incorporation of oxygen at the sapphire interface. When attempting to transfer the previously developed semi-insulating process, from the old reactor, severe problems were encountered. To achieve semi-insulating GaN, much higher dislocation densities were needed, and the process was very sensitive to drifts in the reactor conditions. The dislocations affected the surface morphology of the films, resulting in rough AlGaN/GaN heterojunctions, and consequently low 2DEG mobilities. Fabricated devices showed poor properties, in particular with respect to RF power performance. The experience from the previous reactor was that HEMTs with heavily over-compensated buffers showed poor RF power performance, presumably due to trapping in the buffer. The inherent problem in using

dislocations for compensation is that they propagate throughout the film, while they are only needed in the region close to the sapphire interface. Consequently, semi-insulating films grown in the new reactor, where a high concentration of compensating centers were needed near the sapphire interface, were heavily overcompensated away from the substrate, which explains the poor RF power performance.

For growth of semi-insulating GaN on sapphire in the new reactor, there was a clear need for a stable point-defect acceptor that could be incorporated readily during the initial stages of growth, without having to invoke low pressure growth, or other conditions that favor carbon incorporation. In the following section, the use of Fe as a compensating point defect is investigated, with the goal of producing high quality semi-insulating films.

Growth of GaN on semi-insulating 4H-SiC substrates has also been performed in the new reactor. The films usually turn out semi-insulating, without any special technique, due to the absence of oxygen in the substrate. Given the ease of the semi-insulating process on SiC substrate, compared to on sapphire, it was tempting to abandon the HEMT project on sapphire, but the cost issue motivated further work on the semi-insulating process on sapphire.

2.3 Fe-doping of GaN

Transition metals such as Cr and Fe have been used to render III-V semi-conductors semi-insulating, for many years.[14, 15] As for GaN, few reports of Fe or Cr doping exist in the literature. In 1979 Monemar *et al.*[16] grew GaN samples by hydride vapor-phase epitaxy that were contaminated by Fe and Cr from reactor hardware and/or sources, and they were found to be electrically insulating. Photoluminescence spectroscopy and other characterization later found a 1.30 eV transition associated with the Fe impurity in these samples.[17] In two separate studies the $Fe^{3+/2+}$ acceptor level has been proposed to be located 2.6 eV and 3.17 eV above the valence-band maximum, respectively.[18, 19] Recently, growth of Fe doped GaN by molecular beam epitaxy, for ferromagnetic purposes, has been reported.[20, 21] Although promising for growth of semi-insulating films, no reports of intentional Fe doping of GaN were found in the literature. In this section, *ferrocene* was explored as a precursor to grow Fe doped GaN by MOCVD, based on the success of this precursor for Fe doping of InP.[15]

2.3.1 Experiment

The samples in this study were grown by MOCVD using the precursors TMGa, ammonia, and ferrocene (Cp_2Fe, bis(cyclopentadienyl)iron). The growth conditions, unless otherwise noted, were as follows: reactor pressure 1 atm, growth temper-

ature 1050°C, ammonia partial pressure 0.5 atm, H_2 carrier gas, and growth rate ~ 2 μm/hr. The ferrocene bubbler was kept at +30°C, a temperature at which the ferrocene is a solid. The ferrocene partial pressures were calculated based on vapor pressure data assuming 100% vapor saturation in the bubbler.[22] The Fe concentration in the samples was characterized by secondary ion mass spectrometry (SIMS), using O_2^+ ion species, and was calibrated to a GaN:Fe implant standard. The detection limit was $\sim 3\times10^{15}$ cm^{-3}. For resistivity measurements a thin (20 nm) $Al_{0.3}Ga_{0.7}N$ cap was deposited on the GaN film. Indium contacts were formed, after which the AlGaN layer between the contacts was etched off with reactive ion etching. The presence of the AlGaN under the contact metal induces a two-dimensional electron gas at the AlGaN/GaN interface,[1] which ensures an ohmic contact. Without the AlGaN it is difficult to form ohmic contacts to highly resistive material, and reliable measurements cannot be made.

2.3.2 Fe Incorporation

The Fe concentration in the grown crystal, as measured by SIMS, was investigated as a function of the input ferrocene partial pressure. For the three partial pressures 0.16 mPa, 0.80 mPa, and 2.4 mPa, the Fe concentration was 7.1×10^{17} cm^{-3}, 3.5×10^{18} cm^{-3}, and 9.9×10^{18} cm^{-3}, respectively, following an approximately linear relation (see Fig. 2.4). Another set of samples was grown to study the effect of Fe doping on surface morphology. The doping concentrations were calculated by ex-

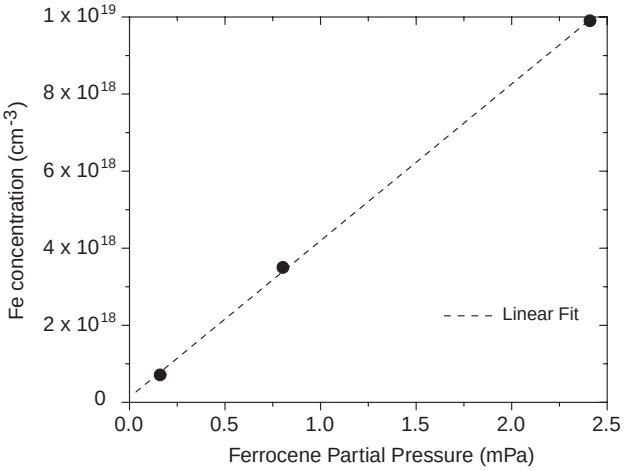

Figure 2.4: Fe concentration in the GaN film versus ferrocene partial pressure.

---

trapolating the linear dependence in Fig. 2.4. For doping levels up to 1.7×10^{19} cm^{-3} the samples showed a specular surface in Nomarsky microscopy. For the sample shown in Fig. 2.5 the doping level was increased to 1.7×10^{20} cm^{-3}, which resulted in a rough surface.

The effect of the GaN growth rate was studied next. As the growth rate and the ferrocene partial pressure were both reduced by a factor of 2, the Fe concentration in the crystal remained essentially unchanged. This behavior is indicative of a mass transport limited dopant incorporation process.[23] To explore the influence of other growth conditions on the Fe incorporation, the following variations to the previously described standard growth conditions were employed: low reactor pressure (0.13 atm), lower temperature (1010°C and 970°C), and lower ammonia partial

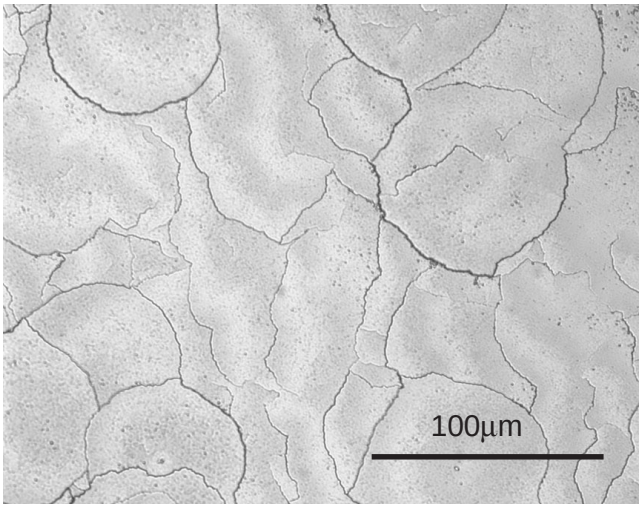

Figure 2.5: GaN sample Fe doped to 1.7×10^{20} cm^{-3}.

---

pressure (0.08 atm). The various growth conditions resulted in only small changes in the Fe concentration, all of which could be accounted for by considering the small changes in GaN growth rate that resulted from the modified growth conditions.

An approximate doping efficiency could be calculated from the Fe concentrations measured by SIMS. A segregation coefficient k_{seg} was defined by relating the Fe/Ga concentrations in the crystal to the ferrocene/TMGa gas phase partial pressures, as:

$$k_{seg} = \frac{[Fe]/N_{Ga}}{p_{Cp_2Fe}/p_{TMGa}} \tag{2.3.1}$$

where N_{Ga} = 4.4×10^{22} cm^{-3}. Using this definition, the experimental data gave a k_{seg} of approximately 0.6, which is close to the ideal value of 1 for dopants with mass transport limited incorporation. The small discrepancy may be a consequence

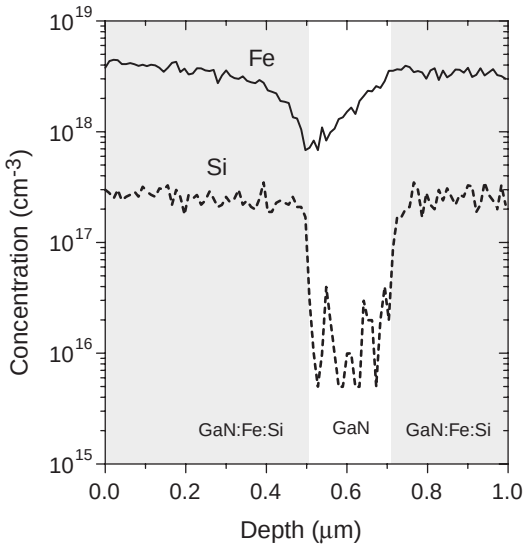

Figure 2.6: SIMS profile of Fe modulation doped structure, showing prominent memory effects. The Fe doped layers were co-doped with Si to mark the positions.

---

of a lower gas-phase diffusion coefficient of ferrocene compared to TMGa, in combination with incomplete vapor saturation of the gas flowing through the ferrocene bubbler, a known problem for solid metalorganic sources.

2.3.3 Fe Doping Response

The SIMS analysis of the Fe doped samples revealed a slow concentration response to the ferrocene injection. Fig. 2.6 shows the SIMS profile of a portion of a Fe doped sample, where the ferrocene flow was interrupted for a period of time. The Fe doped layers were co-doped with low concentrations of Si to mark the position of the layers. The Si had a well-defined profile, with a sharp turn-on and turn-off.

The Fe concentration on the other hand changed gradually as the ferrocene flow was interrupted, and as the ferrocene was turned back on, the Fe concentration in the film increased gradually towards its previous value. The observed slow doping response is very similar to what is observed for Mg doping of GaN by MOCVD, using the precursor Cp_2Mg.[24] Proposed mechanisms for the slow Mg doping response include build-up of Mg (or Mg compounds) on reactor walls and plumbing (memory effect), and build-up of a Mg layer 'riding' the surface of the growing film (Mg surface segregation).[25]

To investigate the origins of the slow Fe doping response, a systematic study was launched, including several Fe doping experiments, which were characterized by SIMS. Prior to the experiments, no Fe doped films had been grown for several weeks in the reactor, ensuring that no residual iron was present in the reactor chamber at the start of the experiments. An undoped GaN base layer was first prepared on sapphire substrate, and was cut into pieces. The individual pieces were then subject to multiple growths, both Fe doped and undoped. The details of the experiments, and the results, will be discussed next.

To investigate the the role of the reactor environment, a nominally undoped GaN film was grown on an undoped base layer, right after a 0.6 μm GaN:Fe film had been grown in the reactor on a *different* sample. SIMS of the undoped sample showed that the Fe concentration was below the detection limit throughout the whole sample. Since there was no increase in the Fe concentration in the regrown region, it can be

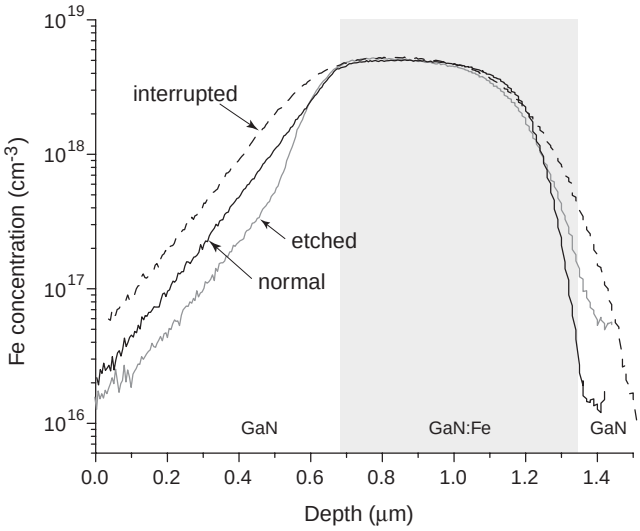

Figure 2.7: SIMS profiles of Fe doped GaN layers followed by nominally undoped layers. The slow Fe concentration turn-off was improved by treating the sample in acids between the growth of the GaN:Fe layer and the nominally undoped layer. The broadening of the 'interrupted' profile is believed to be an artifact of the SIMS measurement.

concluded that the reactor environment is not a source of Fe doping after GaN:Fe growth. Observe that no cleaning or baking of the reactor between the GaN:Fe growth and the undoped GaN growth was necessary to obtain this result.

To further investigate the slow Fe doping response, an interrupted growth was performed on a sample. The sample received 0.6 μm GaN:Fe growth, was removed from the reactor, and was later reloaded and received another 0.8 μm of nominally undoped GaN growth. In between, the reactor was used to grow undoped GaN on another sample. The SIMS profile of the interrupted growth is shown in Fig. 2.7, labelled 'interrupted'. A slow turn-on and turn-off is evident, similar to the non-interrupted profile 'normal' in Fig. 2.7. The fact that a Fe-tail is present in the nom-

inally undoped region, *after* GaN free of Fe had been grown in the reactor, clearly shows that the source of the Fe during the slow turn-off is the sample itself. The 'interrupted' profile is slightly broader and more rounded than the 'normal' profile, but as will be discussed later, this is probably an artifact of the SIMS measurement due to the depth of this structure in the sample. Another interrupted growth was performed, but this time the sample was treated in acids between the growth of the GaN:Fe layer and the nominally undoped GaN layer. The acid treatment consisted of a 5 minute etch in each of the following concentrated acids: H_2SO_4, HNO_3, H_3PO_4, HCl, and HF. The SIMS profile of this interrupted growth is also included in Fig. 2.7, labelled 'etched'. The Fe concentration shows a more rapid initial Fe turn-off than in the non-interrupted growth, but after a short distance the slope is the same. The purpose of the acid etch was to remove any excess Fe (or Fe containing compounds) that may have been present on the sample surface after the GaN:Fe growth. Since the chemical nature of the Fe on the surface was unknown, many different acids were used, to increase the chance of success. From the improved Fe concentration turn-off it appears that the acid treatment was effective in removing some of the Fe from the surface. Moreover, the experiment clearly shows that the slow Fe concentration turn-off is related to excess Fe accumulated on the sample surface. In another experiment, a GaN:Fe layer was subject to a 5 minute *in-situ* anneal before the growth of a nominally undoped GaN layer. The anneal, performed at 1020°C in an ambient of N_2 and NH_3, was intended to desorb Fe from the sample

surface, but it had no measurable effect on the slow Fe concentration turn-off.

The experiments show that the slow turn-on and turn-off of the Fe concentration is *not* due to adsorption and desorption on the internal surfaces of the reactor. This is in contrast to Mg doping of GaN and GaAs, where this effect, often referred to as 'memory effect', is believed to play an important role.[24, 26] In addition to the memory effect, Mg segregation on the growth surface has also been proposed to explain the slow Mg doping response.[25] For the Fe doping of GaN, I propose that the observed slow turn-on and turn-off of the Fe concentration is exclusively due to Fe segregation on the growth surface. In this model, a Fe containing layer builds up on the surface of the growing film as ferrocene is injected. This layer 'rides' the surface of the growing film, while acting as a Fe source for the film. Before the Fe layer is fully built-up, the Fe incorporation into the film is low, resulting in a slow turn-on of the doping profile. When the ferrocene flow is turned off, the Fe containing layer remains on the surface, continuing to supply Fe doping to the growing film until the layer is depleted, resulting in a Fe tail into the nominally undoped layer.

In addition to surface segregation of Fe, diffusion of Fe could also play a role in the apparent slow turn-on and turn-off of the Fe concentration. From the shape of the Fe doping profiles, some idea of the influence of diffusion can be obtained. For a thin doped layer, buried deep in the layer structure, material on both sides of the doped layer have approximately the same thermal history, i.e. the same time at

elevated temperature. For such a layer, the diffusion of dopants into the surrounding undoped material would result in a symmetric doping profile. The following general trend was observed for the Fe SIMS profiles in all samples: Near the sample surface (within 1 μm) the Fe profiles were well-defined, with the start of the Fe turn-off visible as a kink. However, deep in the sample (4-6 μm) the profiles were more rounded. In Fig. 2.7, the profiles labelled 'normal', 'etched', and 'interrupted' were from structures located at sample depths 1.4 μm, 2.8 μm, and 4.2 μm, respectively. The deepest structure, 'interrupted', showed most rounding, but was still quite asymmetric. At this depth, a nearly symmetric shape would be expected for a diffusion dominated process. The observed rounding of the profiles was probably an artifact of the SIMS measurement. Degradation of the sputter crater, such as increased roughness and inclined sidewalls, with increasing depth, can cause loss of depth resolution, a known problem for sputtering with O_2^+ ion species. The variations in the Fe turn-on present in Fig. 2.7, and the rounded shape of the 'interrupted' profile, are probably caused by this effect. The shape of the Fe doping profiles do not support Fe diffusion as a major contributor to the slow turn-on and turn-off, but Fe diffusion can not be entirely ruled out based on the results presented here. More SIMS profiling and annealing studies are necessary to determine the role, if any, of Fe diffusion.

2.3.4 Electrical Activity of Fe in GaN

Transition metals are well known to form deep levels within the bandgap of semiconductors,[27] and Fe doping is a proven technology for rendering InP semi-insulating. Multiple states within the band gap, originating from the interaction of the iron 3d states and the s- and p-like valence levels of the host semiconductor, have been observed for InP:Fe and GaAs:Fe, as well as for GaN:Fe.[28, 27, 19] In this section, the electrical activity of Fe in GaN is investigated, through a Fe-Si co-doping experiment.

Several 2 μm GaN films were grown, co-doped with Si and Fe. The Si concentration was kept constant at 6.4×10^{17} cm^{-3}, while the Fe concentration was varied between zero and 2.6×10^{18} cm^{-3}. SIMS was performed on one sample, to confirm the Si and Fe concentrations. The Fe concentration was also confirmed by X-ray photoelectron spectroscopy, on a highly Fe doped sample. The films were grown on semi-insulating GaN/sapphire base layers, prepared as described in §2.3.5. Hall effect measurements in the van der Pauw geometry, using In contacts, were performed on the samples. The Hall scattering factor was assumed to be unity. Growing the films on semi-insulating base-layers ensured that only the co-doped films were measured by the Hall measurements. The measured Hall charge and mobility are plotted as a function of the Fe concentration in Fig. 2.8. The sample with no Fe doping showed a charge of 5.4×10^{17} cm^{-3}, which is close to the Si concentration

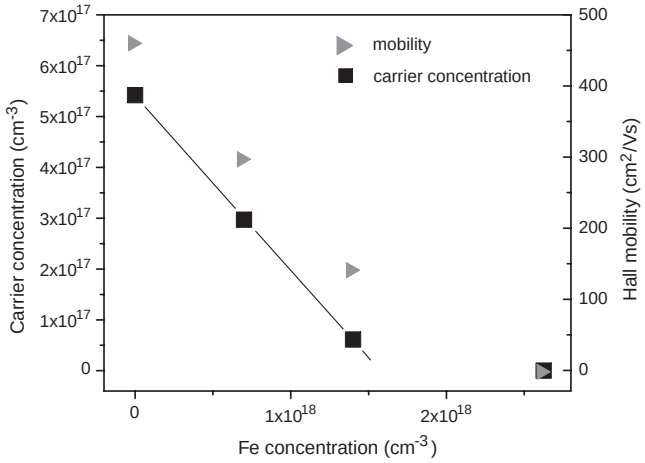

Figure 2.8: Carrier concentration and Hall mobility *vs.* Fe concentration in GaN films codoped with Si and Fe. The Si concentration was kept constant at 6.4×10^{17} cm^{-3}.

6.4×10^{17} cm^{-3} measured by SIMS. The discrepancy may be a sign of light compensation, but it may also be due to the errors in the respective measurements. As Fe was introduced at concentrations 7.0×10^{17} cm^{-3} and 1.4×10^{18} cm^{-3}, the measured charge decreased to 3.0×10^{17} cm^{-3} and 6.1×10^{16} cm^{-3}, respectively. For a Fe concentration of 2.6×10^{18} cm^{-3}, the sample became too resistive to get a reliable Hall measurement. The Hall mobility showed the expected trend; as the compensation increased with the increased Fe concentration, the mobility decreased. Apart from the highly resistive sample, the measured points in Fig. 2.8 fall on a straight line with a negative slope of 0.34. The slope is a measure of how many free electrons are trapped by each Fe atom on average. The fact that the slope is less than one suggests that not all Fe atoms are electrically active in the crystal. Fe atoms could be electrically passive due to an interstitial lattice position, or due to passivation by

native defects or other impurities such as hydrogen. Further experiments on thermal annealing in a hydrogen free atmosphere are needed, to elucidate the compensation mechanism.

In a similar co-doping study of InP, the Fe compensation activity was found to be nearly 100 %.[29] By photoluminescence excitation measurements of GaN:Fe, the deep $Fe^{3+/2+}$ acceptor level has been found to be close to the conduction-band minimum, with a binding energy of (280$\pm$100) meV.[19] If the acceptor level is even closer to the conduction band, in the proximity of the Fermi-level, incomplete ionization of the acceptor level could offer an alternative explanation to the observed less-than-one compensation activity in GaN.

2.3.5 Fe Doped Films on Sapphire Substrate

Based on the overall promising Fe doping results, Fe doped GaN films were grown on sapphire to develop high quality semi-insulating films. The growths were performed using the typical two step process[30] with a low temperature GaN nucleation layer followed by a 2.6 μm thick high temperature (1050°C) GaN layer. An undoped reference sample showed n-type conductivity, with a sheet resistance of 2.6 k$\Omega/\Box$. For the Fe doped samples ferrocene was injected only during the first 0.3 μm of the high temperature growth, since most of the donor impurities are believed to be located near the sapphire interface.[9] Samples with two different ferrocene partial pressures were grown. The sample grown with the lower ferrocene

partial pressure, corresponding to a Fe concentration of 1.7×10^{18} cm^{-3}, had a resistivity of $\sim$ 200 k$\Omega/\Box$. The sample using a higher ferrocene partial pressure, corresponding to 1.3×10^{19} cm^{-3}, showed a very high resistivity of 7×10^{9} $\Omega/\Box$. Since dopant impurities may affect growth morphology and the relative growth rates of various crystal planes,[31, 32] it is possible that the Fe doping may affect the growth mode and alter the structural properties of the film, in particular since the Fe doping was performed during the initial island growth stage.[33] To quantify the influence of the Fe doping on structural properties X-ray diffraction measurements were performed. To get a reliable measure of the structural quality, both symmetric (002) and asymmetric (102) rocking curves (ω-scans) were obtained.[34] The undoped reference sample had a full width at half-maximum (FWHM) of 251 arcsec for the (002) reflection, and a FWHM of 491 arcsec for the (102) reflection. The Fe doped sample (Fe concentration 1.3×10^{18} cm^{-3}) showed very similar values: a FWHM of 253 arcsec for the (002) reflection, and a FWHM of 481 arcsec for the (102) reflection. This shows that the Fe doping did not significantly affect the structural properties of the film. The XRD data indicate an overall high quality film, with threading dislocation densities on the order of 1×10^{9} cm^{-2}. Worth emphasizing is that no Fe doping was necessary in the top 2.3 μm of the film to make the whole structure highly resistive, while the top portion of undoped GaN films grown in our reactor typically have a carrier density on the order of 5×10^{15} cm^{-3}. Although the memory effect of the Fe doping extended the Fe concentration into the nominally

undoped region by about 0.8 μm, the Fe concentration in the remaining part of the layer was below the SIMS detection limit ($\sim 3\times10^{15}$ cm^{-3}), insufficient to compensate the residual donors. Pinning of the Fermi level deep in the film and at the surface may contribute to the high resistivity, by depleting the free carriers.

2.3.6 Summary - Fe Doping

Ferrocene was used as a Fe dopant precursor for MOCVD growth of semi-insulating GaN. The Fe concentration in the film showed a linear dependence on the precursor partial pressure, and was insensitive to growth temperature, pressure, and ammonia partial pressure. Specular films could be achieved with Fe concentrations up to 1.7×10^{19} cm^{-3}. The Fe exhibited slow doping response, which was shown to originate from Fe segregation on the sample surface, rather than from reactor environment related effects, such as adsorption/desorption from reactor walls and plumbing. An improved turn-off behavior was observed when the GaN:Fe sample surface was etched in acids prior to deposition of the subsequent GaN layer. The compensating nature of Fe in GaN was investigated through Si-Fe co-doping experiments, revealing that Fe had a compensating activity of 34 %. A highly resistive (7 G$\Omega/\Box$) GaN on sapphire film was demonstrated, with high crystalline quality. The technique allows growth of semi-insulting GaN without invoking undesirable growth conditions and high dislocation densities.

2.4 HEMTs on Fe Doped Base-Layers

After the successful demonstration of semi-insulating Fe doped GaN films on sapphire substrate, the use of the films as base-layers for HEMT devices was explored. The insulating capability of the Fe-doped was very high, leaving no concerns about current pinch-off. However, other properties pertinent to device operation, in particular the trapping behavior, were unknown. It was known from previous experience, that HEMTs with highly insulating (heavily over-compensated) base-layers showed poor RF power performance, presumably due to trapping in the buffer. Given the highly insulating nature of the Fe doped base-layers, trapping was therefore a big concern.

2.4.1 The First HEMT

The first attempt to grow HEMTs on Fe-doped base-layers resulted in very poor devices. The device structure consisted of $\sim$ 0.6 μm GaN:Fe, followed by 2 μm nominally undoped GaN, and a 20 nm $Al_{0.3}Ga_{0.7}N$ cap layer, as illustrated in Fig. 2.9a. Fig. 2.9b shows the drain I-V characteristics of a fabricated device. The device had not received surface passivation. The current was relatively low, due to a non-optimized AlGaN cap layer. The most striking feature however, was the large difference between the curves obtained in a single sweep, and the curves obtained from repeated sweeps. For repeated sweeps, the current collapsed to about 30% of the

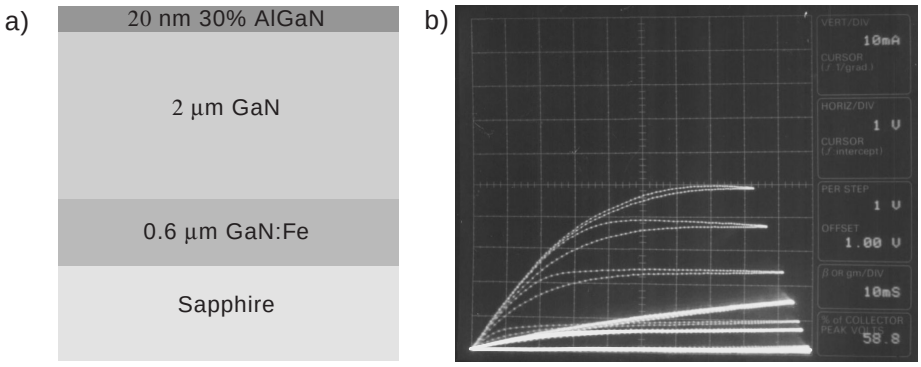

Figure 2.9: The first HEMT on GaN:Fe base-layer. a) The layer structure. b) The plot shows I_{ds} - V_{ds} curves for a device with 3 μm source to drain spacing, 0.7 μm gate length, 75 μm gate width, for V_{gs} from +1 V to -3 V. The difference between single sweep (dotted lines) and repeated sweep (solid lines) shows that the devices suffered from severe current collapse.

starting values, within a few seconds. Current collapse is a consequence of charge trapping; when charge from the channel is trapped, and the response time of the trap is slower than the sweep, the trapped charge can not participate in current transport. In the device, the trap was slower than the 60 Hz sweep frequency, which is very slow. In fact, it took several 10's of seconds for the device current to recover after collapse. The recovery rate was found to be sensitive to sample illumination.

The slow responding trap was initially attributed to the Fe doping in the base-layer. 0.6 μm was actively doped, but due to the slow Fe concentration turn-off, the Fe doping penetrated an additional $\sim$ 0.8 μm into the nominally undoped film, leaving $\sim$ 1.2 μm of undoped GaN below the device active layer. The initial assessment was soon supported by the improvement seen when introducing an AlN electron blocking layer, described in the following section. However, as became clear from

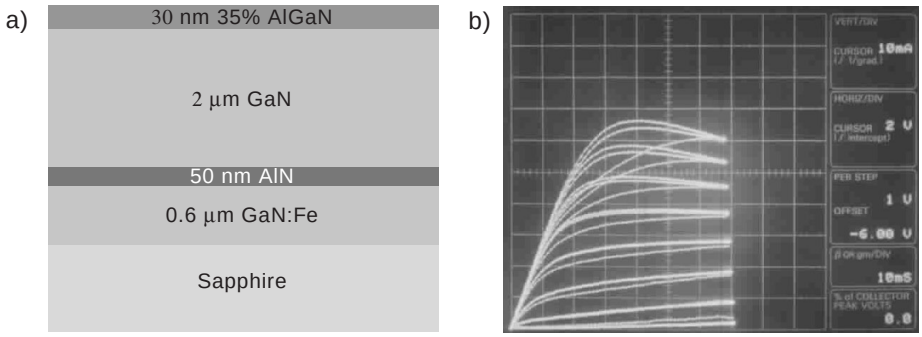

Figure 2.10: a) Improved layer structure, with a 50 nm AlN electron blocking layer, preventing electrons from entering the Fe-doped region. b) Drain I-V characteristics. The maximum current was 1 A/mm, for V_G = 1 V, and a gate width of 75 μm. Devices on this particular sample showed little dispersion for 80 μs pulsed gate operation, but other samples typically showed more dispersion.

---

a more recent study (see §2.4.3), the trapping that leads to current collapse could be eliminated with a SiN surface passivation, which suggests that the responsible trap is located at the surface, excluding Fe as a possible trap.

2.4.2 AlN Interlayer

From the first HEMT devices with GaN:Fe base-layers, it appeared that the deep Fe acceptor in the base layer caused trapping of free carriers from the device channel. To counter this, the layer structure illustrated in Fig. 2.10a was devised. Here, a 50 nm AlN interlayer was inserted between the GaN:Fe layer and the nominally undoped GaN. The purpose of the AlN layer was to provide a high electron barrier, preventing the electrons from reaching the Fe doped layer, where trapping can occur.

Due to a relatively large lattice mismatch to GaN, the 50 nm AlN layer is pre-

sumed to grow nearly relaxed, in a columnar structure. As GaN is deposited on top of the AlN layer, a growth mode similar to the growth on a low temperature nucleation layer is expected, involving discrete nucleation and island coalescence. This growth mode affects the structural properties of the film, and to quantify the effect, X-ray diffraction rocking curves were obtained from the structure. A full-width at half-maximum (FWHM) of 281 arcsec for the (002) reflection and 676 arcsec for the (102) reflection were obtained, compared to values of 253 and 481 arcsec, respectively, for an equivalent film without the AlN layer (see §2.3.5). The increase in the peak widths, notably for the (102) reflection, indicates that the AlN layer results in a film with a higher dislocation density. However, although higher, the FWHM values indicate a film of acceptable structural properties for device applications. Electrically, the structure showed similar properties to structures without the AlN layer. Similar Hall charge and mobility was obtained, and the resistivity of the base layer was very high, with a sheet resistance of $3\times10^{9}\ \Omega/\Box$. One concern with the structure was that a 2DEG would form at the bottom interface of the 50 nm AlN layer, induced by the positive spontaneous polarization charge present at the interface. However, no 2DEG was formed, as indicated by the high sheet resistance, probably due to the presence of Fe doping, in combination with the poor quality of the AlN layer.

Devices fabricated from structures utilizing the AlN interlayer generally showed good performance. For optimized $Al_{0.35}Ga_{0.65}N$ cap layers, maximum currents in

excess of 1 A/mm were achieved, and no current collapse under multiple sweeps was observed. Without surface passivation, the devices would on occasion show minimal dispersion for 80 μs pulsed gate operation, as shown in Fig. 2.10b. However, the devices would more often show some dispersion, with currents reduced to between 70 to 30 % of the DC values. It is currently not clear why dispersion occurs in some cases, but not in others. It may be related to growth conditions, or to processing details, that are currently not under good control. After the proper SiN surface passivation, the dispersion on all devices could be eliminated. RF power measurements were performed on passivated devices, with a load-pull system, at a frequency of 8.2 GHz. At a drain bias of 23 V, the best devices showed a maximum output power of 4.2 W/mm, and a maximum power added efficiency of 39%. These results are among the best reported for AlGaN/GaN HEMTs on sapphire, surpassed only by devices previously produced at UCSB,[3] grown in the 'old reactor' (see §2.2.2).

Based on the overall promising results, the Fe doped base layer, with the 50 nm AlN interlayer, was adopted for the standard HEMT growth process. At the time of writing, it has been in use for one year, and during this time it has proven to be a very robust process, insensitive to variations in growth conditions.

The effectiveness of the AlN interlayer seemed apparent, when comparing devices with the first HEMTs on Fe-doped base-layers (see §2.4.1). It was assumed that surface trapping effects, which can be expected for devices without surface

passivation, would affect both types of structures to the same extent, and that the comparison of unpassivated devices would be fair. As will be seen in the following section, this assumption was probably not correct.

2.4.3 Base-Layer Study

After the Fe-doped base-layer utilizing the AlN interlayer had been in use for nearly a year, the design of the base-layer structure was revisited. One of the motivations was to develop a semi-insulating base-layer of arbitrarily low dislocation density. When deposited on sapphire, the 3D island growth and coalescence sets a lower limit for the dislocation density, but if deposited homoepitaxially on GaN, the limit is set by the dislocation density of the GaN substrate. Possible GaN substrates include thick HVPE layers deposited on sapphire. The AlN interlayer, which is part of the standard process, introduces additional dislocations in the GaN layer grown on top, and would therefore make growth on low dislocation density GaN substrates pointless. With the goal of eliminating the AlN interlayer, a study was launched exploring alternative structures, that can be grown pseudomorphically on GaN.

Base-Layer Structures

Several HEMT structures were grown, with different base-layers, and were processed into devices. The structures are illustrated in Fig. 2.11. The structure labelled *A* was a GaN film on sapphire, with the first 0.3 μm Fe doped, similar to the

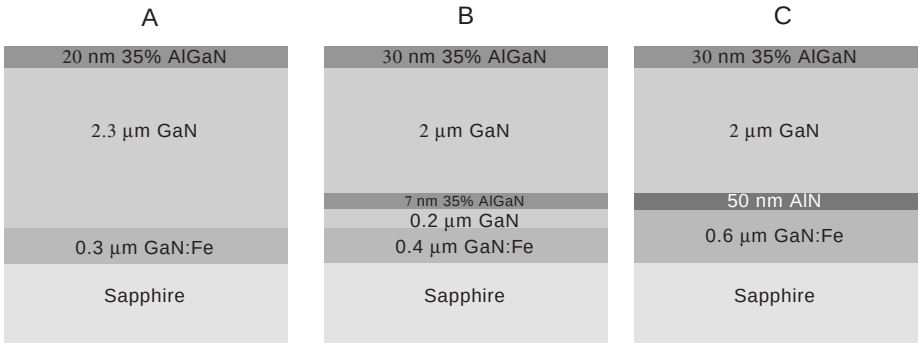

Figure 2.11: HEMT structures with three different base-layer structures. Structure *A* contained only Fe doped GaN, structure *B* contained a 7 nm $Al_{0.35}Ga_{0.65}N$ layer, and structure *C* was the standard structure with a 50 nm AlN interlayer.

---

first HEMT with Fe-doped base-layer, presented in §2.4.1. In structure *B*, a 7 nm $Al_{0.35}Ga_{0.65}N$ layer was inserted, 0.2 μm above a 0.4 μm Fe doped layer located at the sapphire interface. Structure *C* is the standard HEMT structure, containing a 50 nm AlN interlayer, as described in the previous section. Structure *B* was chosen as a compromise between structure *A* and *C*. The 7 nm $Al_{0.35}Ga_{0.65}N$ layer is thin enough to grow fully strained on the underlying GaN layer, and should therefore not give rise to any additional dislocations. The thickness was chosen to cause a shift in the conduction and valence band of about 2 eV, induced by the difference in spontaneous and piezoelectric polarization between the GaN and the $Al_{0.35}Ga_{0.65}N$. Fig. 2.12 shows the band diagrams of structures *A* and *B*. The position of the Fermi level in the semi-insulating GaN:Fe layer is currently not known; for the band diagrams the Fermi level was assumed to be pinned 0.5 eV from the conduction band, based on publications proposing the $Fe^{3+/2+}$ acceptor level to be located much closer

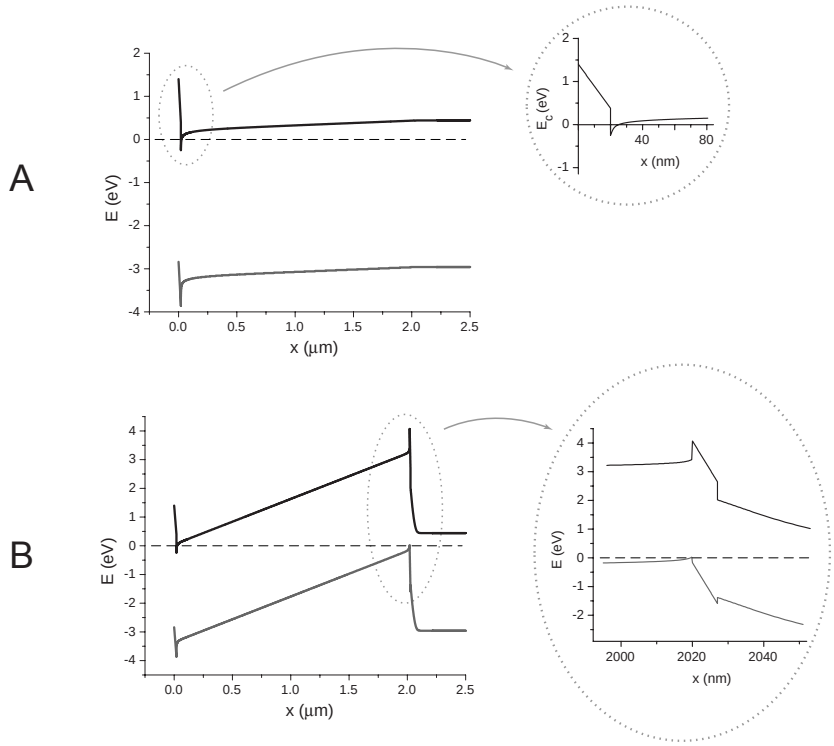

Figure 2.12: Band diagrams of HEMTs with two different base-layer structures. Structure *A* consisted of Fe doped GaN, followed by 2.3 μm undoped GaN, and structure *B* contained a 7 nm $Al_{0.35}Ga_{0.65}N$ layer close to the Fe doped GaN. The Fermi-level has been assumed to be pinned 0.5 eV from the conduction band in the semi-insulating Fe doped GaN.

---

to the conduction-band minimum than to the valence-band maximum.[18, 19] Both structures show the formation of a 2DEG at the top heterojunction, induced by the strong polarization discontinuity. Structure *A* has essentially flat bands in the base-layer, while the polarization of the 7 nm AlGaN in structure *B* gives rise to a $\sim$ 2 eV upward shift in the bands. The exact position of the bands depend on the position of the Fermi level in the semi-insulating region, and on how strongly the Fermi level is pinned. The band diagram of structure *C* is difficult to draw, since the electrical

properties of the 50 nm AlN layer are largely unknown.

At first, the thickness of the $Al_{0.35}Ga_{0.65}N$ cap layer was the same for all three structures, 30 nm. However, during the device processing, specifically during the rapid thermal anneal for the ohmic contact formation, epilayer cracking problems were encountered for structure *A*. No cracking occurred for structures *B* and *C*. The cracking problem was solved by reducing the thickness of the $Al_{0.35}Ga_{0.65}N$ cap layer to 20 nm for structure *A*. The cracking issue is indicative of different strain states in the different structures. It is reasonable that structure *C* would have a different strain state than structure *A*, since the AlN changes the growth mode and introduces dislocations, but it is unclear why structure *B*, which differs from structure *A* only in the 7 nm $Al_{0.35}Ga_{0.65}N$ layer, would have a different strain state. It can be speculated that the 7 nm $Al_{0.35}Ga_{0.65}N$, or the following GaN, did not grow *truly* pseudomorphically.

The Hall data of the structures were similar, with charges around 1.5×10^{13} cm^{-2}, and mobilities around 1500 cm^2/Vs. These relatively high values were achieved by inserting a thin (0.5 nm) AlN at the AlGaN/GaN interface (not shown in Fig. 2.11).[35] After the $Al_{0.35}Ga_{0.65}N$ thickness of structure *A* was reduced to 20 nm, the charge was reduced accordingly.

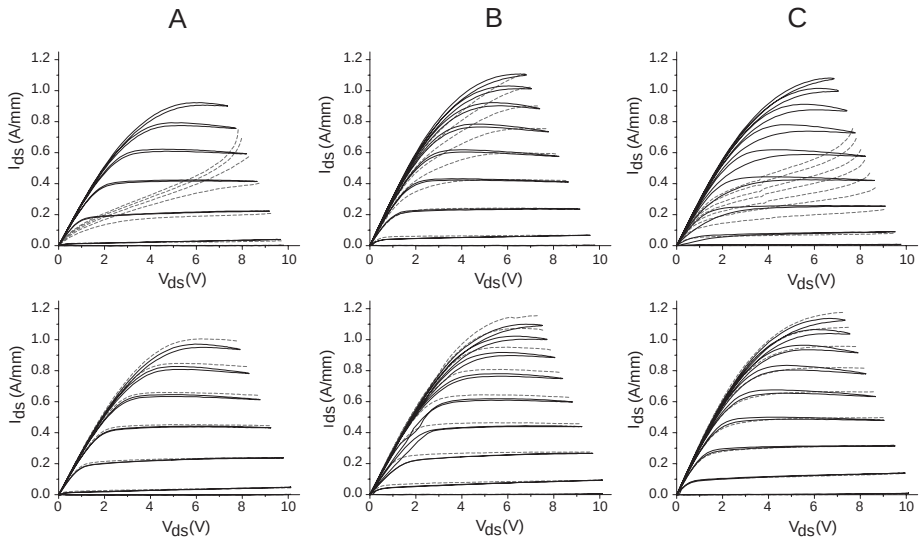

Figure 2.13: Drain I-V characteristics of devices with three different base-layers. The upper plots show the characteristics without SiN passivation, and the lower plots show the characteristics with passivation. The solid lines are the continuous sweeps, while the dashed lines correspond to 80 μs pulsed gate operation.

Drain Characteristics and Gate Lag

Fig. 2.13 shows the I-V characteristics of devices fabricated from the three structures with different base-layers. Without the SiN passivation, the structure *B* (with a 7 nm $Al_{0.35}Ga_{0.65}N$ layer) showed best performance, with only little dispersion detected at 80 μs pulsed gate operation. Structures *A* and *C* however, showed large dispersion without passivation. Structure *A* experienced some current collapse for repeated sweeps, but to less of a degree than the device discussed in §2.4.1 (also with a plain GaN:Fe base-layer). *With* SiN passivation, all samples performed about equally, and structure *A* no longer showed current collapse. Overall, the maximum

current was lower in structure *A*, and the transconductance was higher, but that was merely an effect of the thinner $Al_{0.35}Ga_{0.65}N$ cap layer, and the lower channel charge that this results in.

Drain Lag

Measurements of I-V characteristics with a pulsed gate, know as 'gate lag' measurements, have been established to be most sensitive to surface trapping effects.[36, 37, 38, 39] 'Drain lag' measurements on the other hand, are known to be more sensitive to trapping in the base-layer. For the quantification of the different base-layers, drain-lag measurements were therefore performed. The drain lag measurement, which essentially is the response of the drain current to a drain bias pulse, was performed as illustrated in Fig. 2.14. The gate bias is kept constant throughout the measurement. The measurement starts with the device biased at a low V_{ds}, in the linear region of the I-V plane (1). The drain bias is then pulsed to a high voltage (2), well into the saturation region, and is kept at this voltage for a short time. At the high bias, hot electrons are generated in the device channel, specifically in the high field region between the gate and drain, and they may be trapped in deep centers located throughout the structure. If trapping occurs, and the time constant of the trap is long, the steady state charge in the channel is decreased, leading to a lowered current (3). As the drain bias is lowered to the initial low value (4), any charge that was trapped gradually returns to the channel, causing a slow recovery of the current

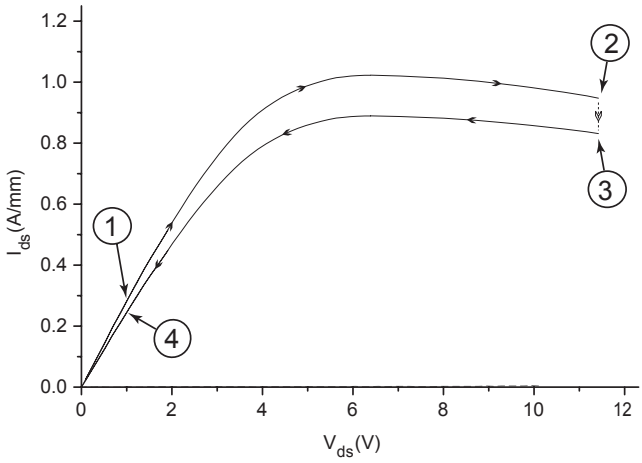

Figure 2.14: Illustration of a drain-lag measurement. The measurement starts with a low V_{ds} (1), which is then pulsed into the saturation region (2), and is held at high voltage for a short time while some current collapse occurs (3). As V_{ds} is lowered to the starting value (4), the current recovers gradually from the collapse.

to its starting value. By recording the current as it recovers, the effect of trapping can be quantified. Current collapse for repeated sweeps, as observed for structure *A* and for the first Fe-doped HEMT (§2.4.1), is caused by the same mechanism as the drain-lag, and can therefore be quantified with drain-lag measurements.

One problem with the drain-lag measurement is that device heating has the same effect on the current as charge trapping does, and it can not easily be distinguished. However, in ref. [36] the thermal effects have been assigned to drain current transients of a very short time scale (6 μs), so by considering the drain current response on a longer time scale, the thermal effects can be ignored.

Fig. 2.15 shows the results of drain lag measurements, performed on devices fabricated from the three structures illustrated in Fig. 2.11. The grey lines are results

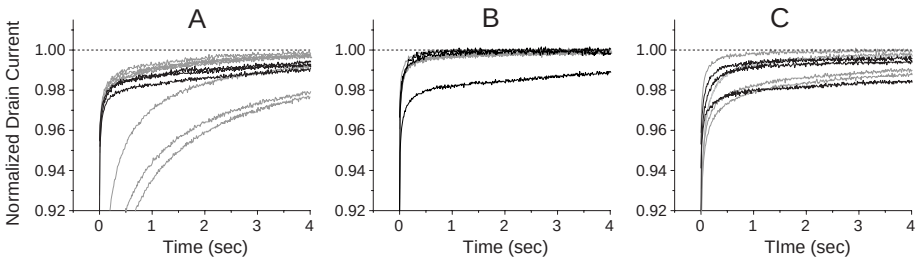

Figure 2.15: Drain-lag measurements on three different device structures. The currents are normalized to the fully recovered currents, measured $\sim$ 1 min after the drain pulse. The multiple lines per plot corresponds to measurements on different dies. The black lines are measurements on passivated devices, and the grey lines are measurements on unpassivated devices.

obtained on unpassivated devices, and the black lines are results from SiN passivated devices. The multiple lines correspond to measurements on different locations on each sample. The plots show the current recovery after a pulse in the drain voltage, and the currents are normalized to the fully recovered current (measured $\sim$ 1 min after the pulse). The conditions were: V_{gs} = 0 V, $V_{ds,initial}$ = 0.1 V, $V_{ds,pulse}$ = 10 V, and pulse duration 2 sec. Severe drain lag was not observed in any of the measurements; the current stayed above 90 % for all three samples. However, structure *A*, the plain Fe-doped structure, showed significant drain lag before passivation, with some variation over the sample, but with SiN passivation the drain lag was reduced, and was more uniform. Structures *B* and *C* were relatively uniform, and showed the same behavior with and without passivation. Overall, structure *B* showed the least amount of drain lag, with the current staying above 99 % for all but one measurements.

Microwave power measurements could unfortunately not be performed on the

samples in this study, due to low breakdown voltages associated with the SiN passivation used at the time.

Discussion

From the measurements it is clear that the traps causing drain-lag are not only located in the base-layer, as suggested in the literature. For example, structure *A* experienced improved drain-lag upon surface passivation, which would indicate that some of the responsible traps were located on the surface. After surface passivation, which should eliminate the effect of the surface traps, the three structures still showed some variation in drain-lag. The remaining variation is therefore attributed to trapping in the base-layer, and it can be concluded that structure *B*, with a 7 nm $Al_{0.35}Ga_{0.65}N$ layer in the base-layer, was most efficient in removing bulk trapping.

When considering the results of the gate lag measurements (see Fig. 2.13), the results are puzzling. The three structures differ only in the base-layer, but they still show drastically different gate lag properties for unpassivated devices. The gate lag is eliminated with surface passivation in all cases, which indicates that the trapping occurred at the surface. The apparent contradiction is that the base-layer structure seems to affect the surface properties of the device. It is not clear if this trend is real; it may be due to uncontrolled variations in the device fabrication or in the growth process, a commonly occurring problem, that at the present time has not been solved or understood. If the trend is real, one possibility is that the base-layer structures are

affecting surface properties through the strain in the films. As was indicated by the epilayer cracking problem mentioned earlier, the three structures had different strain states, and strain has previously been proposed to explain the dispersion phenomena in AlGaN/GaN HEMTs.[40] To further clarify the influence of the base layer on device properties, a more thorough study will have to be undertaken.

The base-layer study was not fully conclusive, but for the purpose of developing a low dislocation density process, it was a success. The best sample, structure *B*, does not introduce additional dislocations, since it only contains a 7 nm $Al_{0.35}Ga_{0.65}N$ layer. In fact, the process was successfully applied for the growth of a HEMT structure on a free-standing GaN wafer produced by HVPE, while maintaining a low dislocation density. The device will not be described here, but it can be mentioned that it had good properties, such as low dispersion, no current collapse, and good pinch-off.

2.5 Discussion and Future Work

2.5.1 Fe Doping

Ferrocene was found to be an efficient precursor for Fe doping of GaN, capable of rendering GaN films on sapphire highly insulating. The doping incorporation was well behaved, except for a slow concentration turn-on and turn-off. For semi-insulating GaN base-layers, the Fe doping works well, and the slow doping re-

sponse is not a problem, so no further doping studies are necessary. For new types of base-layers, requiring a sharp doping concentration turn-off, or for general scientific curiosity, I can suggest a few more aspects to investigate.

To conclusively determine the role of Fe diffusion, if any, in the apparent slow doping response, annealing studies of Fe doped samples can be performed, followed by SIMS profiling. The anneals have to be performed for very long durations, at regular growth temperatures or above. To protect the sample surface during the anneal, the samples have to be covered with a suitable masking material, for example AlN.

In the work presented previously it was shown that a wet-etch in suitable acids can improve the slow Fe concentration turn-off somewhat. It would be interesting to do a similar experiment, with reactive ion etching, where the top 10 - 20 nm of the Fe doped layer would be etched off before the following nominally undoped GaN growth was started. The wet-etch was only partially effective, but a dry-etch, that actually removes some of the GaN as well, may be more effective in removing Fe-containing compounds from the sample surface. As for the slow turn-on, the effects of short ferrocene pre-flows could be investigated. By depositing an appropriate amount of Fe on the sample surface before the growth of the Fe doped layer is started, it is conceivable that the turn-on could be improved.

2.5.2 HEMT Base-Layers

The base-layer study described in §2.4.3 was inconclusive, and left some important questions unanswered. A more thorough study needs to be undertaken. Important for such a study is that several identical samples of each kind are grown and processed, to determine if the observed trends are real, or just an effect of random growth and processing fluctuations. The microwave power performance, in particular output power and power added efficiency, needs to be characterized on all samples, since this has historically been the parameter most sensitive to changes in the device structure. Strain estimates, through wafer curvature measurements, should also be performed, as there have been indications that strain can affect the device properties. Depending on the specific application, other device properties, such as noise figures, or linearity, could also be measured, to aid in identifying the optimum base-layer structure.

References

[1] O. Ambacher, B. Foutz, J. Smart, J. R. Shealy, N. G. Weimann, K. Chu, M. Murphy, A. J. Sierakowski, W. J. Schaff, L. F. Eastman, R. Dimitrov, A. Mitchell, and M. Stutzmann *J. Appl. Phys.*, vol. 87, p. 334, 2000.

[2] J. P. Ibbetson, P. T. Fini, K. D. Ness, S. P. DenBaars, J. S. Speck, and U. K. Mishra *Appl. Phys. Lett.*, vol. 77, p. 250, 2000.

[3] S. Keller, Y. F. Wu, G. Parish, N. Zhang, J. J. Xu, B. P. Keller, S. P. DenBaars, and U. K. Mishra *IEEE Trans. Electron Dev.*, vol. 48, p. 552, 2001.

[4] I. Ben-Yaacov, Y. K. Kwang, S. Heikman, S. P. DenBaars, and U. K. Mishra *submitted to Electron Device Letters*, 2002.

[5] P. Kozodoy, J. P. Ibbetson, H. Marchand, P. T. Fini, S. Keller, J. S. Speck, S. P. DenBaars, and U. K. Mishra *Appl. Phys. Lett.*, vol. 73, p. 975, 1998.

[6] W. Seifert, R. Franzheld, E. Butter, H. Sobotta, and V. Riede *Crystal Res. Tech.*, vol. 18, p. 383, 1983.

[7] C. Wetzel, T. Suski, J. W. Ager III, E. R. Weber, E. E. Haller, S. Fischer, B. K. Meyer, R. J. Molnar, and P. Perlin *Phys. Rev. Lett.*, vol. 78, p. 3923, 1997.

[8] D. C. Look and R. J. Molnar *Appl. Phys. Lett.*, vol. 70, p. 3377, 1997.

[9] M. G. Cheong, K. S. Kim, C. S. Oh, N. W. Namgung, G. M. Yang, C. H. Hong, K. Y. Lim, E. K. Suh, K. S. Nahm, J. J. Lee, D. H. Lim, and A. Yoshikawa *Appl. Phys. Lett.*, vol. 77, p. 2557, 2000.

[10] T. Ogino and M. Aoki *Jpn. J. Appl. Phys.*, vol. 19, p. 2395, 1980.

[11] C. Y. Hwang, M. J. Schurman, W. E. Mayo, Y. C. Lu, R. A. Stall, and T. Salagaj *J. Electron. Mater.*, vol. 26, p. 243, 1997.

[12] N. G. Weimann, L. F. Eastman, D. Doppalapudi, H. M. Ng, and T. D. Moustakas *J. Appl. Phys.*, vol. 83, p. 3656, 1998.

[13] B. Heying, E. J. Tarsa, C. R. Elsass, P. Fini, S. P. DenBaars, and J. S. Speck *J. Appl. Phys.*, vol. 85, p. 6470, 1999.

[14] P. L. Hoyt and R. W. Haisty *J. Electrochem. Soc.*, vol. 113, p. 296, 1966.

[15] J. A. Long, V. G. Riggs, and W. D. Johnston, Jr. *J. Crystal Growth*, vol. 69, p. 10, 1984.

[16] B. Monemar and O. Lagerstedt *J. Appl. Phys.*, vol. 50, p. 6480, 1979.

[17] K. Maier, M. Kunzer, U. Kaufmann, J. Schneider, B. Monemar, I. Akasaki, and H. Amano *Materials Science Forum*, vol. 143-147, p. 93, 1994.

[18] J. Baur, K. Maier, M. Kunzer, U. Kaufmann, J. Schneider, H. Amano, I. Akasaki, T. Detchprohm, and K. Hiramatsu *Appl. Phys. Lett.*, vol. 64, p. 857, 1994.

[19] R. Heitz, P. Maxim, L. Eckey, P. Thurian, A. Hoffmann, I. Broser, K. Pressel, and B. K. Meyer *Physical Review B*, vol. 55, p. 4382, 1997.

[20] H. Akinaga, S. Németh, J. De Boeck, L. Nistor, H. Bender, G. Borghs, H. Ofuchi, and M. Oshima *Appl. Phys. Lett.*, vol. 77, p. 4377, 2000.

[21] S. Kuwabara, T. Kondo, T. Chikyow, P. Ahmet, and H. Munekata *Jpn. J. Appl. Phys.*, vol. 40, p. L724, 2001.

[22] J. T. S. Andrews and E. F. Westrum, Jr. *J. Organometallic Chem.*, vol. 17, p. 349, 1969.

[23] B. Stringfellow in *Organometallic Vapor-Phase Epitaxy: Theory and Practice*, p. 91, San Diego, CA: Academic Press, 2nd ed., 1999.

[24] Y. Ohba and A. Hatano *J. Crystal Growth*, vol. 145, p. 214, 1994.

[25] H. Xing, T. Mates, P. Kozodoy, H. J. Yu, S. Keller, S. P. DenBaars, and U. K. Mishra *submitted to Jpn. J. Appl. Phys.*, 2002.

[26] T. F. Kuech, P. J. Wang, M. A. Tischler, R. Potemski, G. J. Scilla, and F. Cardone *J. Crystal Growth*, vol. 93, p. 624, 1988.

[27] L. A. Hemstreet *Phys. Rev. B*, vol. 22, p. 4590, 1980.

[28] S. Fung, R. J. Nicholas, and R. A. Stradling *J. Phys. C*, vol. 12, p. 5145, 1979.

[29] D. Robein, C. Kazmierski, A. M. Pougnet, and B. Rose *J. Crystal Growth*, vol. 108, p. 554, 1991.

[30] B. P. Keller, S. Keller, D. Kapolnek, W. N. Jiang, Y. F. Wu, H. Masui, X. H. Wu, B. Heying, J. S. Speck, U. K. Mishra, and S. P. DenBaars *J. Electron Mater.*, vol. 24, p. 1707, 1992.

[31] H. Lahrèche, P. Vennéguès, B. Beaumont, and P. Gibart *J. Crystal Growth*, vol. 205, p. 245, 1999.

[32] B. Beaumont, S. Haffouz, and P. Gibart *Appl. Phys. Lett.*, vol. 72, p. 921, 1998.

[33] X. H. Wu, P. Fini, S. Keller, E. J. Tarsa, B. Heying, U. K. Mishra, S. P. DenBaars, and J. S. Speck *Jpn. J. Appl. Phys., Pt. 2*, vol. 35, p. L1648, 1996.

[34] B. Heying, X. H. Wu, S. Keller, Y. Li, D. Kapolnek, B. P. Keller, S. P. DenBaars, and J. S. Speck *Appl. Phys. Lett.*, vol. 68, p. 643, 1996.

[35] L. Shen, S. Heikman, B. Moran, R. Coffie, N. Q. Zhang, D. Buttari, I. P. Smorchkova, S. Keller, S. P. DenBaars, and U. K. Mishra *IEEE Electron Dev. Lett.*, vol. 22, p. 457, 2001.

[36] S. C. Binari, K. Ikossi, J. A. Roussos, W. Kruppa, D. Park, H. B. Dietrich, D. D. Koleske, A. E. Wickenden, and R. L. Henry *IEEE Electron Dev. Lett.*, vol. 48, p. 465, 2001.

[37] W. Mickanin, P. Canfield, E. Finchem, and B. Odekirk *in GaAs IC Symp. Dig.*, p. 211, 1989.

[38] R. Yeats *et al. IEDM Tech. Dig.*, p. 842, 1988.

[39] J. C. Huang *et al. IEEE Trans. Microwave Theory Techniques*, vol. 41, p. 752, 1993.

[40] G. Simin, A. Koudymov, A. Tarakji, X. Hu, J. Yang, M. A. Khan, M. S. Shur, and R. Gaska *Appl. Phys. Lett.*, vol. 79, p. 2651, 2001.

3
Mass-Transport Growth

THE work in this chapter started out as a small study to find out what happens to non-planar masked samples during heat-up, prior to growth. It turned out that major transport of material occurred in very short times, causing growth at the mesa edges. This interesting mass-transport phenomena warranted an in-depth study, including aspects such as mechanisms and driving force, range, and characteristics of the grown material. The mass-transport growth can in principle be performed in an ammonia annealing chamber, without supply of gallium, transforming it into a potentially cheap and simple growth technique. The basic studies of the mass-transport growth technique is the focus of the present chapter. The technique was utilized for n^+-GaN ohmic contact regrowth, but that study will be presented in Chapter 5.

The mass-transport effect is something that must be considered when performing conventional non-planar growth by MOCVD. Rapid growth may occur at the mesa edge, *before* the intended MOCVD growth can commence. For HEMT applications, the growth at the mesa edge is the most important, and control of impurity incor-

poration or alloy composition can not be obtained if mass transport growth occurs. In the non-planar selective area growth studies of Chapter 4, the growths were performed under conditions to avoid mass transport growth, essentially by choosing a lower than usual growth temperature.

3.1 Introduction

Mass transport occurs during all epitaxial GaN growth. For growth of c-plane GaN, it is mass transport that establishes the characteristic step-flow growth mode, by transporting species adsorbed on steps to the step edges. The apparent range of this mass transport is very short, typically less than 0.2 μm. More prominent mass transport effects occur during selective area growth, when material deposited on the mask is transported to the mask openings, over distances of several hundred μm.

The driving force for mass transport is the inclination of a system to minimize its total surface energy. During step-flow growth, species adsorbed on a step have higher surface energy than species at a step edge, and by diffusing to the step edge, or to a step-kink, the surface energy is minimized. For the diffusion process to work efficiently, the thermal energy present in the system has to be of the same order as the bond energies of adsorbed species.

Mass transport can also transpire without external supply of growth species, for example during heat-up or during an anneal. One example of mass-transport occurs during the standard two-step process for growth of GaN on sapphire. During the

heat-up following the low-temperature nucleation layer deposition, changes in the grain-size and crystal structure of the nucleation layer has been observed.[1] The nucleation layer is deposited at low temperature, with insufficient energy to produce a structure with a minimized surface energy. In general, a surface with high curvature has a high surface energy (see for example ref. [2]).

Similar to an as-grown nucleation layer, a GaN film with etched features on the surface, such as a trench or a mesa, has a high surface energy. Several years ago, a research group at Meijo University reported significant mass transport around an etched trench on a GaN surface.[3] By annealing the trench in a nitrogen and ammonia atmosphere at high temperature, mass transport occurred from the unmasked top surface into the trench, filling it up completely with material. The Meijo University group pursued this technique as a means to grow nearly dislocation-free material in the trench.

The structures used for non-planar SAG are similar to the etched trench used in ref. [3], except that the top surfaces are covered with a regrowth mask, preventing the underlying material from desorbing. However, if the mask openings are large enough, material can desorb from the bottom of the etched areas, and get redistributed within the etched area. This is the scenario that will be studied in this chapter.

Mass transport effects have also been observed for InP, when annealing in an ambient of H_2 and PH_3. As early as 1982, Liau *et al.*[4] used mass transport of InP

to fabricate a GaInAsP/InP buried heterostructure laser, and later the technique was applied to improve chemically etched mirrors for GaInAsP/InP lasers.[5] A more detailed study of the mass transport phenomena was performed in 1983 by Chen *et al.*,[6] also focusing on applications in laser diode fabrication. A general selective area growth study of InP, including mass transport effects, was reported by Blaauw *et al.*,[7] including observations of anisotropy of the mass transport. The InP mass transport experiments were performed at temperatures between 670°C and 750 °C, for 30 minutes or more. The mass-transport caused a general rounding of the etched features, and was able to fill in voids caused by non-planar MOCVD growth.

3.2 Sample Preparation

The samples used for the mass-transport experiments, as well as for the non-planar SAG experiments in Chapter 4, were fabricated on GaN base-layers prepared by MOCVD on sapphire substrates. For the experiments on impurity incorporation (see §3.7 and §4.6), the GaN base-layers were grown semi-insulating, by means of Fe doping (see §2.3.5). For device applications (see Chapter 5), the growths were performed on HEMT structures, essentially the same as the semi-insulating GaN films with an additional 20 - 30 nm $Al_{0.35}Ga_{0.65}N$ cap layer. On the base-layer a mask was patterned by photolithography, deposition of a dielectric, and lift-off. The mask material was usually SiO_2, deposited by e-beam evaporation to a thickness

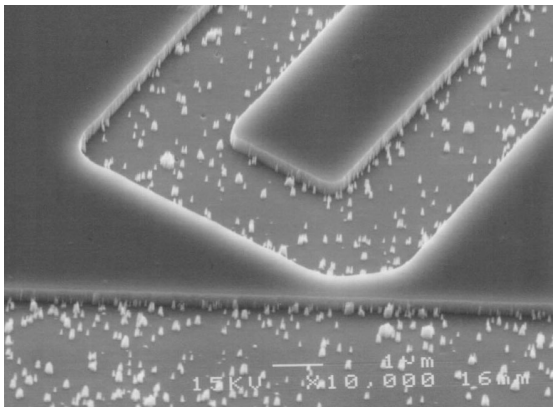

Figure 3.1: SEM image of a sample where micromasking occurred during the reactive ion etching. The micromasking is attributed to surface contamination prior to the etch, specifically photo-resist residue.

---

of 100 - 200 nm. In a few experiments an AlN mask was used, deposited by DC magnetron sputtering, to a thickness of $\sim$ 40 nm. Following lift-off, Cl_2 reactive ion etching (RIE) was used to etch 400 nm into the GaN film, using the dielectric as etch mask. It was found that the AlN etched too fast to serve as an etch mask, so a SrF_2 layer was deposited on top of the AlN, serving as an etch mask during the Cl_2 reactive ion etch, and was afterwards removed in HCl.

3.2.1 Etch Quality

A reasonably smooth etched surface was important for the success of the growth experiments. In the early phase of the work, the Cl_2 RIE would sometimes result in a very rough surface, on which smooth growth could not be performed. An example of a sample after a rough etch is shown in Fig. 3.1. Through studies of

the sample surface prior to etch, by atomic force microscopy, it became clear that the morphology shown in Fig. 3.1 was due to surface contamination *prior* to etch. By considering the process details, it was concluded that the surface contamination consisted of residues from the photo-resist used for patterning the dielectric mask. Although the amount of residue depended on which photo-resist was used, and on other factors, it was found that solvents such as acetone and 2-propanol in general were unable to remove the photo-resist completely. Other techniques, such as flood exposure followed by soak in developer, or prolonged O_2 plasma etches, were developed to remove the photo-resist residue. Once a clean surface was obtained, the Cl_2 RIE always produced smooth etched surfaces. No signs of micromasking from sputtering of the dielectric mask were ever observed.

Some changes in the etch roughness with etch conditions were detected by AFM, but those changes were on a much smaller scale than what is shown in Fig. 3.1, and seemed to have no effect on the subsequent growth. It was for example shown that a lower etch pressure yielded smoother surfaces, while the power level had no influence on the surface roughness. The conditions used throughout this work were as follows: 200 W, 2 mT, and 9 sccm Cl_2. These conditions resulted in an etch rate of about 100 nm per minute.

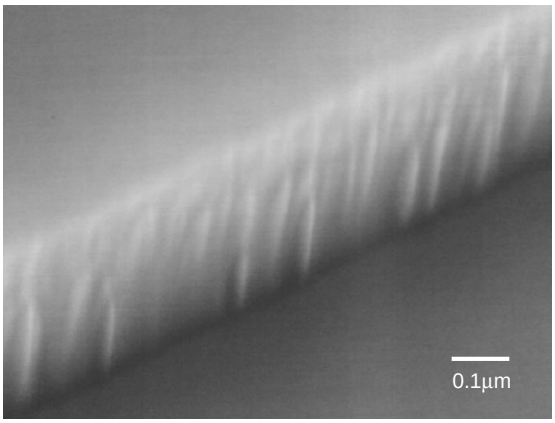

Figure 3.2: SEM image of a sample before anneal, at edge of etched mesa. The sidewall striations are attributed to the dry etch process.

3.3 Annealing Experiments

Samples prepared as described in the previous section, were heated up in an atmosphere of H_2 and NH_3, at a pressure of 100 Torr, and were annealed for 1 minute. The temperature of the anneal ranged from 960°C to 1090°C, and the NH_3 and H_2 flows were 8 slpm and 4 slpm, respectively. No TMGa was injected during the anneal.

An SEM image of a typical sample before anneal is shown Fig. 3.2. The light striations of the sidewall were an effect of the reactive ion etching, and showed no dependence on crystallographic orientation. Fig. 3.3 shows the result of annealing samples at temperatures of 960°C, 1060°C, and 1090°C. At 960°C only little mass transport occurred, with small amounts of material building up at the mesa base. The sidewalls oriented in the $\langle 11\bar{2}0 \rangle$ direction were smoother than before the anneal, but

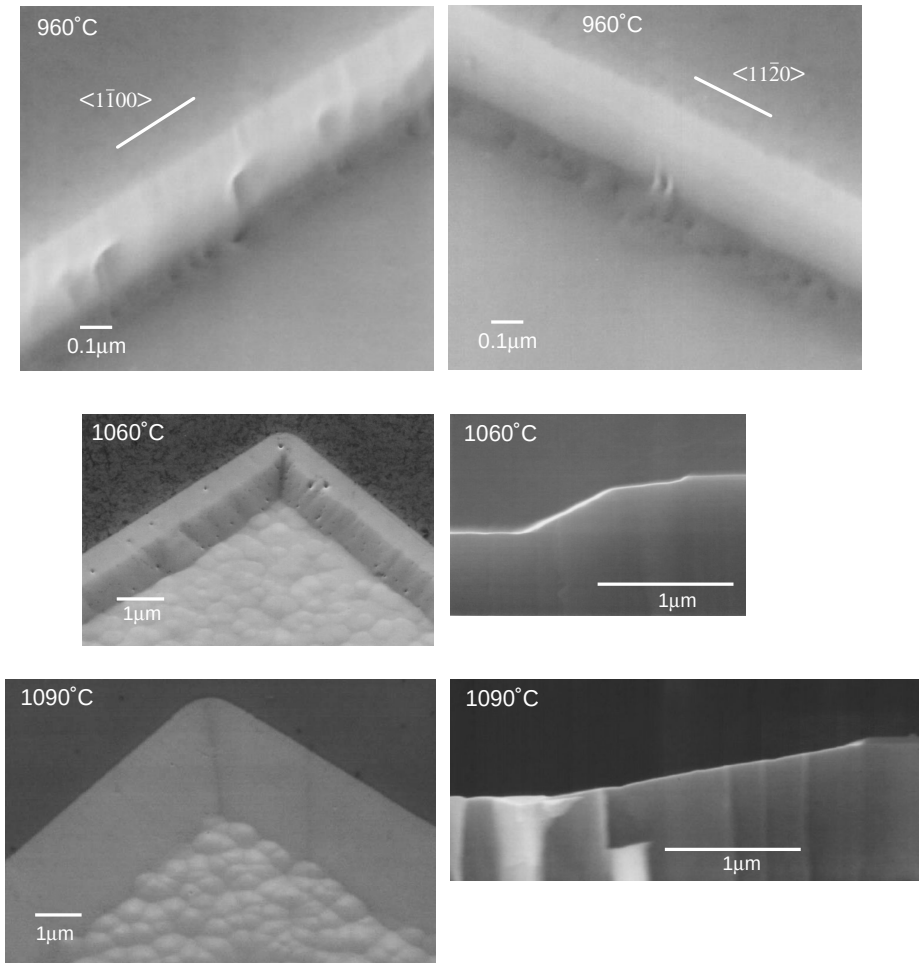

Figure 3.3: Annealing study of sample with masked mesas. When annealed at 960°C, only little mass transport occurred. The sidewall of the mesa oriented in the $\langle 11\bar{2}0\rangle$ direction got smoother, but the sidewall of the mesa oriented in the $\langle 1\bar{1}00\rangle$ direction got etched indentations. When annealed at 1060°C and 1090°C, mass transport resulted in wedge-shaped growth at the mesa edges, extending up to 2 μm from the original mesa sidewall. The growth showed no significant orientation dependence.

---

the sidewalls oriented in the $\langle 1\bar{1}00\rangle$ direction showed etched indentations from the anneal. The anneals at 1060°C and 1090°C resulted in wedge-shaped growths at the mesa edge, extending approximately 1 μm and 2 μm from the original sidewall, re-

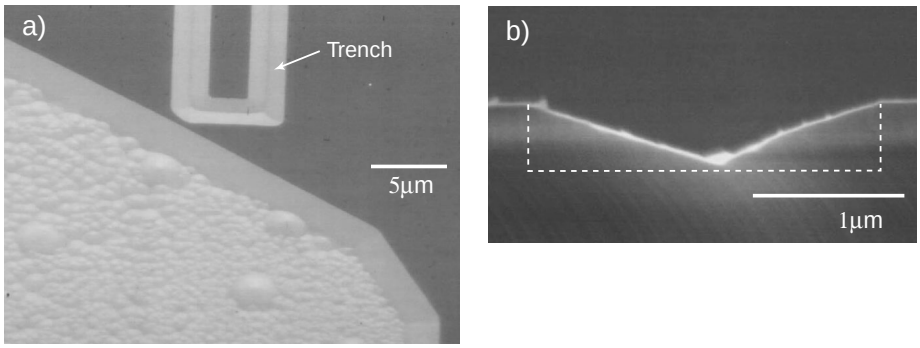

Figure 3.4: a) Sample with a narrow trench near a large unmasked area, after anneal. b) Cross-section of trench. The dashed line marks the etched trench prior to the anneal.

spectively. No significant orientation dependence was detected, in contrast to observations for InP mass-transport.[7] The bottom surface showed roughened morphology after the anneals at 1060°C and 1090°C, indicating that desorption had occurred from this surface, in an inhomogeneous manner. The observed lateral growth rates were very high, corresponding to nearly 120 μm/hr for the higher annealing temperature. This is more than an order of magnitude faster than what can be achieved through conventional MOCVD lateral growth techniques.[8] For the continued annealing studies, 1090°C was chosen as the standard temperature.

Fig. 3.4a shows a narrow etched trench located near a large unmasked area, after anneal. Evidently, desorption has occurred from the large unmasked area, depositing material not only at the edge of the large area, but also in the trench. Fig. 3.4b shows the cross-section of a trench on a similar sample, revealing a V-shaped growth profile. From this experiment it is clear that the mass transport effect is a long range

effect, with a range of at least 10 - 15 μm. In §3.6 it is shown that mass-transport can occur over larger distances, up to $\sim$ 300 μm. SAG experiments by Mitchell *et al.* established that long range diffusion of growth species, over both masked and unmasked surfaces, occurs predominantly in the gas-phase.[9] The transport mechanism for material from the unmasked area into the trench in Fig. 3.4, is most likely also a gas-phase process.

The annealing time had very little effect on the growth. Annealing for 5 minutes at 1090°C produced visibly the same results as annealing for only 1 minute. It should be mentioned that the quoted annealing times include temperature stabilization times. For a 1 minute anneal, the actual temperature reached to within 10°C of the set-point after about 40 seconds, and remained within 10°C for only about 25 seconds before cooling down. Due to the slow temperature response, it was difficult to determine exactly how fast the mass-transport growth is. However, compared to mass-transport experiments in InP, where the anneals typically are performed for more than 30 minutes, the growth rates are extremely fast. The fact that no additional growth occurred after the first minute of anneal demonstrates that the process is self-limiting. The 1090°C growth profile obtained in Fig. 3.3 is an equilibrium profile, established by equal rates of adsorption and desorption.

3.4 Annealing Conditions

The presence of ammonia during the annealing process is crucial; if no ammonia is present over GaN at elevated temperature, it becomes unstable and dissociates under formation of Ga-droplets. Ammonia is necessary for successful mass-transport growth, both for efficient desorption of Ga-species from the unmasked areas,[10] and for stabilizing the growth at the mesa edges. To study the influence of the ammonia supply, an anneal was performed under reduced ammonia conditions, with gas flow of 4 slpm NH_3, 4 slpm N_2, and 4 slpm H_2. The result, shown in Fig. 3.5, shows that the growth along the mesa edge was unstable, only occurring in some locations. From this it seems that a large supply of ammonia is necessary to ensure stable initialization of the growth at the mesa base.

When performing an anneal with N_2 carrier gas instead of H_2, mass transport also occurred. Fig. 3.6 shows a sample after anneal at 1090°C in 4 slpm N_2 and 8 slpm NH_3. The growth showed similar properties to the annealed with H_2 carrier gas (see Fig. 3.3). However, it can be seen that the exposed open areas remained smooth after the anneal, due to a less aggressive thermal desorption in the absence of H_2 carrier gas.

The pressure dependence of the mass transport growth was investigated by performing anneals at reactor pressures of 50 Torr and 300 Torr, in addition to the standard pressure 100 Torr. No detectable pressure dependence was observed.

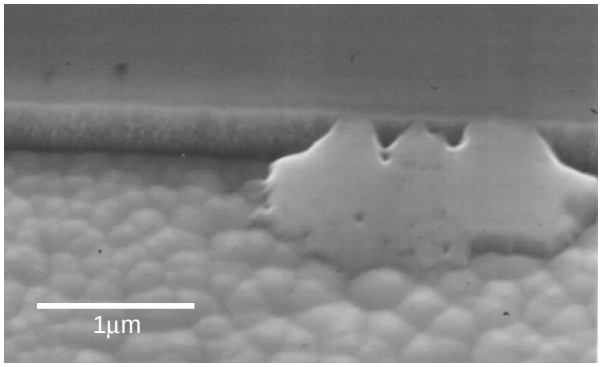

Figure 3.5: SEM image of a sample annealed in 3 slpm ammonia, half of the usual flow. The growth along the mesa edge was unstable and occurred only in some locations.

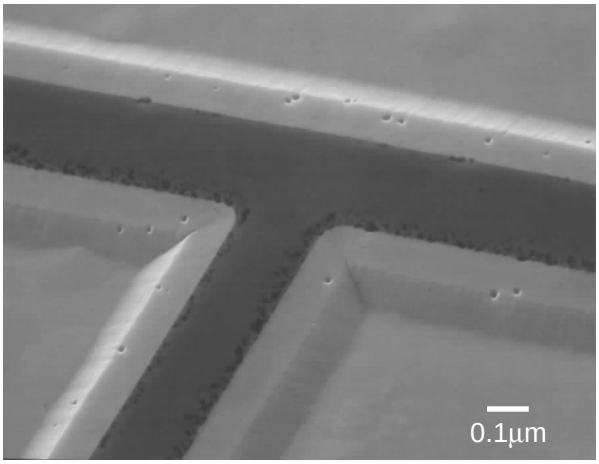

Figure 3.6: A sample after anneal in N_2 and ammonia. The unmasked area is smoother than on samples annealed in H_2 and ammonia.

3.5 Driving Force

Previously in this chapter it has been stated that the driving force behind the mass transport phenomena is minimization of surface energy. The concave corner created by the mesa etch is a point of high surface energy, which can be eliminated by transporting material into the corner. Another possible driving force could be that the growth rate on the vertical facet is much higher than that of the c-plane surface. At the relatively high temperatures of the anneal, the GaN c-plane is experiencing desorption in the absence of TMGa flow. This is not necessarily true for other crystal planes, and the material desorbed from the c-plane can diffuse and deposit on surfaces capable of sustaining a positive growth rate.

An experiment was devised to study what the driving force of the mass transport growth is. The test structure, illustrated in Fig. 3.7a, consisted of a sample prepared the normal way (described in §3.2), that had received a second thin layer of SiO_2 mask partially covering the etched area. The second SiO_2 layer was evaporated onto the sample under a slight angle, to ensure that there was no sidewall coverage on at least one side of the mesas. The final structure thus had some areas where the etched bottom surface close to the mesa was masked. The structure was annealed at 1090°C for 3 minutes, and the result is shown in Fig. 3.7b, with close-ups of the mesa edge in Fig. 3.7c-d. In the region without masked bottom surface, mass transport growth occurred as normal. In the region *with* masked bottom surface,

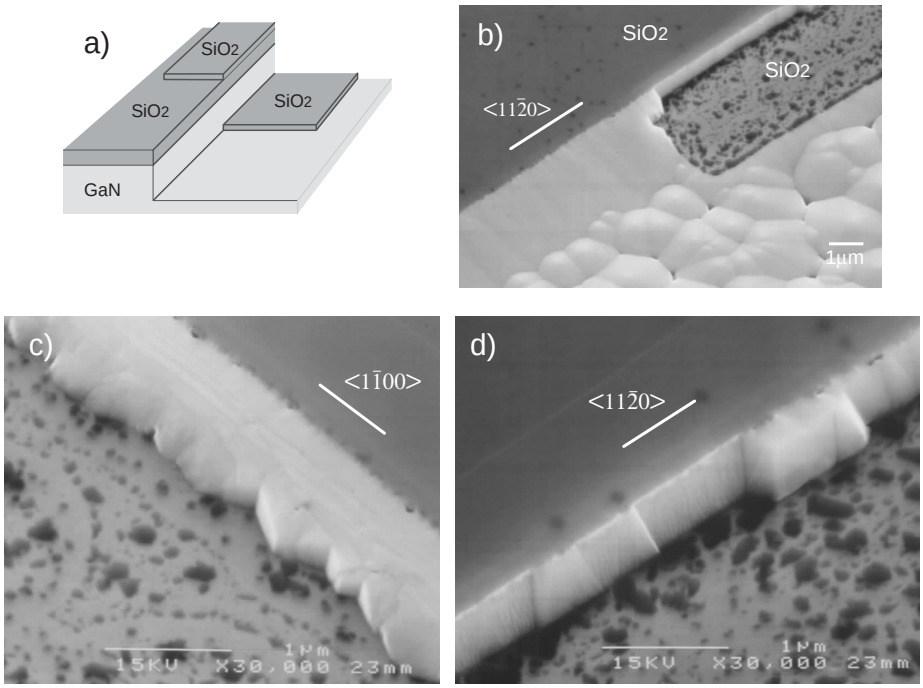

Figure 3.7: Experiment to investigate the driving force behind mass transport growth. a) Schematic of the test structure. b) Test structure after anneal c)-d) Close-up of mesa edges aligned to different crystallographic orientations.

---

the behavior was orientation dependent: for a $\langle 11\bar{2}0\rangle$ mesa orientation (Fig. 3.7d) no significant growth occurred, but for a $\langle 1\bar{1}00\rangle$ mesa orientation (Fig. 3.7c), some lateral growth was observed, extending nearly 1 μm from the mesa edge, with a jagged front formed by $\{1\bar{1}00\}$ facets. The spotted surface of the thin SiO_2 mask is a sign of mask decomposition, probably due to the small thickness of the mask. With the bottom surface masked near the mesa, material could not deposit in the concave corner, thereby eliminating minimization of surface energy as a driving force. From the experiment it can therefore be concluded that mass transport growth

along $\langle 11\bar{2}0\rangle$ oriented mesas is driven by surface energy. For mass transport growth along $\langle 1\bar{1}00\rangle$ oriented mesas on the other hand, the high growth rate of the vertical sidewall is also a contributing factor. This result is consistent with what is typically observed for ELO of GaN; growth on $\langle 11\bar{2}0\rangle$ oriented stripes generally exhibit slow lateral growth, while growth on $\langle 1\bar{1}00\rangle$ oriented stripes can have very high lateral growth rates.[8]

The experiment determined what the driving force for the mass-transport growth is. More precisely, it showed why material at the mesa edge is stable and can sustain positive growth rates, at the same time as unmasked areas away from the mesa edge are unstable and experience net desorption. In the end, what actually *causes* the growth is a large supply of gallium species in the gas-phase; the driving force by itself can not cause growth. This is for example why mass-transport growth of GaN on an AlGaN base-layer would not work; AlGaN is much more stable than GaN at reasonable temperatures, so there would be no supply of growth species, and therefore no growth.

3.6 Range of Mass Transport Effect

In §3.3 it was shown that mass transport can take place over a distance. Material desorbed from a large unmasked area diffused over a masked region and deposited in a narrow trench, over a distance of 10 - 15 μm. Presented in this section is a more

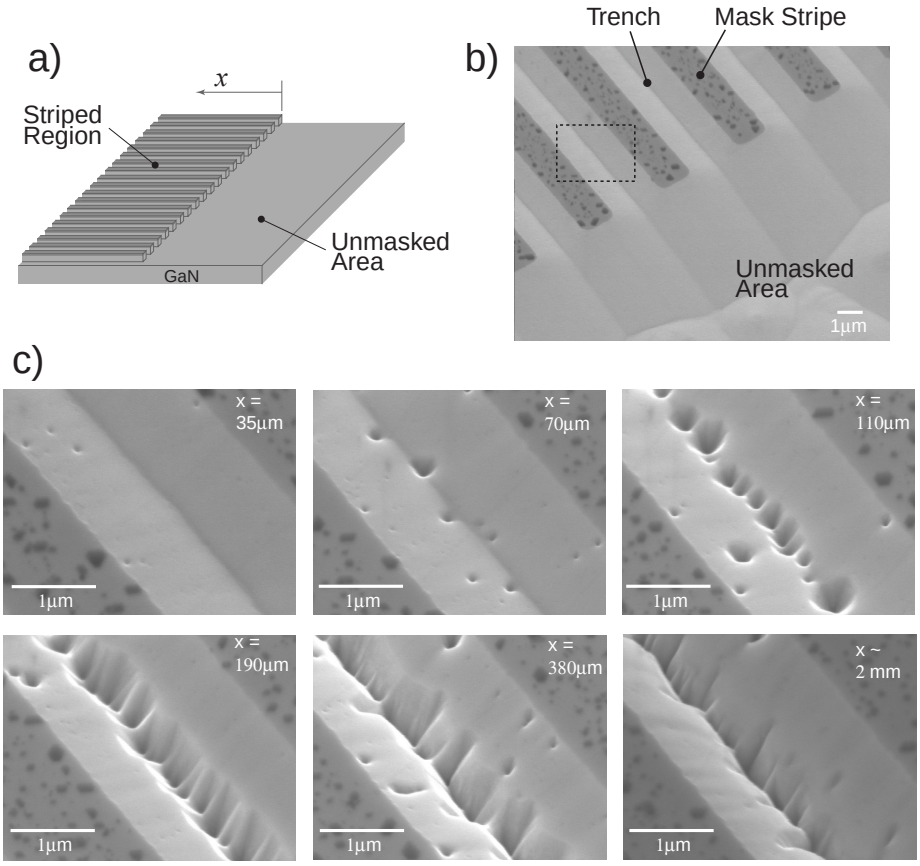

Figure 3.8: Investigation of the range of the mass transport effect. a) The test structure. *x* marks the distance from the edge of the unmasked area. b) Edge of the large unmasked area, after mass-transport anneal. Growth has occurred between the masked stripes, and from the edge of the striped region ~ 4 μm into the unmasked area. The dotted square indicates the view of the images in c), at various distances *x* from the edge of the unmasked area.

---

quantitative study of the range of the mass transport effect.

A schematic of the test sample used in this experiment is shown in Fig. 3.8a. The sample had a large region with masked stripes, located next to an unmasked area. The SiO_2 masked stripes were 2 μm wide, and were separated by 2 μm etched trenches. Upon anneal, the unmasked area served as a supply of growth species

for the striped region, causing growth to occur in the trenches. At the edge of the unmasked area, the mass transport growth was very smooth, as seen in Fig. 3.8b. The trench growth in the striped region was examined at various distances *x* from the unmasked area. The resulting SEM images, for *x* ranging from 35 μm to $\sim$ 2 mm, are presented in Fig. 3.8c, and they show that mass-transport growth occurred in all locations. At a distance of 35 μm, the growth was as smooth as at the edge of the unmasked region, but at 70 μm distance a few pits appeared in the growth. At a distance of 120 μm more pits were present, located at the center of the V-shaped growth, and for distances of 190 μm and more, the pits formed a more or less continuous groove in the center of the trench. The presence of the pits was due to gas phase depletion of growth species as the distance to the source of the growth species (the unmasked area) was increased.

At a distance of 380 μm and beyond, the growth morphology was constant, with some mass transport growth visible. Considering that the unmasked area constituted only about 2 % of the total sample area, it seemed unreasonable that it would supply growth species for the entire sample. To clarify the observed growth behavior, the sample was cleaved, and the striped region was examined in cross-section by SEM. Fig. 3.9a shows the the growth in trenches located 30 μm, 90 μm, 130 μm, and 720 μm from the edge of the unmasked area. In Fig. 3.9b, the profiles of the four cross-section images in Fig. 3.9a have been combined, overlayed on a schematic of the original 0.4 μm deep etched trench. It is clear that the slope of the V-shaped

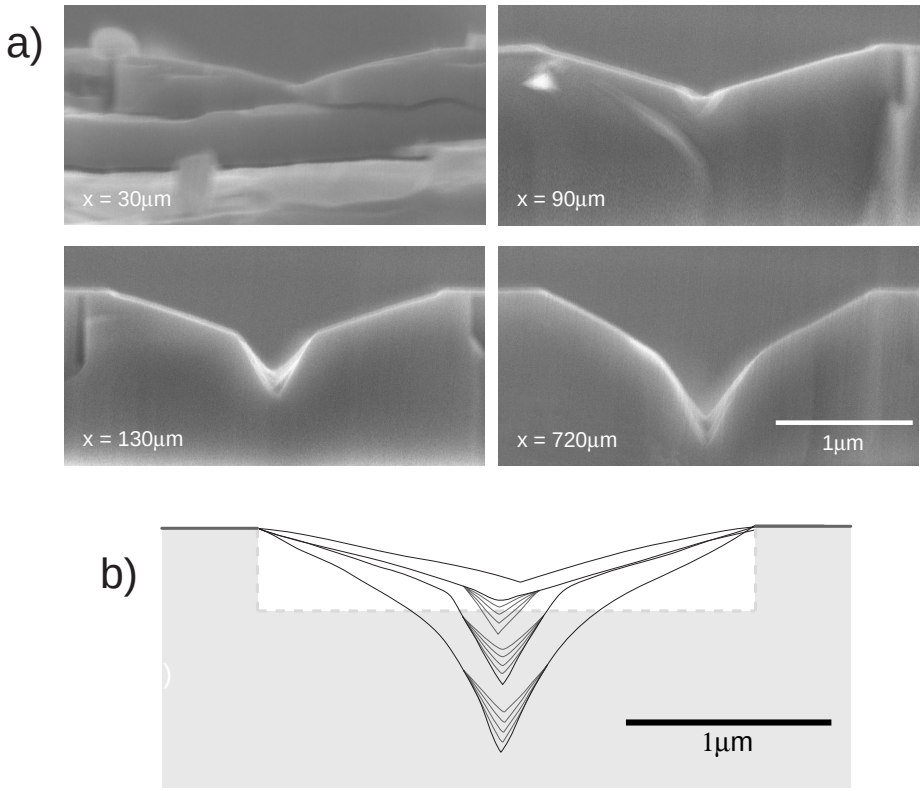

Figure 3.9: Investigation of the cross-section of trench growth as a function of distance to the unmasked area. a) SEM images at distances 30 μm, 90 μm, 130 μm, and 720 μm. b) Profiles of the SEM images, combined in one plot, from top to bottom 30 μm, 90 μm, 130 μm, and 720 μm. The grey area represents the cross-section of the original etched trench.

---

growth varies with the distance to the unmasked area. Already at a distance of 90 μm, the pits in the center extend below the original etched bottom surface. At increasing distances, the pits in the center extend deeper, and there is less net amount of deposited material. At 720 μm, the cross-section area of the material desorbed at the center of the trench roughly equals the area of the material deposited at the mesa edges, which means that no net growth occurred, just rearrangement of material within the trench. From this it can be concluded that the range of material diffusing

from the unmasked region is somewhere between 130 μm and 720 μm, probably around 300 μm judging from Fig. 3.8. Within this range the supply of growth species declines rapidly, and at 300 μm the supply is a very small fraction of the supply near the unmasked area.

3.7 Autodoping of Mass Transport Growth

Impurity incorporation for selective area growth is typically affected by the material in the regrowth mask, as well as by external doping. The mask material of choice, SiO_2, etches slightly under formation of volatile Si and O species, when exposed to NH_3 and H_2 at elevated temperature. Both silicon and oxygen act as shallow donors and lead to n-type doping when incorporated into the GaN crystal lattice. High free carrier concentrations is an indicator of auto-doping, and has been observed in for example refs. [11, 12]. The impurity incorporation is of importance for device applications; for n^+-GaN contact regrowth, the highest possible n-type doping is desired (see §5.2).

The mass transport growth invokes higher temperatures than normal GaN growth does, which enhances the thermal etching of the mask. This leads to more impurities in the gas-phase, but the higher temperature may also change the incorporation behavior of the impurities. Two techniques were used to quantify the impurity incorporation into the mass transport growth: secondary ion mass spectrometry (SIMS),

and electrical conductivity measurements. The investigations will be presented next.

For the SIMS characterization, a similar sample structure to the one used for the range experiment in §3.6, was used. A large part of the sample consisted of 2 μm SiO_2 stripes separated by 2 μm trenches. A large unmasked area was located at the center of the sample, serving to supply growth species to the surrounding striped areas. A large entirely *masked* area was also present on the sample, to serve as reference for the SIMS measurement. Upon annealing the sample, mass transport occurred, causing V-shaped growth in the trenches of the striped regions. After the anneal the mask was removed, and the sample was subject to a $\sim$ 2 μm GaN regrowth using regular MOCVD. The GaN regrowth was performed to planarize the sample surface, and to bury the material to be tested, which is necessary to avoid surface contamination during the SIMS measurement. Fig. 3.10 illustrates the fabrication process, for the striped region and the large masked area on the sample.

SIMS measurements were performed on 500 μm $\times$ 500 μm areas, in two locations on the sample. One measurement was obtained in the striped region, and the the other measurement was obtained in the large masked area; the depth profiles are presented in Fig. 3.11. Large concentrations of Si and oxygen were detected in the striped region, over a depth of $\sim$ 0.4 μm, with the Si reaching up to 7×10^{18} cm^{-3} and the oxygen reaching up to 3×10^{18} cm^{-3}. The depth 0.4 μm corresponds to the depth of the etched trenches, and consequently to the depth extent of the mass-transport growth. In the masked area, spikes of Si and oxygen were detected, with

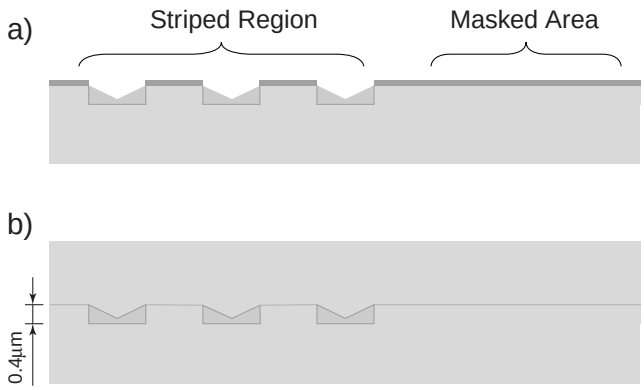

Figure 3.10: Structure for SIMS measurements. a) Mass transport growth was performed on sample with striped area and a large masked area. b) The SiO_2 mask was removed, followed by a planarizing MOCVD GaN growth.

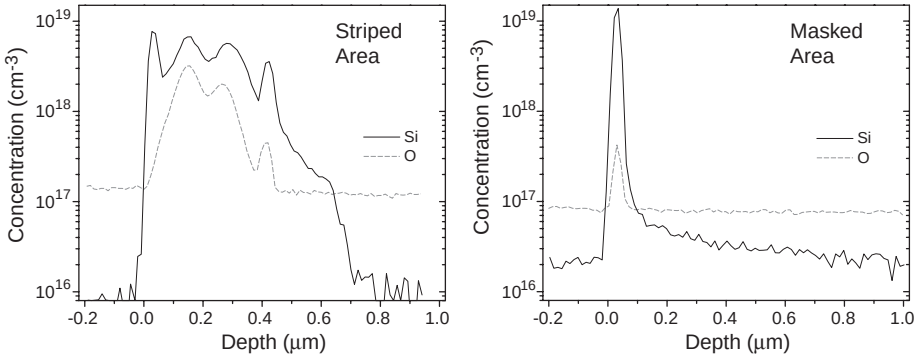

Figure 3.11: SIMS profiles of mass transport growth. Profiles were obtained in two locations, in the striped region and in a large masked region. The zero point on the depth scales marks the MOCVD regrowth interface.

peak concentrations of 1.4×10^{19} cm^{-3}, and 4×10^{17} cm^{-3}, respectively. The spikes were located at the MOCVD regrowth interface, and were most likely caused by SiO_2 mask residues left by incomplete mask removal. The profile from the masked area serves as a reference, from which it can be concluded that the first Si peak in the

striped-region profile, which is exactly half the height of the peak in the masked area profile, is related to the regrowth interface. Apart from the first Si peak, the remaining Si and O in the striped area profile can be assigned to the mass-transport growth. The average concentrations within the 0.4 μm region were calculated (excluding the first Si peak), resulting in the values 3.9×10^{18} cm^{-3} for Si and 1.3×10^{18} cm^{-3} for oxygen. These values represent the average concentrations in the 0.4 μm thick layer containing the mass transport growth. As can be seen from the geometry of the striped region in Fig. 3.10, the undoped masked mesas constitute half of the volume of this layer, and about half of the remaining volume is occupied by undoped MOCVD regrowth, due to the V-shape of the mass-transport growth. To obtain the average impurity concentrations inside the mass transport growth, the previously calculated average concentrations therefore had to be multiplied by a factor 4. When doing so, the corrected concentrations were 1.6×10^{19} cm^{-3} Si, and 5×10^{18} cm^{-3} oxygen, adding up to a total n-type impurity concentration of 2.1×10^{19} cm^{-3}. This is a remarkably high impurity concentration, considering that no external dopant species were supplied during the growth. As a matter of fact, for normal planar MOCVD growth, Si doping in excess of 1×10^{19} typically leads to a rough morphology. It is probably the non-planar nature of the growth, and the high growth rate, that allows high impurity concentrations without causing poor morphology. What can also be noted is that although the silicon to oxygen ratio in SiO_2 is 1:2, the ratio in the grown material is 4:1. This is related to a low oxygen incorporation

efficiency,[13] caused by a thermal instability of gallium-oxide compounds in the presence of ammonia.[14]

The impurity incorporation for mass transport growth was also quantified by electrical resistivity measurements. For these measurements the samples were prepared on semi-insulating base-layers, to ensure that only the mass-transport growth was being probed. Ohmic contact pads were formed in a TLM pattern, oriented *along* the mesa edge, allowing the resistance *per unit length* of the wedge-shaped growth to be measured. By normalizing the measurements to the cross-section area of the growth, the average resistivities could be calculated. Values of 3×10^{-3} Ωcm and 4×10^{-3} Ωcm were obtained from two samples. Without knowing the carrier mobility, these numbers can not be compared to the SIMS impurity concentrations. However, assuming a mobility of 100 cm^2/Vs, based on experimental values for Si-doping of GaN,[15] the measured resistivities translate into a carrier concentration of nearly 2×10^{19} cm^{-3}, which agrees well with the measured SIMS n-type impurity concentration. Resistivity measurements were also performed for mass transport growth in a 2 μm trench, and similar results were obtained. On samples with an AlN mask, the resistivity was found to be between 6×10^{-2} Ωcm and 13×10^{-2} Ωcm, over an order of magnitude higher than for the SiO_2 masked samples. This clearly shows that the high conductivity obtained for the SiO_2 masked samples is due to autodoping from the SiO_2 mask. Interestingly, although more resistive than the SiO_2 masked samples, the resistivity of the AlN masked samples were still quite low, indicating

substantial impurity concentrations. The reason probably lies in the non-planar nature of the growth, and the high growth rate, both of which can strongly affect impurity incorporation. Similar observations for SiO_2 and AlN mask materials used during regular non-planar SAG will be discussed in §4.6. Another possible source of the low resistivity is the formation of native defects, such as nitrogen vacancies, during the rapid mass transport growth.

3.8 Discussion and Future Work

Mass-transport growth is an interesting growth technique, which does not require a Ga precursor, but it can also be a problem for regular non-planar selective area growth, if the growth temperature is too high. Some aspects of the mass-transport growth were investigated in this chapter, including the dependence on annealing conditions, the mechanism, the range, and the autodoping from the mask. Some other parameters were not studied, notably the etch depth of the starting samples. Early on in the study an etch depth of 0.4 μm was settled on, and was since not changed except for a few experiments. 0.4 μm was deep enough that the features of the growth could be studied with SEM without difficulty, and it was shallow enough not to cause problems during the reactive ion etching. The few experiments performed on samples with 0.2 μm etch depth resulted in similar growths, with about the same lateral extent as for an etch depth of 0.4 μm. It can be interesting to explore

other etch depths, in particular the extremes of very deep and very shallow etches.

One aspect I believe is important to study is external oxygen doping during the anneal, because of the impact it may have for device applications. One experiment was performed where Si doping was supplied externally during the growth, but the Si doping resulted in a changed morphology, and it did not improve the contact properties of the material. I instead propose exploring oxygen as an n-type dopant, using O_2 as the precursor. Oxygen doping of GaN has been demonstrated both by MOCVD and MBE,[13, 16] in both cases using O_2 as the precursor. There are indications that oxygen incorporation is strongly anisotropic, being much higher on N-polar c-plane GaN,[16] and on $\{1\bar{1}01\}$ facets,[17, 18] than on the standard Ga-polar c-plane GaN. Some initial oxygen doping experiments performed at UCSB showed similar trends, with very low oxygen incorporation on a smooth c-plane surface, and high incorporation on a rough surface. There is reason to believe that the oxygen incorporation would be high for mass-transport growth, due to the non-planar nature of the growth. The SIMS investigation in §3.7 showed that $\sim$25% of the n-type dopant was oxygen, originating from the mask, and by supplying more oxygen in the gas stream, it may be possible to increase the total doping concentration. Oxygen has the advantage of not reacting with ammonia, in contrast to Si, which forms SiN. This allows very high oxygen concentrations to be injected together with ammonia during the anneal, without forming undesired compounds.

References

[1] X. H. Wu, D. Kapolnek, E. J. Tarsa, B. Heying, S. Keller, B. P. Keller, U. K. Mishra, S. P. DenBaars, and J. S. Speck *Appl. Phys. Lett.*, vol. 68, p. 1371, 1996.

[2] W. D. Kingery, H. K. Bowen, and D. R. Uhlmann, *Introduction to ceramics*. New York: Wiley, 2nd ed., 1976.

[3] S. Nitta, M. Kariya, T. Kashima, S. Yamaguchi, H. Amano, and I. Akasaki *Appl. Surf. Sci.*, vol. 159, p. 421, 2000.

[4] Z. L. Liau and J. N. Walpole *Appl. Phys. Lett.*, vol. 40, p. 568, 1982.

[5] Z. L. Liau, J. N. Walpole, and D. Z. Tsang *Appl. Phys. Lett.*, vol. 44, p. 945, 1984.

[6] T. R. Chen, L. C. Chiu, A. Hasson, K. L. Yu, U. Koren, S. Margalit, and A. Yariv *J. Appl. Phys.*, vol. 54, p. 2407, 1983.

[7] C. Blaauw, A. Szaplonczay, K. Fox, and B. Emmerstorfer *J. Crystal Growth*, vol. 77, p. 326, 1986.

[8] H. Marchand, J. P. Ibbetson, P. T. Fini, X. H. Wu, S. Keller, S. P. DenBaars, J. S. SPeck, and U. K. Mishra *MRS Internet J. Nitride Semicond. Res.*, vol. 4S1, p. G4.5, 1999.

[9] C. C. Mitchell, M. E. Coltrin, and J. Han *J. Crystal Growth*, vol. 222, p. 144, 2001.

[10] Y. A. Vodakov, E. N. Mokhov, M. G. Ramm, M. S. Ramm, A. D. Roenkov, A. G. Ostroumov, A. A. Wolfson, S. Y. Karpov, Y. N. Makarov, and H. Jurgensen *Mat. Res. Soc. Symp. Proc.*, vol. 482, p. 27, 1998.

[11] K. C. Zeng, J. Y. Lin, H. X. Jiang, and W. Yang *Appl. Phys. Lett.*, vol. 74, p. 1227, 1999.

[12] J. A. Freitas Jr., O. H. Nam, R. F. Davis, G. V. Saparin, and S. K. Obyden *Appl. Phys. Lett.*, vol. 72, p. 2990, 1998.

[13] R. Y. Korotkov and B. W. Wessels *MRS Internet J. Nitride Semicond. Res.*, vol. 5S1, p. W3.80, 2000.

[14] S. W. King, J. P. Barnak, M. D. Bremser, K. M. Tracy, C. Ronning, R. F. Davis, and R. J. Nemanich *J. Appl. Phys.*, vol. 84, p. 5248, 1998.

[15] S. Nakamura, T. Mukai, and M. Senoh *Japan. J. Appl. Phys.*, vol. 31, p. 2883, 1992.

[16] A. J. Ptak, L. J. Holbert, L. Ting, C. H. Swartz, M. Moldovan, N. C. Giles, T. H. Myers, P. Van Lierde, C. Tian, R. A. Hockett, S. Mitha, A. E. Wickenden, D. D. Koleske, and R. L. Henry *Appl. Phys. Lett.*, vol. 79, p. 2740, 2001.

[17] F. Bertram, T. Riemann, J. Christen, A. Kaschner, A. Hoffmann, C. Thomsen, K. Hiramatsu, T. Shibata, and N. Sawaki *Appl. Phys. Lett.*, vol. 74, p. 359, 1999.

[18] K. Hiramatsu, H. Matsushima, T. Shibata, Y. Kawagachi, and N. Sawaki *Mater. Sci. & Eng. B*, vol. 59, p. 104, 1999.

4

Non-Planar Selective Area Growth

THE unifying theme of this dissertation is the development and study of the AlGaN/GaN HEMT from a growth perspective. Part of this work, focusing on the planar structure and its growth, was covered in Chapter 2. In this chapter, non-planar selective area growth is developed, as a tool to allow more advanced device designs to be implemented. The emphasis of the experiments is to understand the properties of the growth near the mesa edge, since this is the region of most importance for HEMT applications. Drawing on the lessons learned in Chapter 3, the growths are performed under conditions to avoid mass transport growth, to allow good control over the material properties near the mesa edge. Growth rate and growth evolution, impurity incorporation, and alloy composition, are studied in the near-mask region. Device applications utilizing the non-planar growth techniques developed in this chapter are presented in Chapter 5.

I would like to credit Dr. Frank Bertram and Prof. Jurgen Christen, at Otto-von-Guericke Universität Magdeburg, Germany, for the spectrally resolved cathodoluminescence microscopy, performed on one of the AlGaN samples.

4.1 Introduction

Selective area growth (SAG) of III-nitrides by metal organic chemical vapor deposition (MOCVD) is a technique that allows the fabrication of advanced device structures. SAG of GaN was first demonstrated in 1993 on a SiO_2 masked GaAs substrate,[1] and later on a GaN film on sapphire.[2] Several device structures based on GaN SAG were soon developed, for instance GaN hexagonal pyramids for cold-cathode field emitters,[3] optical waveguides,[4] and hexagonal microprisms.[5] However, a majority of the work to date has been focused on epitaxial lateral overgrowth (ELO) techniques for dislocation reduction, first demonstrated in 1997.[6] Various ELO techniques have since been developed and studied, including facet-initiated ELO by hydride vapor phase epitaxy,[7] PENDEO epitaxy,[8] and facet-controlled ELO.[9] SAG of AlGaN has also been demonstrated,[2, 10, 11, 12, 13] but the selectivity was in some cases reported to be poor. More extensive reviews of nitride SAG and ELO can be found in refs. [14, 15].

Non-planar selective area growth is a technique that has received relatively little attention in the III-nitride system. In this technique, a mask pattern is fabricated on the sample, after which the sample is selectively etched in the mask openings, resulting in a masked mesa structure. During the following growth, the material grows both in the etched areas, and on the mesa sidewalls. In the InP and GaAs material systems this technique is relatively well studied, see for example refs.

[16, 17, 18]. Non-planar SAG of GaN and AlGaN has been used for fabrication of buried-ridge laser diodes, to create transverse optical confinement and current confinement.[10, 11] Non-planar SAG is also attractive for lateral conduction devices, in particular AlGaN/GaN high electron mobility transistors (HEMTs). It allows direct contact between the regrown material and the device channel through the etched sidewall. Using non-planar SAG, n^+-GaN regrown ohmic contacts have been demonstrated for AlGaN/GaN HEMTs.[19, 20, 21] In these structures, the current is passed from the contact metal through a short section of the regrown material into the channel of the device. Clearly, the properties of the regrown material near the mesa edge is most important for the device performance. For regrown ohmic contacts the highest possible n-type doping is desired to reach low contact resistance, but for other device applications, including drain regrowth for dispersion control (see section §5.5), a controlled amount of doping is desired. The doping level is ideally controlled by the external supply of dopant species alone, but in reality the regrowth mask can influence the impurity levels as well. The mask material of choice, SiO_2, dissociates slowly during growth, resulting in autodoping of the growing film.[22, 23] The impurity incorporation may also be complicated by the presence of multiple surfaces with different orientations and growth rates. Furthermore, for structures involving non-planar SAG of AlGaN, composition control may be important, both near and far from the mesa.

In this chapter studies of non-planar selective area growth of GaN and $Al_{0.1}Ga_{0.9}N$

are presented, focusing on the growth behavior near the mesa edge. In the studies, the time evolution of the growth was examined by performing interrupted growths. The compositional uniformity of the AlGaN was studied by cathodoluminescence microscopy, and the impurity incorporation of the GaN growth was studied by conductivity measurements near and far from the mesa. Some correlation is found between the measured properties, and the observed evolution of the growth.

The samples used for the study were prepared in the same way as the samples for the mass-transport growth studies. The details can be found in §3.2.

4.2 Growth Conditions

Growth temperature is an important parameter for III-nitride growth, in particular for selective area growth. If the temperature is too low, deposits may occur on the mask, thereby compromising the growth selectivity. For ELO work, and SAG on planar samples, the growth temperature is usually chosen to be near the typical temperature for planar growth, around 1050°C. For non-planar SAG, a high growth temperature can have drastic effects on the growth in the regions near the mask edge, as was the subject of Chapter 3. The etch creates a vertical sidewall with a concave corner to the bottom surface, a structure with high surface energy. Upon heating in ammonia to sufficiently high temperatures, spontaneous mass-transport may result, transporting GaN from the open areas into the concave corner, rapidly

depositing material into a wedge shaped feature at the mesa edge. The effect was very pronounced at a temperature of 1050°C and above, but was much smaller at a lower temperature of 960°C. The effect can be a problem for non-planar SAG, when control of growth rate, doping, or alloy composition, in the near-mesa region is desired. Spontaneous mass-transport may occur during the short heat-up and temperature stabilization time, before the intended growth can commence. To avoid these problems, all SAG in this chapter was performed at a temperature of 960°C or lower. The benefit of the lower temperature is that it prevents desorption of material from unmasked areas during heat-up. Without material desorption, there is no Ga species in the gas phase that can cause growth at the mesa edges, before the start of the intended growth.

The selective area growth was performed by MOCVD, using the precursors trimethylgallium (TMGa), trimethylaluminum (TMAl), and ammonia. The growths were performed in H_2 carrier gas, at a pressure of 100 Torr and an ammonia partial pressure of 25 Torr. The planar GaN growth rate was 0.94 Å/s, as calibrated on a planar sample. For growth of $Al_{0.1}Ga_{0.9}N$, the TMAl flow was set to give an aluminum composition of 0.1 for planar growth, resulting in a growth rate of 1.05 Å/s. The growth temperature was either 960°C or 920°C. Di-silane was used as the Si-precursor when Si doping was performed. After growth the mask was removed; buffered HF was used for the SiO_2 masked samples, and boiling NH_4OH was used for the AlN masked samples.

The mask pattern had an overall large 'fill-factor', i.e. most of the sample was unmasked. The features used in the present study consisted of masked stripes of widths 5 μm 10 μm, 20 μm, and 50 μm, each located 200 μm or more away from the nearest masked feature. The stripes were aligned in the $\langle 11\bar{2}0\rangle$ direction of the underlying GaN film. This orientation was chosen because it tends to produce more stable sidewalls than stripes in the $\langle 1\bar{1}00\rangle$ direction, for SAG on planar samples.[2] Furthermore, in §3.3 it was shown that heating a sample to 960°C prior to growth resulted in smooth sidewalls for mesas in the $\langle 11\bar{2}0\rangle$ direction, and rough side walls for mesas in the $\langle 1\bar{1}00\rangle$ direction. A smooth sidewall is necessary to achieve smooth vertical regrowth interfaces needed for device applications.

4.3 Growth Evolution - GaN

To study the evolution of non-planar SAG of GaN, a technique of repeated interrupted growth was employed. Four samples were grown under identical conditions, while the growth time was increased in equal steps. The growths, performed at 960°C, resulted in planar thicknesses of 43 nm, 85 nm, 128 nm, and 170 nm, respectively. Atomic force microscopy (AFM) was used to measure the profile of the growth near the masked mesa for each sample. Fig. 4.1 shows the AFM profiles obtained near a 10 μm SiO_2 mask stripe. Each profile is a 'snap-shot' of the growth front in time, and the profiles together show the time evolution of the growth. At a

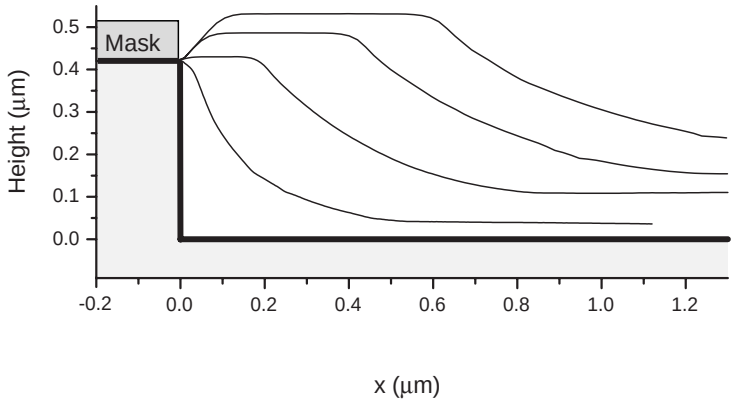

Figure 4.1: Atomic force microscopy line scans of growth profiles near a 10 μm SiO_2 mask stripe. The profiles are from four samples with corresponding planar thicknesses of 43 nm, 85 nm, 128 nm, and 170 nm, respectively. The thick line represents the GaN surface prior to growth.

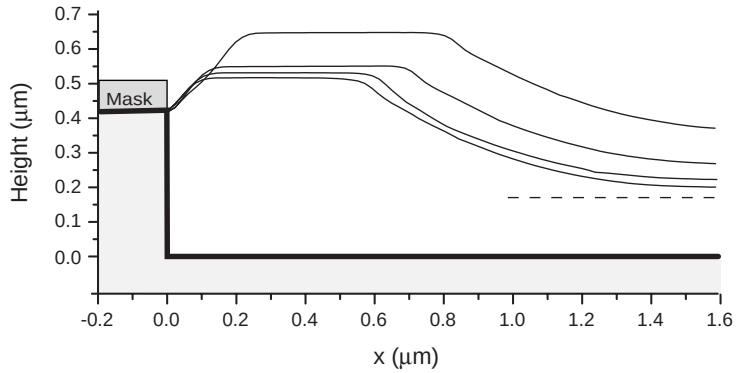

Figure 4.2: Atomic force microscopy line scans of growth profiles of a sample of 170 nm planar growth thickness. The curves correspond to four different mask stripe widths: from top to bottom 50 μm, 20 μm, 10 μm, and 5 μm. The dashed line represents the planar thickness far from masked areas.

distance of 1.3 μm from the mesa edge the growth was relatively planar, but closer to the mesa the growth was more rapid, and non-planar in nature. A c-plane terrace developed over time, extending above the original sample level. To study the influence

of the mask stripe width, AFM profiles were obtained near stripes of varying widths, on the sample with 170 nm planar thickness. The results are plotted in Fig. 4.2; from top to bottom the curves correspond to stripe widths of 50 μm, 20 μm, 10 μm, and 5 μm. In Fig. 4.2, an increase in growth rate with increased stripe width is evident. In the nearly planar region ($\sim 1.6\mu$m from the mesa edge), the increase in growth rate relative to the growth rate far from the mesas was of a factor 2.2, 1.6, 1.3, and 1.2, for the mesa widths 50 μm, 20 μm, 10 μm, and 5 μm, respectively. Since the increase in growth rate near the mesas depended strongly on the mesa width, it can be concluded that the growth rate enhancement is due to diffusion of growth species from the mask. This effect is normal for SAG, and typically has a range on the order of 20 μm or more.[2, 24] Given the magnitude of the range, compared to the small lateral scale of interest in the present study, it is clear that the growth rate enhancement from the mask is nearly constant in the entire near-mesa region. It can therefore be concluded that the rapid growth within ~ 0.8 μm of the mesa compared to a distance of 1.6 μm, visible in both Fig. 4.1 and Fig. 4.2, can not be an effect of diffusion of growth species from the mask.

To explain the growth evolution observed in Fig. 4.1, the non-planar nature of the growth must be considered. At the start of the growth there were two growth surfaces present, the bottom surface and the etched sidewall, both subject to deposition once the growth started. The structure grew fast in the lateral direction, exceeding the planar growth rate by a factor of ~ 3. Once the lateral growth progressed, a

slow-growing c-plane terrace developed near the mask edge. Similar terraces were observed near the mask for SAG on planar samples by Li *et al.*.[24] If adsorbed growth species have adequate energy to diffuse, local growth rate variations may occur between planes of different crystallographic orientation,[25] due to a difference in thermodynamic driving force. In this thermodynamically limited regime, the slow-growing planes tend to expand in area, on the expense of faster-growing planes. The c-plane of GaN is known to be slow growing, so the appearance and expansion of the c-plane terrace in Fig. 4.1 is a sign of thermodynamically limited growth.

The appearance of the c-plane terrace, extending above the original mesa level, can cause problems in the intended device applications. If non-planar SAG is performed at the source of a HEMT, and the gate needs to be placed close to the regrowth edge, the terrace can cause interference with the lithography, in particular for e-beam lithography of very short gates. The main tool to avoid growth above the mesa level is growth time. For growth conditions that produce controlled growth near the mesa edge, the formation of a c-plane terrace is inevitable, but by limiting the growth time, the height of the terrace can be limited. A height of up to 100 nm is acceptable, which limits the growth to a planar thickness of about 170 nm for a 10 μm stripe width. Some variations in the growth conditions were tried, including changed ammonia flow, changed growth rate, higher pressure, and lower temperature, but in all cases the formation of the c-plane terrace was inevitable. By going to

higher temperature, the formation of the c-plane terrace can be avoided (see §4.7), but that also compromises the control of the growth near the mesa.

In the GaAs and InP material systems, marker layers consisting of alloys, typically AlGaAs and InGaAs, have been used to study non-planar growth evolution, see for example refs. [25, 26]. After growth the cross-section is stain-etched, which creates contrast in optical microscopy and SEM, and gives beautiful direct images of the growth evolution. This method could unfortunately not be used in the present study. Currently, the only GaN alloy that can be used for selective area growth is AlGaN, and its growth behavior is different from that of GaN, and would therefore perturb the GaN growth if used as a marker layer. Furthermore, I am not aware of any suitable stain-etch that could be used to create a contrast between GaN and AlGaN.

4.4 Growth Evolution - AlGaN

Similar to the previous section, the growth evolution of AlGaN during non-planar SAG was studied by performing interrupted growths. $Al_{0.1}Ga_{0.9}N$ was deposited using the same growth conditions as for the GaN growth. The growth rate was slightly higher, and the growth times were adjusted to compensate for this. As before, the four incremental growth times were chosen to give planar thicknesses of 43 nm, 85 nm, 128 nm, and 170 nm. A different approach was taken for the charac-

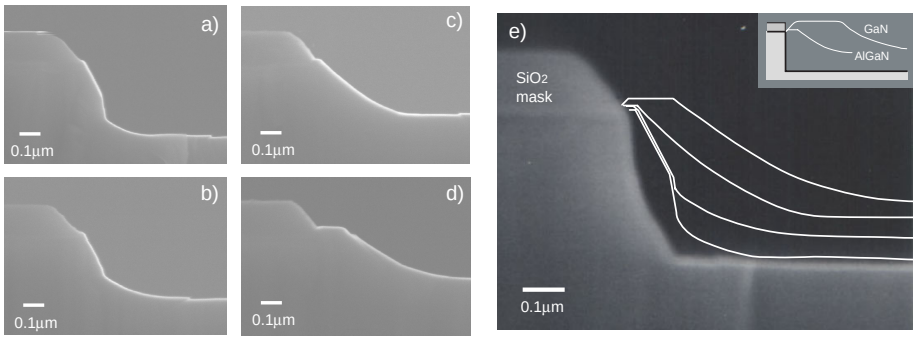

Figure 4.3: a - d) SEM micrographs of $Al_{0.1}Ga_{0.9}N$ SAG in etched areas near a 10 μm SiO_2 mask stripe. The growth time for each sample corresponds to four different planar thicknesses: a - 43 nm, b - 85 nm, c - 128 nm, and d - 170 nm. e) the profiles of all four samples, represented with lines, have been combined. Inset shows size comparison on GaN and AlGaN growth (planar thickness 170 nm).

terization. The AlGaN growths resulted in steeper profiles near the mask edge, and it was believed that using AFM profiling would not give fully reliable measurements. Instead, the samples were cleaved and were examined in cross-section by SEM. The SEM micrographs of the individual samples are shown in Fig. 4.3a-d. Note that the SiO_2 mask had not yet been removed at the time. For better visualization, lines were drawn along the profile edge of each sample, and were combined in one plot, shown in Fig. 4.3e. The lines are superimposed on an SEM image of one of the samples before growth, from which it is evident that the reactive ion etch did not produce perfectly vertical sidewalls. The inset in Fig. 4.3e is a scale comparison of the GaN and the AlGaN growth, for the same planar thickness of 170 nm.

The AlGaN growth overall showed similar features to the GaN growth. Material deposited both on the bottom surface and on the mesa sidewall, leading to a com-

plex behavior near the mask edge. The most striking difference is the low lateral growth rate of the AlGaN; the average lateral growth rate was only about a factor 1.5 higher than the planar growth rate. Similar to the GaN growth, a c-plane terrace developed also during the AlGaN growth, but at a much later stage, due to the slow lateral growth rate. The terrace was very narrow, also a consequence of the slow lateral growth rate. Growth of AlGaN is in general associated with a shorter surface diffusion length than GaN, visible for example in shorter step-lengths during planar step-flow growth. In this context it is tempting to attribute the low lateral growth rate to a diffusion limiting process, but such a conclusion can not be drawn from the present experiments. A long surface diffusion length can only ensure that the thermodynamically favored growth planes grow faster; if all surfaces are equally favored, the growth rates will be the same regardless of the magnitude of the surface diffusion length. As a matter of fact, in the two samples with the shortest growth times, Fig. 4.3a-b, a clear facet, with an angle of 62° to the c-plane, is evident. Facet formation, and the associated very slow growth rate, is a sign of thermodynamically limited growth. Similar slow growing planes, labelled 'non-growth' planes, have been observed for non-planar GaAs growth.[25] The angle 62° corresponds to the $\{1\bar{1}01\}$ facet, a facet that often occurs during 3-dimensional growth of GaN, for example during island growth on a low temperature nucleation layer, or during regular SAG on $\langle 11\bar{2}0\rangle$ oriented striped.[2] For AlGaN growth the $\{1\bar{1}01\}$ surface has been reported to be particularly stable, resulting in very sharp facets.[13]

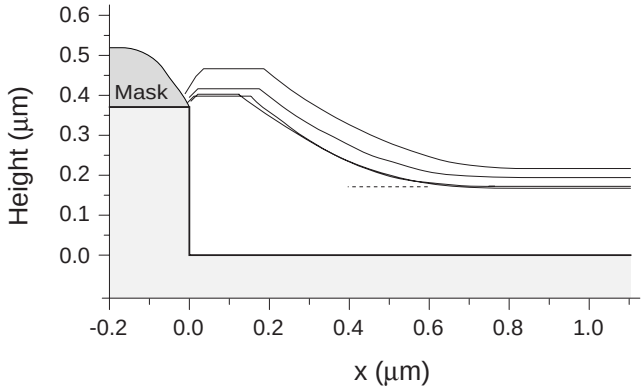

Figure 4.4: Growth profiles on an $Al_{0.1}Ga_{0.9}N$ non-planar SAG sample of 170 nm planar growth thickness. The profiles, obtained by SEM, correspond to four different mask stripe widths: from top to bottom 50 μm, 20 μm, 10 μm, and 5 μm. The profiles for 10 μm and 5 μm are nearly identical. The dashed line represents the planar thickness far from masked areas, based on growth rate calibrations.

So far, diffusion on the growth surface has been discussed, but the diffusion on the mask is a different issue. Enhanced growth rate due to diffusion from the mask was observed for GaN growth, but this effect was much smaller for the AlGaN growth. Fig. 4.4 shows the growth profiles obtained from the sample with 170 nm planar thickness, for different mesa widths. The profiles were measured by SEM, and combined in the same way as Fig. 4.3e. At a distance of 1 μm from the mask edge the growth rate was nearly the same as the planar growth rate, for mesa widths of 5 and 10 μm. For 20 μm and 50 μm some enhancement in the growth rate was observed, but it was far less than for GaN growth. The low growth rate enhancement indicates that large amounts of material must have deposited on the mask. No obvious signs of mask deposition was visible after growth, but other observations suggest

that deposits did occur. When examining the cross-sectional SEM images taken of samples prior to mask removal, it appeared that the masks of the samples with thick AlGaN growth had gained in thickness during growth. Moreover, when attempting to remove the SiO_2 mask after AlGaN growth, it was found that the standard technique, proven for mask removal from GaN SAG samples (buffered HF etch), did not work. After a long soak in buffered HF, cracks appeared in the mask, getting wider with time, but complete removal was not achieved. A new technique was developed, on the assumption that the mask after growth was covered with a thin layer of AlN or AlGaN. The samples were etched in boiling NH_4OH for 10 min, an effective etchant for amorphous AlN, followed by the standard etch in buffered HF. This technique proved effective in removing the mask completely. This strongly supports the idea that mask depositions occurred during growth.

Selectivity is of great concern for AlGaN selective area growth, due to the extremely low vapor pressure of AlN at typical growth temperatures. In previous reports of AlGaN SAG, involving thick layers or high Al-composition, mask depositions were observed.[2, 10] However, for thin AlGaN layers there are no reports of poor selectivity.[11, 12, 13] From our results it appears that growth of thin layers at a relatively slow growth rate gives rise to smooth mask depositions, that easily go undetected in optical microscopy. For most applications, mask depositions are not a problem, as long as the mask can be removed after growth.

4.5 AlGaN Composition Gradient

In the previous section the non-planar AlGaN growth near the mesa edge was studied. The nominal Al composition far from the mesa was 0.1, but near the mesa the non-planar nature of the growth, in combination with Ga diffusion from the mask, may have altered the Al composition.

To study the Al composition in the near-mesa region, a sample was grown similar to the 170 nm sample from the AlGaN growth evolution study (§4.4), with the exception of a 5×10^{18} cm^{-3} Si doping level. It was sent to a research group at Otto-von-Guericke Universität Magdeburg, for characterization by spectrally resolved cathodoluminescence (CL) microscopy. In the CL imaging mode the focused electron beam is scanned over the area of interest, and a complete CL wavelength spectrum is recorded in each point. The resulting three-dimensional data set is evaluated ex situ and can produce local spectra, sets of monochromatic CL images, as well as CL wavelength images (CLWI) mapping the emission wavelength of the local maximum CL intensity each sampling point.[27] The CL study was performed at a temperature of 4 K.

The CL measurements were obtained from the top surface of the sample, and therefore only serve to quantify the properties of the top portion of the growth. The probe depth, as well as the lateral resolution, is determined by the generation volume for electron-hole pairs, as given by the Bethe range. For the primary energy used

for the measurements, 5 keV, the resolution is estimated to about 100-200 nm. The CL intensity from the sample cross-section was too low to allow measurements. However, for applications to AlGaN/GaN HEMTs, the transition from the regrowth into the active parts of the device should occur within $\sim$ 50 nm from the surface, making the material properties at shallow depths most important.

The growth around a 2 μm masked mesa was examined. $Al_{0.1}Ga_{0.9}N$ growth near 5 μm and 10 μm mesas had very similar profiles (see Fig. 4.4), and it is assumed that growth at the 2 μm mesa is very similar too. Fig. 4.5a shows an SEM image of the mesa, in plan view. In Fig. 4.5b, the corresponding CL intensity image is shown, mapping the spectral region of GaN and AlGaN. Higher emission intensity was detected in the Si-doped AlGaN than in the GaN in the mesa. Fig. 4.5c is a plot of the emission energy of the local maximum CL intensity, as a function of lateral position along a line across the mesa. The position of the line is marked with a white line in Fig. 4.5a. At a distance of $\sim$ 0.6 μm or more from the mesa edge, the emission maximum occurred at an energy of 3.670 eV, which corresponds to an Al composition of 10 %, assuming zero strain. Within $\sim$ 0.6 μm of the mesa edge, the emission maximum was at 3.612 eV, which corresponds to an Al compositions of $\sim$ 7 %.

Due to the high Al-N bond strength, adsorbed Al species are believed to be much less mobile than adsorbed Ga species during growth. This result in a much shorter diffusion length of Al compared to Ga. Diffusion of growth species can

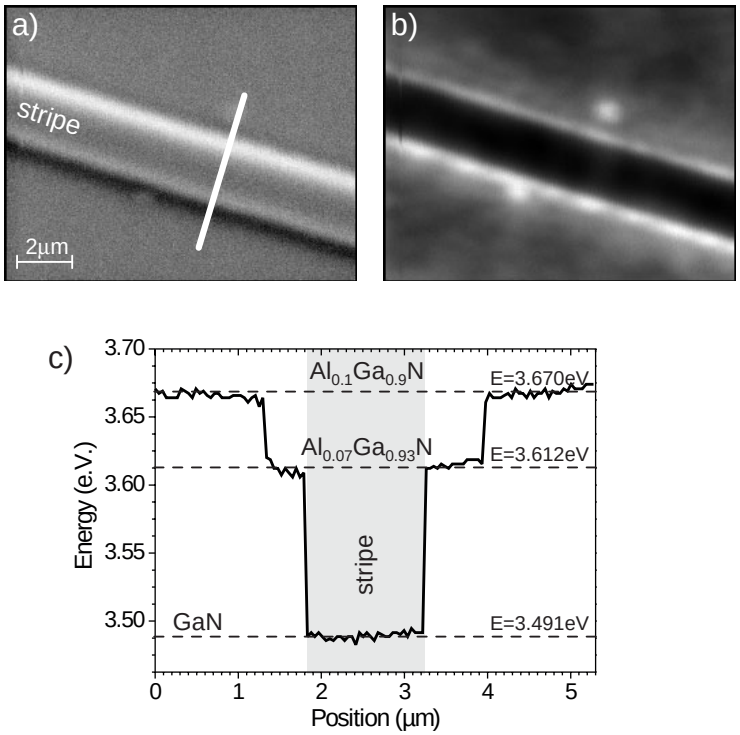

Figure 4.5: Cathodoluminescence study of $Al_{0.1}Ga_{0.9}N$ non-planar SAG at a 2 μm wide masked mesa. a) SEM image. b) CL intensity image of the entire spectral region. c) Plot of the emission energy of the local maximum CL intensity, as a function of lateral position across masked mesa. The position of the line-scan is marked in a). The grey box marks the mesa.

---

cause increased growth rates on surfaces where the thermodynamic growth rate limit is higher than in the surrounding areas. Since more Ga than Al can diffuse to cause a local growth rate increase, the growth rate increase is also associated with an increased Ga mole fraction, which causes the Al composition to decrease. To lower the Al composition from 10 % to 7 %, as was observed at the mesa edge, the binary GaN growth rate would have to increase by 48 %, assuming a constant binary AlN growth rate, which would result in a 43 % increase in the total growth rate.

Studying the $Al_{0.1}Ga_{0.9}N$ growth evolution shown in Fig. 4.3, it can be seen that the average lateral growth rate was a factor $\sim$1.5 higher than the planar growth rate, which would account for the decrease in Al composition. The growth rate is high in a region within $\sim$0.6 μm of the mask edge, which matches the region of lower Al composition in Fig. 4.5.

In an experiment by Kato *et al.*[13], AlGaN SAG was performed on mesas with triangular cross section, prepared by ELO on masked striped oriented in the $\langle 11\bar{2}0\rangle$ direction. The Al composition was examined by CL, and it was found to depend on the position on the $(1\bar{1}01)$ facet, ranging from 18 % at the top of the $\sim$ 13 μm high triangular mesa, to 5 % at the base. The strong gradient was attributed to a large difference in diffusion lengths of Ga and Al species.

The results in the present experiment indicate that a well controlled Al composition can be achieved in the near mask region. To reach a certain Al composition, the planar growth must be of a somewhat higher nominal Al composition. However, given the 100 - 200 nm resolution of the measurement, there is still the possibility of compositional fluctuations on a smaller scale. Of particular concern is the observation of a $(1\bar{1}01)$ 'non-growth' surface in §4.4. Analogous to the previous reasoning, the very low growth rate of the $(1\bar{1}01)$ facet may give rise to a locally very high Al composition. Due to the location of the $(1\bar{1}01)$ surface in the way of the intended current path, a high Al composition could cause problems.

4.6 Impurity Incorporation

Conductivity measurements were used to quantify the n-type impurity level in the material. Direct measurements of the impurity concentration or carrier concentration would be preferable, but these quantities were deemed too difficult to measure on the small lateral scale of interest. The measurements were performed using the transmission line model (TLM). In this method, the resistance *per unit length* of a slab of material is measured. The inverse is conductance times unit length (unit S·μm), and will be referred to as just 'conductance' in this section. By normalizing the conductance to the slab width, the sheet conductance is obtained, carrying the unit S·□.

The impurity incorporation during non-planar selective area growth, and the role of autodoping from the mask, was studied with a set of samples grown on semi-insulating base-layers. One sample was actively doped with Si, while four samples were grown nominally undoped. Among the four undoped samples, two different mask materials, SiO_2 and AlN, and two different growth temperatures, 960°C and 920°C, were used. The samples are summarized in Table 4.1. The samples were grown to a planar thickness of 128 nm, corresponding to the second highest curve in Fig. 4.1. The mask was removed after growth, followed by formation of ohmic contacts. For the Si-doped sample, the contacts were formed directly on the sample, by evaporating and annealing metals as described in ref. [28]. Good ohmic contacts

Table 4.1: Summary of samples for conductivity measurements. The sheet conductance was measured at various distances x from the mask edge.

Sample	Mask	Temp. (°C)	Si doping (cm^{-3})	Sheet Conductance ($\mu S \cdot \square$) at position x		
				$x \sim 40$ μm	$x = 1$ μm	$x \in$ [0-0.4] μm
A	SiO_2	960	1.5×10^{18}	710	1170	3600
B	SiO_2	960	-	61	380	2300
C	AlN	960	-	11	120	940
D	SiO_2	920	-	8.6	145	3200
E	AlN	920	-	7.8	81	420

could not be formed directly to the four undoped samples, due to the low carrier concentrations. Instead, regrown contacts were fabricated, by n^+-GaN mass transport regrowth (see §5.2) followed by metal deposition and anneal. With the regrown ohmic contacts nearly all contacts showed ohmic characteristics.

The conductance was measured with two types of TLM structures, one for the near-mask region, and one for regions far from masked areas. The latter was a standard large area TLM pattern, located ~ 40 μm from the nearest masked region. For measuring the near-mask conductance, a more complicated test structure was employed, consisting of narrow etched mesas positioned near the regrowth edge, etched to a depth of 0.5 μm. One such etched mesa is illustrated in cross-section in Fig. 4.6a. The etch isolates a small section of regrown material, and by fabricating a TLM pattern along the etched mesa, the conductivity of the regrown material could be measured. Fig. 4.6b shows the SEM image of an etched mesa near a TLM contact pad. Each die on the samples contained eight TLM patterns, each on a separate

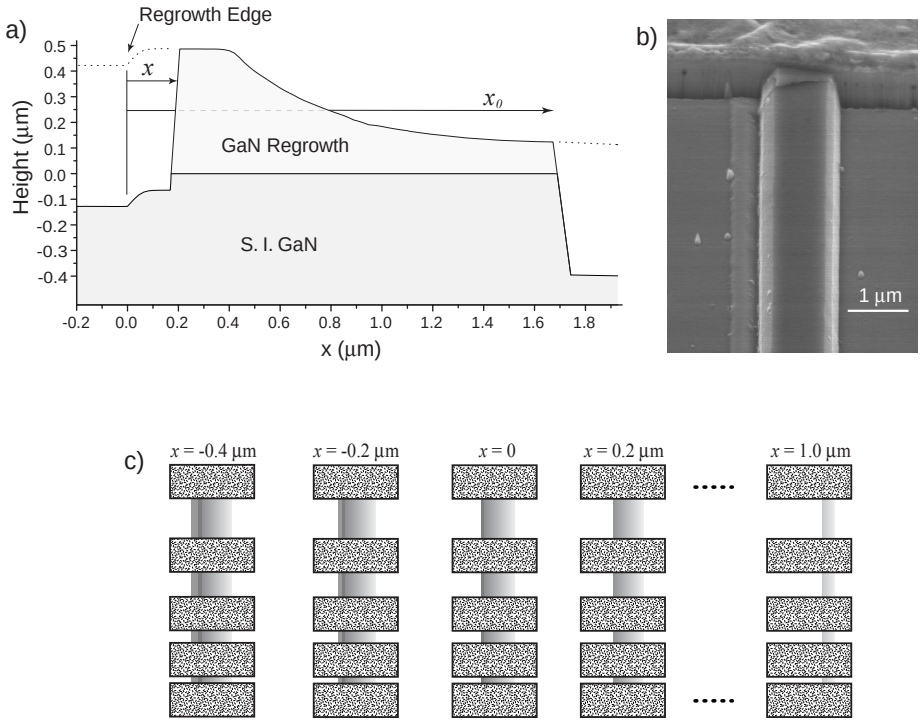

Figure 4.6: Test structure used for measuring conductivity of the selective area growth near the mask edge. a) Schematic of the cross-section. The dotted curve represents the regrown sample surface before etch. In the experiment, x_0 was held constant at 1.7 μm, while x was varied between -0.4 and +1.0 μm. b) SEM image of an etched mesa near a TLM contact pad. c) Schematic of layout of TLM structures in a die (not to scale). The die contained eight TLM patterns, each along a separate etched mesa, with x going from -0.4 μm to 1.0 μm in steps of 0.2 μm.

---

etched mesa, as illustrated schematically in Fig. 4.6c. The dimension x_0, defined in Fig. 4.6a, was the same for all eight TLM patterns (1.7 μm), while x was varied between -0.4 μm and 1.0 μm in steps of 0.2 μm. This allowed the *sheet conductance* in each 0.2 μm incremental slice of material to be calculated as the difference in conductance between two adjacent TLM patterns. Seen differently, when plotting the conductance as a function of x, the sheet conductance could be obtained in any

point as the slope of the curve (with opposite sign). To increase the number of data points, measurements from two or more dies were combined for each sample. The alignment of the mesa to the regrowth was varied on purpose between dies, creating offsets in x and x_0 between measurements from different dies. To obtain correct x values, the actual alignment for each die was measured by SEM. A conductance offset was added to measurements from different dies, to compensate for different values of x_0. The offsets were chosen for best fit between points from different dies.

First, the sheet conductance far from the masked stripes was studied. The results are summarized in Table 4.1, in the column labelled "$x \sim 40$ μm". The Si doped sample *A* showed the highest sheet conductance of 710 μS·□. The carrier concentration was $\sim 1.5\times10^{18}$ cm^{-3}, based on doping calibrations on a planar sample. To reach the measured sheet conductance of 710 μS·□, a 128 nm thick film with a carrier concentration of 1.5×10^{18} cm^{-3} would have to have a mobility of 230 cm^2/Vs, which is reasonable for that carrier concentration.[29] Sample *B*, grown nominally undoped but under the same conditions as sample *A*, showed a much reduced sheet conductances of 61 μS·□. Clearly, most of the conductance measured in sample *A* was a result of the intentional Si doping, not of autodoping from the mask. For the nominally undoped sample *B* however, most of the conductivity was a result of autodoping from the mask, as is clear from comparison to sample *C*. Sample *C* was grown under identical conditions to sample *B*, but it had an AlN mask, a material not conducive to autodoping. The sheet conductance of sample *C* was measured to

11 μS·□, a factor 6 lower than the SiO_2 masked sample *B*. As the growth temperature was lowered by 40°C, for sample *D* and *E*, the difference between SiO_2 mask and AlN mask was negligible, with sheet conductances of 8.6 μS·□ and 7.8 μS·□, respectively. This shows that autodoping had very little effect far from the mask at 920°C.

Next, the conductivity near the mask edge was studied with the test-structure shown in Fig. 4.6. The resulting conductance *vs. x* plots for samples *A*-*E* are shown in Fig. 4.7. The results present a more complex picture than the measurements far from the mask. The total conductance stayed relatively constant in all samples for $x < 0$, indicating highly resistive material in this region. This is expected since the material in this region was the original semi-insulating GaN film. For $x > 0.5$ μm the conductances showed constant slopes, which translates into constant sheet conductances. The value of these sheet conductances are included in Table 4.1 in the "x = 1 μm" column. In the $0 < x < 0.4$ μm region the slopes were higher, to varying degrees. Curves were fitted to the data points for $x > 0$, using a function with a linear component based on the slope at x = 1 μm, plus an arbitrary function to best fit the $0 < x < 0.4$ μm region. The slope in the steep region near the mask depended to some extent on the choice of fitting function, making the slope in any specific point an inaccurate measure of the sheet conductance. Instead, the *average* slope between 0 and 0.4 μm was used to quantify the near-mask sheet conductance. These average values are presented in the far right column of Table 4.1. A graphic representation

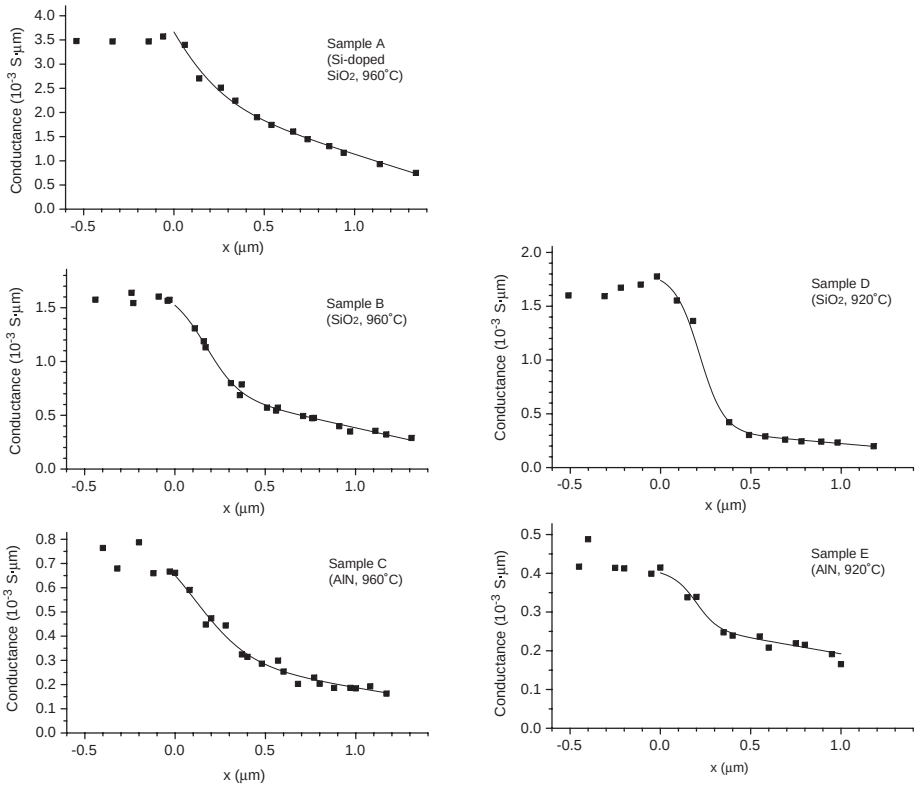

Figure 4.7: Measurement of conductance of narrow etched mesas at regrowth edge, as a function of the alignment *x*. The alignment parameter *x* is defined in Fig. 4.6a.

---

of the sheet conductances is shown in Fig. 4.8. Here, the negative derivatives of the fitted curves from Fig. 4.7 were used for $0 < x < 1.3$ μm, and the large area TLM measurements were included for large *x*.

Some general trends for the sheet conductances can be identified. Sample *A* (the Si doped sample) showed a modest increase in sheet conductance near the mask, compared to far from the mask. At $x = 1$ μm and in the range $0 < x < 0.4$ μm the increase was of a factor 1.6, and 5, respectively. The undoped samples showed a more drastic increase; among the samples the increase at $x = 1$ μm was of a factor

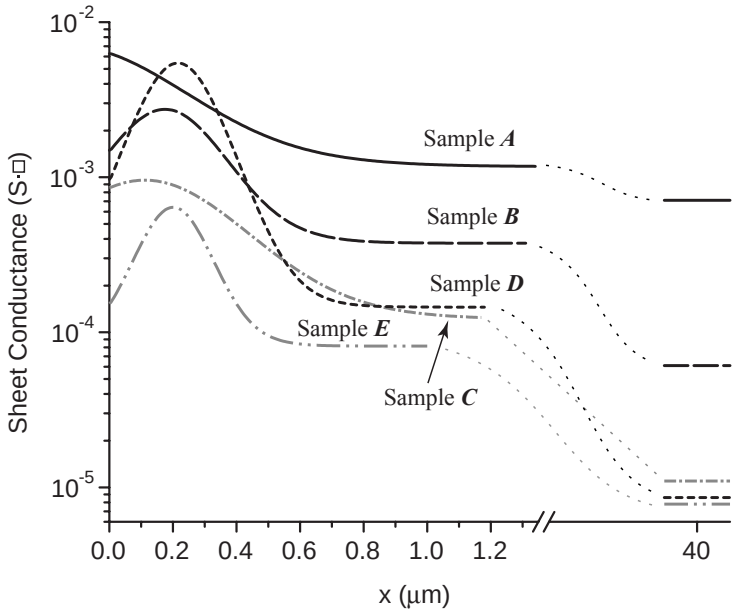

Figure 4.8: The sheet conductance of samples *A* - *E* as a function of the distance *x* from the mask edge. The curves for $x < 1.3$ μm are calculated from the slope of the fitted curves in Fig. 4.7.

---

between 6 and 16, and in the range $0 < x < 0.4$ μm the increase was of a factor between 40 and 85. This observation includes the samples with AlN masks, and since AlN should not exhibit auto-doping effects, it can be concluded that auto-doping from the mask was not the main effect responsible for the increased sheet conductance near the mask edge. However, it appears that auto-doping accentuates the effect, since the SiO_2 masked samples show higher sheet conductances than the AlN masked samples do near the mask, in particular in the $0 < x < 0.4$ μm range.

Sheet conductance is an areal quantity; if the conductivity was uniform throughout the *thickness* of the regrowth, then the thicker regions should exhibit a higher sheet conductance. At first this would seem to explain the higher sheet conductances

measured near the mask edge, where the regrowth is much thicker than far from the mask. However, the thickness profile in Fig. 4.1 does not match the sheet conductance profiles. Most of the thickness increase occurred between 0.5 um and 1.3 μm from the mask, but the sheet conductances stayed largely constant in this range. This rules out the increased thickness as a major contributor to the high near-mask sheet conductance. Another possible source of conductance is impurity contamination of the etched sidewall prior to growth. However, such contamination would show up as a high sheet conductance at $x = 0$, and not over the whole $0 > x > 1.4$ μm range as is observed in the samples.

The most probable origin of the high sheet conductance near the mask is a higher incorporation efficiency of dopant species due to the orientation of the growing surfaces. Far from the mask the growth is planar, with a relatively well known impurity incorporation. The growth near the mesa is by nature non-planar, and the surfaces involved may incorporate impurities differently than the c-plane surface. Comparing the growth profile in Fig. 4.1 with the sheet conductance *vs.* x plot in Fig. 4.8, we see that in the intermediate conductance region (0.5 μm $< x <$ 1.3 μm), the growth surface has a moderate slope of less than 30° relative to the c-plane. In the high conductance region ($0 < x <$ 0.4 μm), much steeper slopes are present. The incorporation efficiency of Si on c-plane GaN is on the order of one, and can therefore not be much higher for other orientations. The incorporation of oxygen on the other hand, has been shown to be thermodynamically limited,[30] and can therefore

be expected to show orientation dependence. For planar high temperature growth in our reactor, the gas phase residual impurities are not capable of causing appreciable n-type carrier concentrations (see §2.3.5). For growth on differently oriented surfaces however, the residual impurities, in combination with impurity species desorbing from the mask (for SiO_2 masking), may be sufficient to cause significant n-type conductivity. Large variations in impurity incorporation have been observed for InP and GaAs when growing on differently oriented substrates.[31, 32] No such experiments have been performed for GaN, due to the difficulty in growing GaN of other orientations than c-plane. However, some evidence of increased impurity incorporation on the $\{1\bar{1}01\}$ facet has been reported.[33, 34] ELO samples grown by HVPE were examined in cross-section by cathodoluminescence microscopy and micro-Raman spectroscopy, and it was found that regions where growth occurred in the $\langle 1\bar{1}01\rangle$ direction had an order of magnitude or more higher free carrier concentration than regions growing in the $\langle 0001\rangle$ direction. Given these observations, it is reasonable to assign the high conductivity near the mask to enhanced impurity incorporation, caused by the different surface orientation during growth.

4.7 Low-Profile Selective Area Growth

So far in this chapter the SAG has been performed at temperatures of 960°C or lower, to enable controlled doping or alloy composition in the near-mesa region.

In this section a SAG technique performed at high temperature, is presented. The technique is, in a way, a hybrid between the non-planar SAG presented so far in this chapter, and the mass-transport growth of the previous chapter. The purpose was to develop a 'low-profile' growth technique, that does not extend much above the original sample surface, while still allowing a large lateral extent of the growth. This is required for certain ohmic contact regrowths, where a spacing is necessary between the metal edge of the contact and the regrowth edge (see §5.1.1).

The temperature and conditions were chosen similar to the mass-transport growth technique: 1060°C, 100 Torr pressure, and a gas flow of 6 slpm NH_3 and 6 slpm H_2. Before the TMGa was injected, the sample was briefly heated up to 1090°C, to ensure maximum mass-transport growth at the mesa edge. After the short 1090°C anneal, TMGa was injected for the remainder of the growth, to supply growth species for extended lateral growth. At the temperature chosen, which is the typical growth temperature for planar growth, considerable desorption occurs from c-plane GaN. For regular planar growth, the desorption is countered by a large supply of TMGa, causing net growth to occur. For the present SAG technique, a low TMGa flow was chosen, low enough to prevent net growth on the c-plane, while high enough to cause positive lateral growth.

Fig. 4.9 shows the growth profiles of growths performed with a TMGa flow of 15 μmole/min, for 10 min and 30 min. The 30 min profile was obtained by AFM, and the 10 min profile by SEM. For better visualization, the *x* axis has been compressed

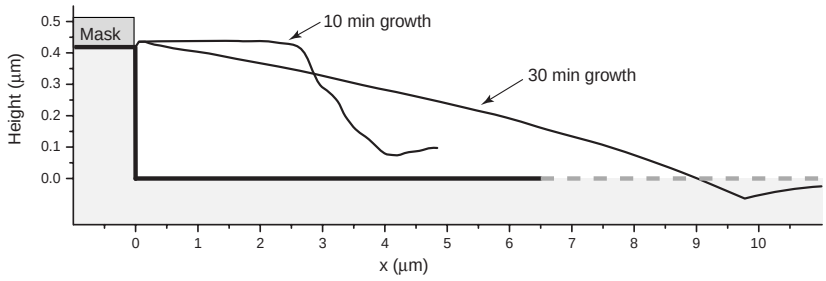

Figure 4.9: Low-profile selective area growth of GaN. Virtually no growth occurred on the bottom surface. Note that the lateral and vertical scales are not the same.

---

with a factor 5 relative to the vertical axis. The TMGa flow used would give a growth rate of $\sim$ 1 Å/s, in the absence of desorption. For device application purposes (see §5.4), the growths were finished with a 20 nm $Al_{0.35}Ga_{0.65}N$ cap layer, deposited at a temperature of 960°C. The 10 min growth extended nearly 3 μm from the mesa edge, while maintaining a flat c-plane top-surface. The 30 min growth extended nearly 10 μm from the mesa edge, and the top-surface assumed a slanted profile. The lateral growth appeared to be proportional to the growth time, resulting in a relatively constant growth rate. The growth extended $\sim$ 30 nm above the original sample level, mostly due to the AlGaN deposition. When performing another 10 min growth, with twice as high TMGa flow (30 μmole/min), and without the AlGaN cap layer, the growth extended nearly 100 nm above the original sample level. This indicated that the limit between the desorption regime, and the growth regime of the c-plane GaN, occurred somewhere between a TMGa flow of 15 and 30 μmole/min. The experiment shows that excellent low profile growth can be obtained, if the TMGa

flow is low enough. A step of 30 nm at the regrowth edge is acceptable for device applications, while steps of 100 nm and above may interfere with subsequent gate lithography and alignment. For the ohmic contact application in §5.4, the lower flow of 15 μmole/min, and a growth time of 30 min, was used.

A few words should be mentioned about the 20 nm $Al_{0.35}Ga_{0.65}N$ growth. In a separate experiment, a thicker $Al_{0.35}Ga_{0.65}N$ cap was grown, and was studied in cross-section by SEM. By comparing the sample thickness before and after AlGaN deposition, the growth rate of the AlGaN deposition was estimated, and it was found to be uniform over the sample surface. That is to say, the same growth rate was obtained on the mask and in the mask openings, indicating that the growth was not selective. For the 20 nm layer, mask removal could be obtained despite of the AlGaN mask deposits, using the mask removal technique described in §4.4.

For the intended application of ohmic contact regrowth, heavy n-type doping of the GaN is necessary. It was found that relatively high Si doping with DiSilane flow was possible, without disrupting the growth morphology. The absolute value of the doping concentration was not measured, nor can it be calculated from the injected DiSilane flow, since the growth rate/direction is ill-defined. For the contact regrowth experiment described in §5.4, the maximum DiSilane flow allowable before morphology degradation occurred, was used.

4.8 Summary

The growth evolution of non-planar selective area growth of GaN and $Al_{0.1}Ga_{0.9}N$ was studied at a growth temperature of 960°C. Growth occurred both on the bottom surface of the open areas, and on the etched mesa sidewalls, resulting in features extending above the original GaN mesa level. For GaN growth, a lateral to vertical growth rate ratio of ~ 3 was observed, while the ratio was only ~ 1.5 for $Al_{0.1}Ga_{0.9}N$ growth. An enhanced growth rate due to diffusion of growth species from the mask was observed for GaN growth, but the effect was relatively small for mask stripes of width up to 10 μm. Much smaller mask-related growth rate enhancement was observed for the $Al_{0.1}Ga_{0.9}N$ growth, due to poor growth selectivity, which resulted in mask depositions. The Al composition of the AlGaN growth was investigated, with spectrally resolved cathodoluminescence microscopy. It was found that a sample with 10% Al composition far from the mask, had a composition of only 7% in the 0.6 μm closest to the mesa edge. The impurity incorporation during non-planar SAG of GaN was investigated with various TLM measurements, on samples with SiO_2 masks and AlN masks. The impurity incorporation was found to be greatly enhanced near the mask edge, in part due to autodoping from the mask (for the SiO_2 masked samples), and in part due to the non-planar nature of the growth near the mask.

A low-profile selective area growth technique was also developed, in which

the benefits of both non-planar SAG, and mass-transport growth, were combined. The external supply of growth species allowed the growth to extend up to 10 μm from the mask edge, and the use of reactor conditions similar to the mass-transport growth conditions ensured that vertical growth above the original sample surface was avoided.

4.9 Future Work

The growth evolution studies in this chapter, preformed by multiple interrupted growths, provided valuable insight, but were cumbersome and time consuming to perform. In the GaAs and InP material systems, a much simpler technique has been used, involving marker layers, consisting of alloys, typically AlGaAs and InGaAs.[25, 26] AlGaN or InGaN would not work as marker layers for nitride growth, since the growth mode would be affected, or it would require a low growth temperature. Instead, Si-doping could be used to mark layers, since a moderate concentrations of Si does not alter the growth mode. The problem lies in developing a wet-etch that can selectively stain the Si-doped layers, or the undoped layers. Photo-electro-chemical (PEC) etching is know to be sensitive to the conductivity type, and for properly optimized etch conditions, a working stain-etch could perhaps be developed. Mg doping, or Fe doping, can not be used to mark layers, due to the slow doping response. However, it would be possible to dope the entire structure with

either of these dopants, and co-dope with Si in the marker layers, to create stronger conductivity contrasts between the marker layers and the layers in between.

Similar to the mass-transport growth, all non-planar selective area growths were performed on samples with etch depth 0.4 μm. Growth on samples with other etch depths should be explored as well.

References

[1] M. Nagahara, S. Miyoshi, H. Yaguchi, K. Onabe, Y. Shiraki, and R. Ito *Japan. J. Appl. Phys.*, vol. 33, p. 694, 1993.

[2] Y. Kato, S. Kitamura, K. Hiramatsu, and N. Sawaki *J. Crystal Growth*, vol. 144, p. 133, 1994.

[3] R. D. Underwood, D. Kapolnek, B. P. Keller, S. Keller, S. P. DenBaars, and U. K. Mishra *Solid State Electron.*, vol. 41, p. 243, 1997.

[4] T. Tanaka, K. Uchida, A. Watanabe, and S. Minagawa *Appl. Phys. Lett.*, vol. 68, p. 976, 1996.

[5] T. Akasaka, Y. Kobayashi, S. Ando, and N. Kobayashi *Appl. Phys. Lett.*, vol. 71, p. 2196, 1997.

[6] T. S. Zheleva, O. H. Nam, M. D. Bremser, and R. F. Davis *Appl. Phys. Lett.*, vol. 71, p. 2472, 1997.

[7] A. Usui, H. Sunakawa, A. Sakai, and A. Yamaguchi *Japan. J. Appl. Phys.*, vol. 36, p. L899, 1997.

[8] T. S. Zheleva, S. A. Smith, D. B. Thomson, T. Gehrke, K. J. Linthicum, P. Rajagopal, E. Carlson, W. M. Ashmawi, and R. F. Davis *Mater. Res. Soc. Symp. Proc.*, vol. 537, p. G3.38, 1999.

[9] K. Hiramatsu, K. Nishiyama, A. Motogaito, H. Miyake, Y. Iyechika, and T. Maeda *Phys. Stat. Sol. A*, vol. 176, p. 535, 1999.

[10] T. Asano, K. Yanashima, T. Asatsuma, T. Hino, T. Yamaguchi, S. Tomiya, K. Funato, T. Kobayashi, and M. Ikeda *Phys. Stat. Sol. A*, vol. 176, p. 23, 1969.

[11] M. Yang, M. Cho, C. Kim, J. Yi, J. Jeon, S. Khym, M. Kim, Y. Choi, S. J. Leem, and Y. H. Lee *J. Crystal Growth*, vol. 226, p. 73, 2001.

[12] N. Maeda, T. Saitoh, K. Tusubaki, and N. Kobayashi *Phys. Stat. Sol. A*, vol. 188, p. 223, 2001.

[13] T. Kato, Y. Honda, Y. Kawaguchi, M. Yamagushi, and N. Sawaki *Jpn. J. Appl. Phys.*, vol. 40, p. 1896, 2001.

[14] K. Hiramatsu *J. of Phys.: Condensed Matter*, vol. 13, p. 6961, 2001.

[15] P. Fini, *Threading Dislocation Reduction in Gallium Nitride Thin Films on Sapphire via Lateral Epitaxial Overgrowth*. Ph.d. dissertation, University of California, Santa Barbara, 2000.

[16] R. T. Huang, C. L. Jiang, A. Appelbaum, D. Renner, and S. W. Zehr *J. Electron. Mater.*, vol. 19, p. 1313, 1990.

[17] K. Nakai, T. Sanada, and S. Yamakoshi *J. Crystal Growth*, vol. 93, p. 248, 1988.

[18] K. Goto, M. Takemi, T. Miura, A. Takemoto, and Y. Mihashi *J. Electron. Mater.*, vol. 25, p. 411, 1996.

[19] C. H. Chen, S. Keller, G. Parish, R. Vetury, P. Kozodoy, E. L. Hu, S. P. DenBaars, and U. K. Mishra *Appl. Phys. Lett.*, vol. 73, p. 3147, 1998.

[20] H. Kawai, M. Hara, F. Nakamura, and S. Imanaga *Electron. Lett.*, vol. 34, p. 592, 1998.

[21] Y.-F. Wu, D. Kapolnek, P. Kozodoy, B. Thibeault, S. Keller, B. Keller, S. Denbaars, and U. Mishra in *IEEE Twenty-Fourth International Symposium on Compound Semiconductors*, (San Diego, CA, USA), p. 431, IEEE, 1998.

[22] K. C. Zeng, J. Y. Lin, H. X. Jiang, and W. Yang *Appl. Phys. Lett.*, vol. 74, p. 1227, 1999.

[23] J. A. Freitas Jr., O. H. Nam, R. F. Davis, G. V. Saparin, and S. K. Obyden *Appl. Phys. Lett.*, vol. 72, p. 2990, 1998.

[24] X. Li, A. M. Jones, S. D. Roh, D. A. Turnbull, S. G. Bishop, and J. J. Coleman *J. Electron. Mater.*, vol. 26, p. 306, 1997.

[25] S. D. Hersee, E. Barbier, and R. Blondeau *J. Crystal Growth*, vol. 77, p. 310, 1986.

[26] P. Demeester, P. Van Daele, and R. Baets *J. Appl. Phys.*, vol. 63, p. 2284, 1988.

[27] J. Christen, M. Grundmann, and D. Bimberg *J. Vac. Sci. Technol. B*, vol. 9, p. 2358, 1991.

[28] D. Buttari, R. Coffie, L. Shen, S. Heikman, S. Keller, and U. K. Mishra *submitted to IEEE Electron Device Letters*, 2002.

[29] S. Nakamura, T. Mukai, and M. Senoh *Japan. J. Appl. Phys.*, vol. 31, p. 2883, 1992.

[30] R. Y. Korotkov and B. W. Wessels *MRS Internet J. Nitride Semicond. Res.*, vol. 5S1, p. W3.80, 2000.

[31] R. Bhat, C. Caneau, C. E. Zah, M. A. Koza, W. A. Bonner, D. M. Hwang, S. A. Schwarz, S. G. Menocal, and F. G. Favire *J. Crystal Growth*, vol. 107, p. 772, 1991.

[32] C. Caneau, R. Bhat, and M. A. Koza *J. Crystal Growth*, vol. 118, p. 467, 1992.

[33] F. Bertram, T. Riemann, J. Christen, A. Kaschner, A. Hoffmann, C. Thomsen, K. Hiramatsu, T. Shibata, and N. Sawaki *Appl. Phys. Lett.*, vol. 74, p. 359, 1999.

[34] K. Hiramatsu, H. Matsushima, T. Shibata, Y. Kawagachi, and N. Sawaki *Mater. Sci. & Eng. B*, vol. 59, p. 104, 1999.

[35] T. Sanada, K. Nakai, K. Wakao, M. Kuno, and S. Yamakoshi *Appl. Phys. Lett.*, vol. 51, p. 1054, 1987.

5
Device Applications

A central part of this work was to explore selective area growth as a tool in device design. The development of the growth techniques was covered in the previous two chapters, and in this chapter they are put to use in actual device applications. In the applications, the selective area growth is introduced to solve known problems of AlGaN/GaN HEMTs, to varying degrees of success. One application, the low-profile contact regrowth (§5.4), I believe has potential for use in the standard fabrication process, with some further optimization. Another application, the drain regrowth for dispersion control (§5.5), more serves to illustrate a device problem, and to aid in understanding the physics of the problem. The most advanced application, the hot electron device with regrown source, has some potential, but at the current technology level other parasitic elements overshadow the possible benefits.

First, some of the issues of today's AlGaN/GaN HEMT devices will be discussed, including DC and RF features such as the soft current saturation, the g_m compression, and the low f_T. It will be argued that contact resistance and access resistance, particularly on the source side, is largely responsible for the non-ideal

device characteristics. Then, the application of various selective area growth techniques to ohmic contact formation, will be presented, followed by a few other device designs involving SAG.

I had help with many aspects of this device work. Robert Coffie did the processing and testing of the drain regrowth device (§5.5), and he also performed the power measurements of the trench-regrowth contacts (§5.2.4). Vamsi Paidi performed the e-beam lithography and gate deposition for the hot electron device in §5.7. Alessandro Chini developed a SiN passivation process, which he performed on the hot electron device, and Likun Shen helped out with s-parameter measurements. Brendan Moran grew the HEMT structure on SiC substrate that was used for the power measurements of the trench-regrowth contacts.

5.1 Device Issues and Proposed Solutions

This section will discuss some of the shortcomings of today's AlGaN/GaN HEMTs, and how they may be avoided. Since this dissertation is focused on epitaxial growth, the proposed solutions will naturally involve selective area growth.

5.1.1 DC Characteristics

Fig. 5.1 shows the I-V characteristics of a standard AlGaN/GaN HEMT on sapphire substrate. It has powerful features, such as high I_{max}, high breakdown voltage, and low output conductance, far superior to devices based on the GaAs or InP

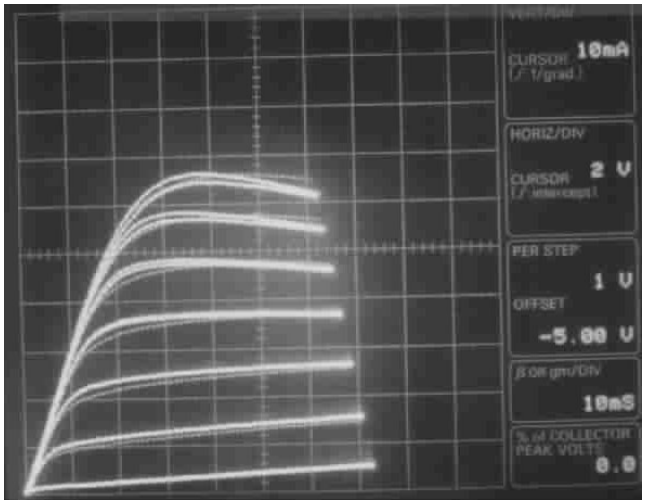

Figure 5.1: I_{ds} *vs.* V_d characteristic of a standard AlGaN/GaN HEMT on sapphire substrate, with 75 μm gate periphery. The gate sweep is from +1 V to -6 V in steps of 1 V.

systems. The AlGaN/GaN devices also show undesirable properties, including a high saturation voltage ('knee voltage'), soft current saturation, and strong g_m compression at high currents. In the following discussion, it will be argued that these undesirable properties are due to parasitic source and drain resistances.

Current Saturation

The current in an ideal FET can be described either by the gradual channel approximation, or by the saturated-velocity model, depending on gate length, and material properties.[1] For the short gate lengths used in microwave devices, HEMTs based on the GaAs or InP systems usually exhibit saturation-velocity limited cur-

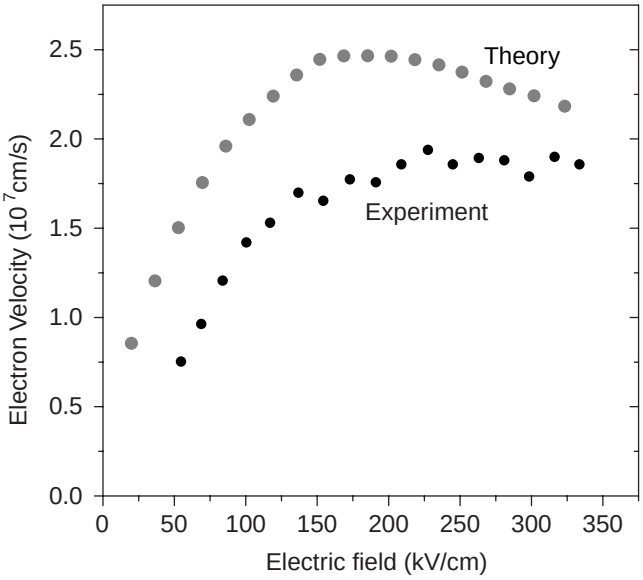

Figure 5.2: Velocity-field curves for wurtzite GaN. Theoretical values from ref. [3], and experimental values from ref. [4].

---

rents, if properly designed. The current is then:

$$I_{ds} = q \cdot n_s v_{sat} \tag{5.1.1}$$

where v_{sat} is the electron saturated velocity, and n_s is the charge under the gate, controlled by the gate bias. Experimentally and theoretically obtained velocity-field curves for GaN are plotted in Fig. 5.2, showing a saturated velocity of approximately 2×10^7 cm/s, which is comparable to GaAs. For AlGaN/GaN HEMTs with gate length L_g of $\sim$ 0.7 μm, Eqn.5.1.1 typically overestimates the current by a factor $\sim$ 3. For a shorter gate length of 0.15 μm, the overestimate can be less, down to $\sim$ 2.[2] This suggests that the electrical field under the gate is lower than the critical field ($\sim$ 150 kV/cm) required to reach saturation. To understand the current

limiting mechanism in detail, a full 2-D solution to Poisson's equation, is necessary, utilizing realistic transport models. However, by considering typical device characteristics, particularly in the high current region, some conclusions can be reached. The strong g_m compression at high currents is not characteristic of a long gate device, described by the gradual channel approximation, but rather indicates a different saturation mechanism.

The source resistance R_s, consisting of the contact resistance and the resistance of the access region, decreases the measured extrinsic g_m relative to the intrinsic value, as follows:

$$g_{m,extrinsic} = \frac{g_m}{1 + g_m \cdot R_s} \tag{5.1.2}$$

The decrease in g_m is independent of the current level, for a constant R_s. However, for high current levels, R_s need not be constant. For the standard AlGaN/GaN device structure of today, the charge in the access regions is the same as under the gate, for an open channel. Since the current is the same in all regions, this implies that the drift velocity is also the same. Under the gate, and in the gate-drain region, high fields can be generated by a high drain bias, which allows the electrons to reach velocity saturation. In the source-gate region however, the high fields from the drain are screened by the gate, preventing the electrons from reaching the saturated velocity. The source access-region therefore effectively limits the current flow through the device. Several ways to eliminate the problem will be discussed below. It is also possible that the fields under the gate, on the source-side, are too low, serving to

limit the current and the electron velocity as well. This will be discussed in §5.1.2.

Close Gate-Source Alignment

The most straight-forward way of eliminating the current saturation in the source access region is to remove the region altogether, by placing the gate right next to the source contact. This is technologically challenging, since the metal of the source contact tends to have a rough edge, and the hight of the source contact makes gate lithography difficult. Furthermore, the contact itself may also cause saturation, since some current flows in the material under the contact metal, within a transfer length, before entering the metal.

A device with very close source-gate spacing was demonstrated by Ching-Hui Chen, using a self-aligned gate and n^+-GaN regrown source and drain contacts.[5] Despite a relatively long gate of 1.2 μm, and a low channel charge of 7.5×10^{12} cm^{-2}, a current density in excess of 1 A/mm was achieved. The device had low knee voltage, showed a high g_m, and most importantly did not exhibit the typical g_m compression at high currents. However, the self-aligned process suffered from low yield, and the devices had low breakdown voltage, limiting their usefulness. Despite these problems, the experiment served well to demonstrate the benefits of eliminating the source access region.

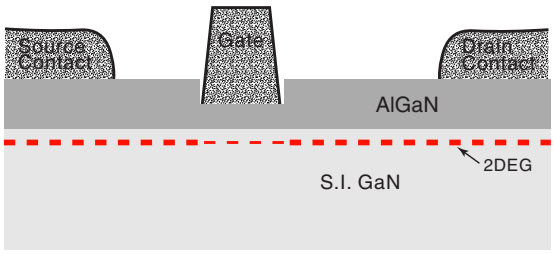

Figure 5.3: Gate recess structure, to eliminate current saturation in the source access region.

Gate Recess

Another solution to the saturation problem is to ensure that the source access region has higher conductivity than the gate region. This can be done in one of two ways: processing of the planar structure, or by selective area growth. The processing approach is used extensively in GaAs and InP based devices, and typically involves one or more recesses at or around the gate, as illustrated for the AlGaN/GaN HEMT in Fig. 5.3. The gate recess lowers the charge in the gate region, compared to the access regions, by removing a highly doped top layer, or by modifying the charge balance according to the lever rule. The importance of the gate recess technology was first realized in the late 1970's and the early 1980's, for GaAs microwave power MESFETs.[6] The sought benefits were higher breakdown, and improved noise performance, but other related improvements were also observed, such as lowered saturation voltage, and increased transconductance.[7] Recessing is easy in conventional III-V device technologies, since well developed wet etchants

are available, and is used for virtually all HEMT devices. For the nitride semiconductors few wet-etching techniques exist, and none are suitable for gate recessing. The other alternative, dry etching, often suffers from plasma damage, that degrades the transport properties in the active region of the device.

Despite the challenges, some AlGaN/GaN HEMT devices with gate recess have been demonstrated. In recent work by Dario Buttari, utilizing a low damage digital etch technique, a 100 Å gate recess was realized on a 290 Å AlGaN barrier.[8] The device showed reduced pinch-off voltage, and increased g_m. Similar I_{max} to non-recessed devices was achieved, but at these current levels there was no improvement of the g_m compression or the soft saturation. No improvement was expected, since the source access region had the same amount of charge as in non-recessed devices. For improved characteristics at high currents, the layer structure of the source access region must have higher conductivity than the standard HEMT structure. Structures could include n^+-GaN or n^+-AlGaN cap layers, or a high Al-composition barrier, that could be (partially) removed in the gate region.

Regrown Source and Source Access Region

Instead of increasing the charge with the gate recess approach, charge can be added beneath the channel, as illustrated in Fig. 5.4. This would ideally be accomplished by a selective ion implantation of an n-type dopant, through the AlGaN barrier, into the source access region. At present date, ion implantation into GaN is

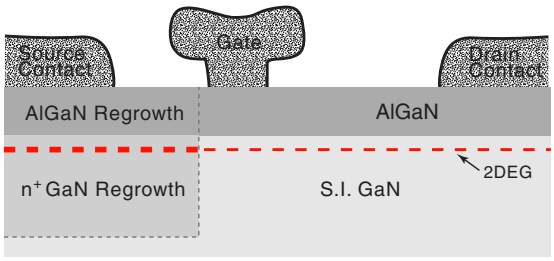

Figure 5.4: Improved device structures to eliminate current saturation in the source access region. Can be implemented with an etch followed by AlGaN/n^+-GaN non-planar selective area growth.

---

associated with serious problems, and can not be used in the present application. A more viable approach is to utilize selective area growth. By etching the source and the source access region, and regrowing n^+-GaN in the etched region, followed by an optional AlGaN cap layer, a structure similar to Fig. 5.4 can be achieved.

Of great importance for the success of the SAG approach is the physical profile of the growth. As the gate needs to be positioned very close to the regrowth edge, it is unacceptable if the regrowth extends high above the original sample surface, or even worse if lateral overgrowth onto the mask occurs. A high step at the regrowth edge may interfere with the gate lithography, in particular for very short gate lengths. For T-shaped e-beam gates, where the foot-print of the gate is much shorter than the top of the gate, a low profile regrowth edge would allow very close alignment, with the top part of the gate extending over the regrowth area, as illustrated in Fig. 5.4. A suitable regrowth technique was discussed in §4.7, capable of growing n^+-GaN with a 20 nm $Al_{0.35}Ga_{0.65}N$ cap layer, extending up to 10 μm laterally from the mesa

edge, while only causing a 30 nm step at the regrowth edge. The application of this technique to ohmic contact regrowth will be presented in §5.4.

5.1.2 High Frequency Operation

There are two frequencies of merit for high frequency operation of transistors. The unity gain frequency cutoff (f_T) is a measure of the inherent electron transit time in the device, and is commonly used as a benchmark to compare high frequency performance of devices. The maximum frequency of oscillation (f_{max}) is the power gain cutoff frequency. f_{max} is a function of f_T, but is also influenced by quantities such as gate resistance and gate-drain capacitance. f_{max} can usually be optimized by proper device design, while f_T is ideally limited by material properties and gate length.

Fig. 5.5 shows values of f_T *vs.* gate length L_g, obtained from literature, for AlGaN/GaN HEMTs fabricated by various groups, compared to HEMTs based on the GaAs and InP material systems. The inverse dependence of f_T on L_g for the different material systems is visible in the log-log scale, as the data forms approximately straight lines with slope -1. The inverse relation overestimates the obtained f_T for very short gate lengths, when parasitic quantities start dominating over the electron transit time. The intrinsic expression for f_T is:

$$2\pi \cdot f_T = \frac{g_m}{C_{gs} + C_{gd}} \approx \frac{v_s}{L_g} \tag{5.1.3}$$

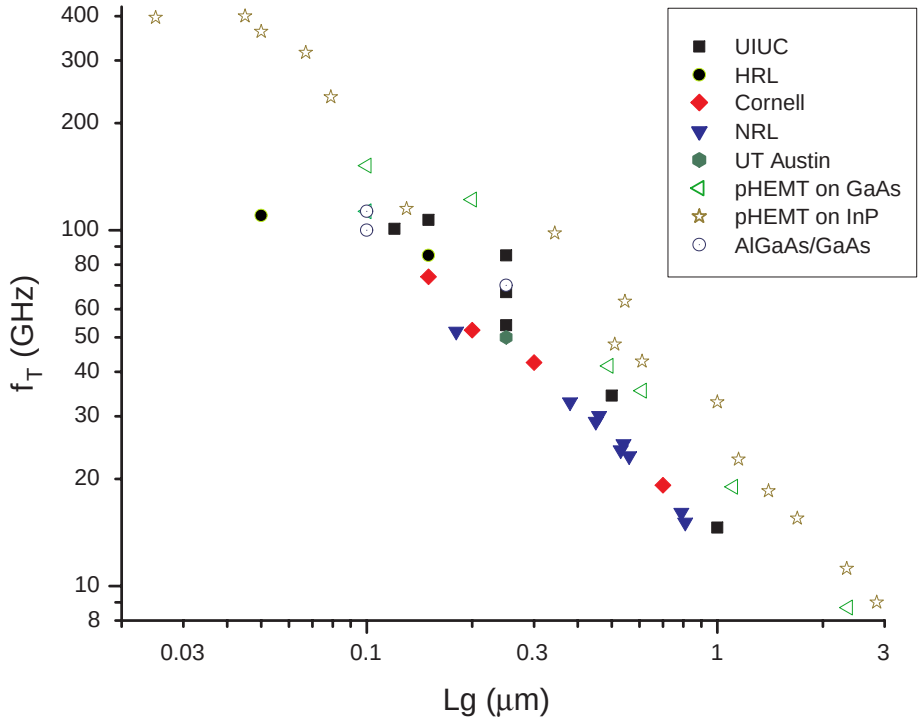

Figure 5.5: Unity current gain (f_T) *vs.* gate length L_g for AlGaN/GaN HEMTs fabricated at various laboratories (filled symbols), and for HEMTs fabricated in other material systems (open symbols). From references: [9, 10, 11, 12, 13] - UIUC (University of Illinois, Urbana Champaign), [14, 2] - HRL (HRL Laboratories LLC), [15] - NRL (Naval Research Laboratory), [16] - Cornell University, [17] - UT Austin (University of Texas, Austin), [18, 19, 20, 21, 22] - p-HEMT on InP, [23, 24, 21, 22] - p-HEMT on GaAs, and [25, 26, 27] - AlGaAs/GaAs.

---

where the second approximate term is obtained using the saturation FET model. v_s is the electron saturation velocity, and the term v_s/L_g is the inverse of the transit time, assuming a constant velocity of v_s. The source and drain resistance of the device have a second-order effect on f_T, given by the following expression:[28]

$$2\pi \cdot f_T = \frac{g_m}{[C_{gs} + C_{gd}] \cdot [1 + (R_s + R_d)/r_0] + C_{gd} \cdot g_m \cdot (R_s + R_d)} \tag{5.1.4}$$

The source and drain resistance, R_s and R_d, which include the contact resistance

and the access regions, can degrade the extrinsic f_T if too large. When reducing the gate length in a given device design, with all other dimensions fixed, a saturation in f_T will eventually occur, beyond which further gate scaling has little effect on f_T. For pseudomorphic InAlAs-InGaAs HEMTs, device designs exist for which f_T increases with reduced L_g down to 45 nm, with f_T up to 400 GHz.[20] For current AlGaN/GaN devices, no improvement in f_T seems to occur beyond 0.15 μm gate lengths, due to the relative immaturity of the device designs. As was discussed at length in §5.1.1, GaAs and InP based state-of-the-art power devices employ some kind of gate recess, while today's AlGaN/GaN HEMTs typically are planar. To reach far beyond the 100 GHz level by further gate scaling, it will be necessary to employ an effective gate recess technique, or to use the regrowth solution proposed in §5.1.1.

In the absence of parasitic resistances, the relation $2\pi \cdot f_T = v/L_{g,eff}$ can be used to estimate the electron drift velocity v under the gate. For p-HEMTs on GaAs and InP substrates, the estimated drift velocity is typically around 2-3$\times 10^7$ cm/s, which is higher than the saturation velocities in these materials. Apparent from the generally lower values of f_T for nitride devices in Fig. 5.5, the estimated electron drift velocity is lower, about 1×10^7 cm/s, which is only half of the saturated velocity in GaN (see Fig. 5.2). The parasitic resistances are part of the problem, but another problem may lie in the very high electric fields required to reach velocity saturation. As can be seen in Fig. 5.2, an electric field of $\sim$ 150 kV/cm is required

to reach velocity saturation in GaN, while only 3 - 4 kV/cm is necessary for velocity saturation in GaAs. To calculate the exact electric fields under the gate in the device, a full 2D solution of Poisson's equation is required, using the appropriate velocity-field curves. In the absence of that, as a simple estimate it can be assumed that the electric field scales with the saturation drain voltage. A typical GaAs based HEMT saturates at a V_d of 1 V, while AlGaN/GaN HEMTs saturate at $\sim$ 5 V. The electric field in the AlGaN/GaN HEMT would therefore be about 5 times that of the GaAs HEMT, but the field required for electron velocity saturation is nearly 50 times higher for GaN than for GaAs. This rough estimate indicates that the fields in the AlGaN/GaN device are too low to accelerate the electrons to saturation.

To achieve a higher electron velocity under the gate, the introduction of an electron quasi-field at the source-end of the gate is proposed. The quasi-field is generated by a band-gap discontinuity, caused by the placement of a higher bandgap material near the gate. The structure, involving the selective area growth of $Al_{0.05}Ga_{0.95}N$, is illustrated in Fig. 5.6. The gate is made very short, by e-beam lithography, and it is aligned very close to the regrowth edge. As the electrons enter the channel under the gate, from the $Al_{0.05}Ga_{0.95}N$, the electrons gain kinetic energy equal to the conduction band discontinuity, which for a 5% Al composition is about 0.1 eV. The kinetic energy of 0.1 eV corresponds to a velocity of $\sim 3\times10^7$ cm/s, which is close to the electron saturated velocity.

After the gain in kinetic energy, the electrons are 'hot', since their distribution

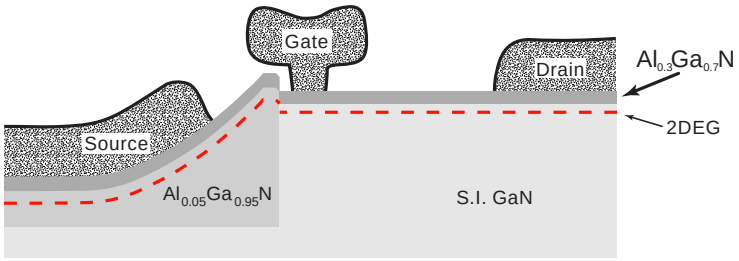

Figure 5.6: Device structure with $Al_{0.05}Ga_{0.95}N$ source regrowth, to create electron quasi-field at source-side of gate for higher electron velocities under the gate.

---

is no longer the equilibrium distribution, dictated by the lattice temperature. Within a short distance, the electrons return to their equilibrium distribution by scattering events, if the electric field is low. The distance within which this happens, the relaxation distance, is currently not known. Some indications as to the magnitude can be obtained from measurements of the transient electron velocity overshoot, performed by Wraback *et al.*.[29] Starting with an equilibrium distribution, electron velocity overshoot up to over 7×10^7 cm/s was observed for strong applied fields (300 kV/cm), lasting for a distance of ~ 0.3 μm. The circumstances of the measurement were different than for the structure proposed here, but it shows that electrons in GaN have the capability of remaining hot for substantial distances.

To take advantage of the high velocity of the hot electrons generated at the regrowth interface, the gate must be placed, and fit within, the 'relaxation distance' of the regrowth edge. If the relaxation distance is 0.3 μm as suggested above, this can be accomplished with e-beam lithography.

In addition to allowing electrons to reach saturation velocity, it is possible that the $Al_{0.05}Ga_{0.95}N$ source could cause velocity overshoot for electrons under the gate. In the measurements by Wraback *et al.*,[29] velocities of over 7×10^7 cm/s were reached, which is more than 3 times the saturated velocity. If such velocities can be accessed during device operation, enormous improvements in f_T would follow. Signs of velocity overshoot have been seen by some researchers for AlGaAs/GaAs HEMTs.[26, 30]

5.1.3 Summary of Proposed Solutions

The most important suggestion for improving the device characteristics, is the reduction of parasitic resistances. By minimizing the source and drain resistances, such problems as the soft current saturation, high knee voltage, g_m compression, and low f_T, can be addressed. Furthermore, microwave power gain compression, which probably is related to the g_m compression, can be improved, and along with that also the linearity.

In addition to reducing the source and drain resistances, a structure consisting of $Al_{0.05}Ga_{0.95}N$ source regrowth was suggested. The structure would provide for higher electron drift velocities under the gate, and therefore a higher f_T.

5.2 Ohmic Contacts by Mass-Transport Growth

So far in this chapter, the benefits of reducing the contact resistance, and the access resistance, have been emphasized, and regrown ohmic contacts have been proposed to accomplish this. Regrown ohmic contacts also have the benefit of contacting the active layer of a device, independent of the layer-structure of the device. By etching into the device structure, and regrowing n^+-GaN, the current can flow from the regrown material into the device channel through the vertical regrowth interface, regardless of the depth of the channel, or the vertical resistance to current flow in the device active layers. Regrown ohmic contact also have merits when ohmic contacts to low conductivity material is needed. Regular annealed metal contacts to GaN rely on a relatively high impurity concentration, to show ohmic behavior, while n^+-GaN regrown contacts do not have this requirement. An example of such use is the conductivity measurements near the mesa edge, in §4.6, where n^+-GaN regrowth enabled ohmic contact formation to very lightly doped material.

Structures with high Al-composition in the AlGaN barrier can be difficult to form low resistance contacts to. The aluminum composition in the AlGaN barrier of typical AlGaN/GaN HEMTs is in the range 30 - 40 %, but in some cases a higher composition is desired. By increasing the Al composition, the barrier can be made thinner, while still retaining high charge in the channel, which can be important for increased g_m and to avoid short channel effects for short gate length devices. Tra-

ditionally, high Al-compositions were associated with growth difficulties, and low 2DEG mobilities would result from increased alloy scattering. However, the recent introduction of an AlN interlayer at the AlGaN-GaN hetero-interface,[31, 32] has eliminated the adverse effects of alloy scattering, enabling higher Al-compositions to be used in device structures. When devices utilizing high Al-composition AlGaN start emerging, the need for efficient contact regrowth schemes will increase.

Using non-planar (and planar) SAG of Si-doped GaN, several demonstrations of regrown ohmic contacts can be found in the literature.[5, 33, 34, 35] Regrowth is appealing from a design standpoint, but the additional step in the growth system is unacceptable in many production settings. In Chapter 3, a selective area mass-transport growth technique was demonstrated, where mass-transport from large unmasked areas caused GaN deposition to occur at the etched mesa edges. The process, a short $\sim 1090^{\circ}$C anneal in an ambient of ammonia and hydrogen, does not require an MOCVD growth system, but can in principle can be performed in an ammonia-annealing furnace. Mass-transport effects have in fact been demonstrated in an HVPE system,[36] which shows that the process is reactor independent. Using the mass-transport growth technique, ohmic contact regrowth can be performed by research groups that do not have access to an MOCVD system.

To form good contacts, the regrown material must be n+ doped, normally achieved by flowing disilane during growth. For the mass-transport growth, the SiO_2 mask serves as a source for n-type dopants, by slowly dissociating into Si and oxygen, in

the aggressive annealing environment. In §3.7, a high doping level of 2.1×10^{19} cm^{-3} (1.6×10^{19} cm^{-3} Si and 5×10^{18} cm^{-3} oxygen) was measured in GaN grown by mass-transport, without any external supply of dopants. The strong auto-doping eliminates the need for an external dopant, another important feature of the mass-transport growth that makes it promising as a cheap and simple regrowth technique.

5.2.1 Experiment

The contact regrowth experiments were performed on $Al_{0.3}Ga_{0.7}N$/GaN heterostructures prepared by MOCVD on semi-insulating GaN wafers. The films underwent the standard processing for non-planar regrowth, described in §3.2. The process consisted of deposition and patterning of an SiO_2 mask, followed by a 400 nm reactive ion etch into the device structure.

After preparation, mass-transport growth was performed on the samples, using the standard conditions detailed in §3.3. The standard anneal consisted of heating to 1090°C for 3 minutes, in a gas mixture of 8 slpm NH_3 and 4 slpm H_2 at 100 Torr. The SiO_2 mask served the dual purpose of protecting the unexposed area, and acting as a solid dopant source during the anneal. The SiO_2 mask was removed after the anneal by a 6 minute etch in buffered HF. Ohmic contact pads were formed in a TLM configuration, by a short reactive ion etch of the contact area, followed by e-beam evaporation of Ti/Al/Ni/Au (20nm/200nm/55nm/45nm). The contact metal was annealed at 860C in N_2 for 30 seconds, and in the final step an isolation region around

the TLM pattern was defined by reactive ion etching through the $Al_{0.35}Ga_{0.65}N$.

From the TLM measurements the *transfer* contact resistance, with the unit Ωmm, was obtained. This is the relevant measure of contact resistance for the lateral HEMT devices. The specific contact resistance (Ωcm^2) is difficult to determine from regular TLM measurements, since the regrown material under the contacts has a different sheet resistance than the material between the contacts. Even if the sheet resistance of the regrown material is determined by other TLM measurements, the properties near the regrowth edge are typically non-uniform (see §4.6), which leads to a variable specific contact resistance that can not be determined.

5.2.2 Single Edge Regrowth

In the first experiment, the contact pads were placed in areas that were unmasked during the anneal, overlapping onto the mass-transport growth at the mesa edge. Fig. 5.7a shows a section of a TLM pattern, after metal deposition, where the edge of the contact metal is located about 1 μm from the mesa edge. Each contact pad overlaps onto the growth along *one* mesa edge; accordingly the contact structure will be referred to as 'single edge contact'. A cross-section of the contact structure is illustrated in Fig. 5.7b, where the 'contact alignment', an important parameter for the contact, is indicated. The mask layout contained several TLM patterns, with 0, 0.3, 0.7, and 1.0 μm contact alignments.

Contact resistance was measured with the TLM method, both for regrown con-

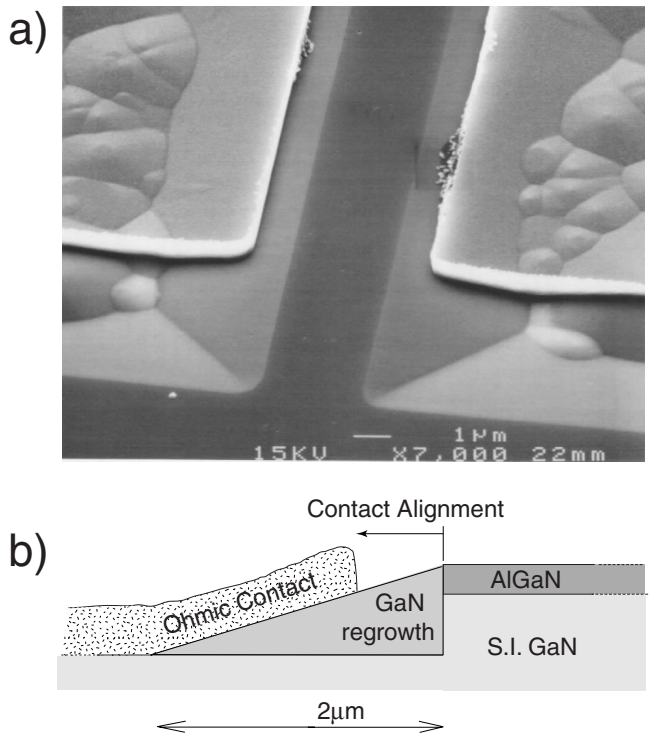

Figure 5.7: Ohmic contact structure utilizing the mass-transport growth along the edge of a mesa. a) SEM image of two contact structures facing each other, spaced 3 μm apart. b) Schematic of the cross-section of a finished regrown contact structure. The 'contact alignment' was a variable in the experiments.

---

tacts and for conventional contacts formed directly to the AlGaN/GaN heterostructure. For the conventional contacts a contact resistance of 0.35 Ωmm was obtained, which is on the low side of what is typically obtained ($\sim$ 0.5 Ωmm) with the metallization scheme used, for 30% Al composition.[37] The contact resistance of the regrown contacts is plotted in Fig. 5.8, as a function of the contact alignment. The contact resistance ranged from 0.40 Ωmm for zero contact alignment, to 1.26 Ωmm for 1 μm alignment. The rapid increase in contact resistance with increased contact

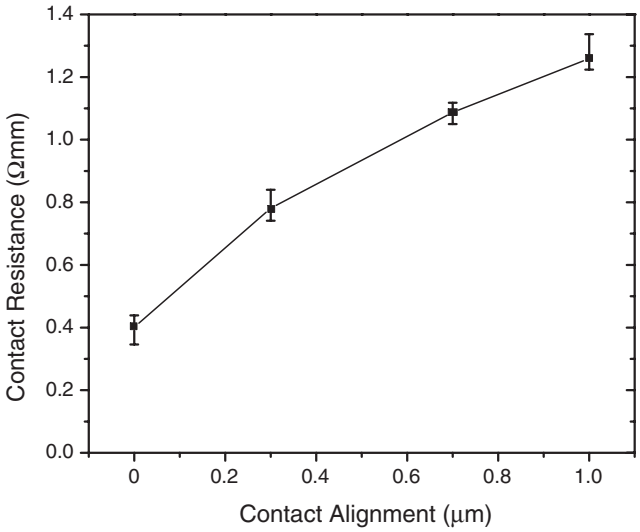

Figure 5.8: Contact resistance of the 'single edge' contacts, as a function of the contact alignment.

---

alignment was surprising at first. Recalling the resistivity measurements performed on the mass-transport grown material, in §3.7, it is clear that the access resistance introduced for a non-zero contact alignment can not cause such a rapid increase. The measurements showed a very low average resistivity of 4×10^{-3} Ωcm, which would result in an access resistance of 0.03 Ωmm for a 0.3 μm access region. This value is much lower than the 0.38 Ωmm increase in contact resistance observed when increasing the contact alignment from 0 to 0.3 μm. Furthermore, the rapid increase in contact resistance can not be attributed to the reduced contact area either. This becomes clear when considering that the contact resistance was nearly doubled when going from zero to 0.3 μm contact alignment, at the same time as the contact area was reduced by only 15%.

The rapid increase in contact resistance can be explained by a non-uniform doping-profile of the mass-transport growth. The impurity incorporation originates from the SiO_2 mask, and it seems reasonable that material grown close to the mask would incorporate more dopants. Furthermore, based on observations made in §4.6, non-planar growth may cause non-uniform doping, due to orientation dependent dopant incorporation. The contact structure presented in the following section takes advantage of the high doping near the mask, and shows reduced contact resistance as a result.

The single edge contact structure shows that mass-transport growth is useful for ohmic contact formation. The simplicity of the technique, and the potential of performing it without an expensive MOCVD system, makes it attractive. However, for the purpose of reducing the source access region resistance, at the same time as lowering the contact resistance, the present contact structure is not suitable. For the ~ 0.5 μm contact alignment required for close gate spacing, the total contact resistance increased to over 0.9 Ωmm, which is too high. For applications where a zero contact alignment is acceptable, the single-edge contact structure is attractive, since existing mask sets can be used. The SiO_2 regrowth mask can be defined with the same mask as the ohmic contact layer, with image reversal.

5.2.3 Trench Regrowth

In §3.6 it was shown that mass-transport growth can occur in etched trenches located up to $\sim$ 300 μm from a source supply (a large unmasked area). A different contact structure was developed, with the goal of further reducing the contact resistance, by utilizing mass-transport growth in narrow trenches. In this structure, the contact pads were placed to overlap with one side onto 2 μm mass-transport grown trenches, as shown in Fig. 5.9a. The contact alignment was kept constant in this experiment, at a value of 0.3 μm, as illustrated in Fig. 5.9b. Four samples were prepared, at different annealing temperatures, to study the effect of annealing temperature on the contact resistance. The temperatures used were 1070°C, 1080°C, 1090°C, and 1100°C. In the mask layout used for this experiment the trenches were on average located about 200 μm from the unmasked areas.

The morphology of the trench-growth for the four samples is shown in Fig. 5.10. The morphology of the regrowth changed with annealing temperature; at lower temperatures the slopes of the regrowth had small pits, which were replaced at higher temperatures with larger pits at the center of the v-shaped groove. Overall, the observed morphologies suggest source depletion, which is related to the large distance ($\sim$ 200 μm) to the source supply.

Contact resistance was measured with the TLM method, for regrown contacts as well as conventional contacts on the same samples. The conventional contacts

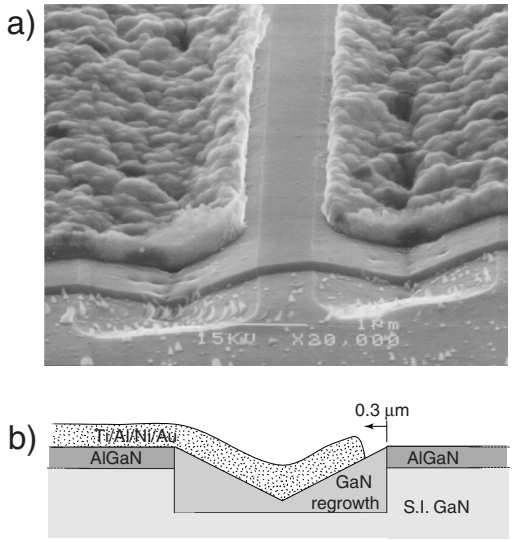

Figure 5.9: Ohmic contact structure utilizing mass-transport growth into a 2 μm etched trench. a) SEM image of two contact structures facing each other, spaced 0.7 μm apart. b) Schematic of the cross-section of the finished regrown contact structure. The 'contact alignment' was fixed at 0.3 μm.

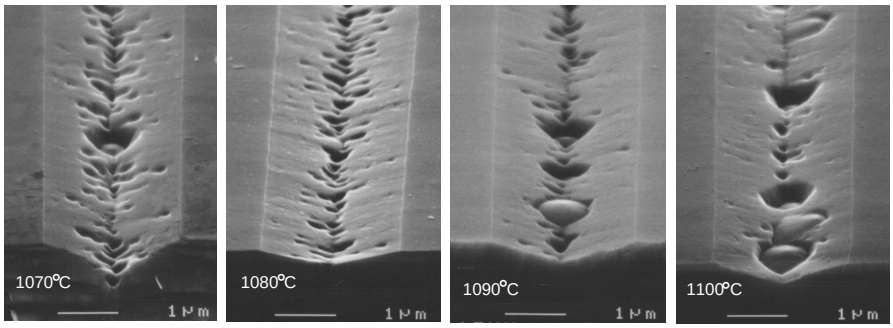

Figure 5.10: SEM images of mass transport regrowth in 2 μm trenches, for annealing temperatures between 1050°C and 1080°C.

had a contact resistance of 1.0 Ωmm, which is higher than usual, perhaps due to SiO_2 residues remaining on the sample surface after mask removal. The contact resistance measured for the regrown contacts is plotted in Fig. 5.11 as a function of

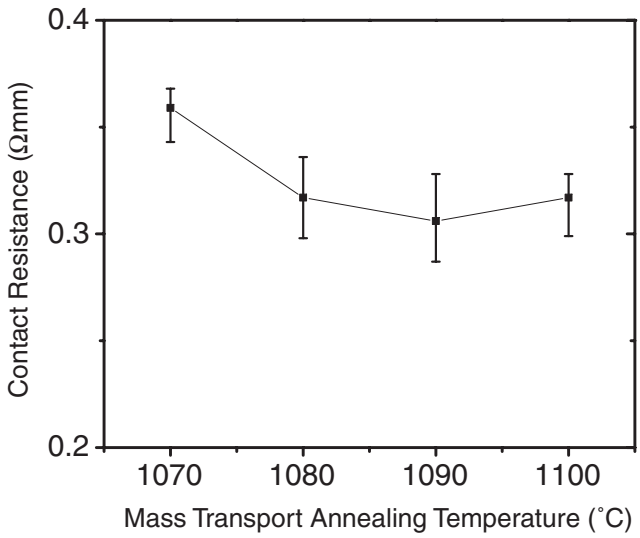

Figure 5.11: Contact resistance of trench regrowth contacts, as a function of annealing temperature.

---

annealing temperature. An average contact resistance of 0.31 Ωmm was achieved for the optimum annealing temperature of 1090°C, which is an improvement over the results obtained for the single-edge contact structure described in the previous section. The mild temperature dependence observed may be due in part to the change in growth morphology with temperature (see Fig. 5.10), and in part to a change in dopant incorporation with temperature.

The contact resistance of 0.31 Ωmm was obtained for a fix contact alignment of 0.3 μm. For the same alignment, the single edge contact in the previous section exhibited a contact resistance of 0.78 Ωmm. This shows that the trench regrowth has superior contact properties, probably due to the presence of SiO_2 mask on both sides of the regrowth, resulting in more autodoping. In the previous section it was sug-

gested that the regrown material was non-uniformly doped, with the highest impurity concentrations near the regrowth edge. In analogy with that, the trench regrowth should have two regions of high impurity concentration, at both edges of the trench. The superior performance of the trench-regrowth contacts therefore lends supports to the idea of non-uniform doping.

For the application of reduced access region resistance, the trench contact structure shows more promise than the single edge structure. The 0.3 μm contact spacing used in the experiment may be too short for reliable placement of a gate at the regrowth edge, but the contact resistance would probably not increase much for a spacing of 0.5 μm, which would allow reliable close gate spacing.

5.2.4 Device Performance

Measurement of contact resistance gives important information, but the ultimate validation of the contact structure lies in the device performance. When performing SAG on the HEMT structure, there is always the risk that damage occurs, due to the high temperature and duration of the growth. By fabricating devices, and verifying their functionality both at DC conditions and at high frequency, it is confirmed that no significant damage occurred. Furthermore, by making devices and testing them, the soundness of the starting material is verified. For example, if contacts are fabricated to a device structure with an n-type buffer, the contacts may have better performance than with a semi-insulating buffer, but such material is useless for

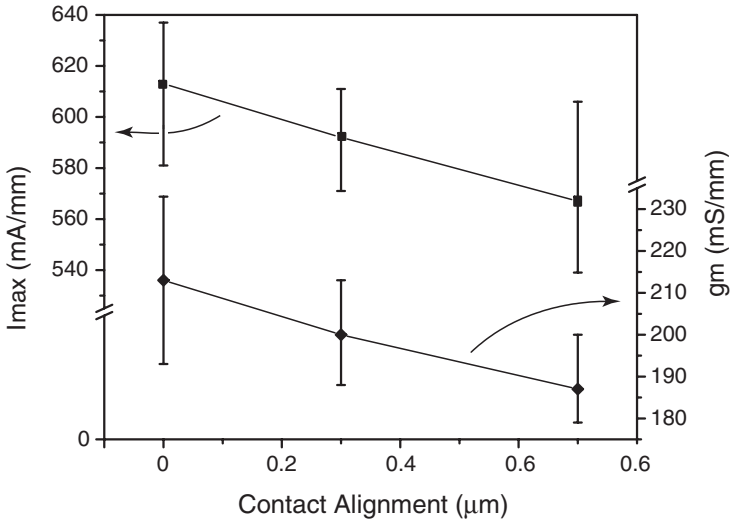

Figure 5.12: Maximum source-drain current and transconductance for devices with single edge regrowth contacts. The relatively low currents were attributed to a low sheet charge of the HEMT structure.

---

device applications, since current pinch-off can not be achieved.

Using the single edge regrowth discussed in §5.2.2, HEMT devices with regrown source and drain contacts were fabricated for DC testing. A 0.7 μm gate was deposited between the regrown source and drain, with a 0.7 μm gate to source spacing. The devices showed good pinch-off. Maximum drain current (I_{max}) and gate transconductance (g_m) were measured, as a function of contact alignment, as these parameters were expected to show dependence on source contact resistance. The results are plotted in Fig. 5.12, and although the data has significant spread, the expected trends are observed. The zero contact alignment (lowest contact resistance) gave the best performance, with I_{max} = 610 mA/mm and g_m = 210 mS/mm. The

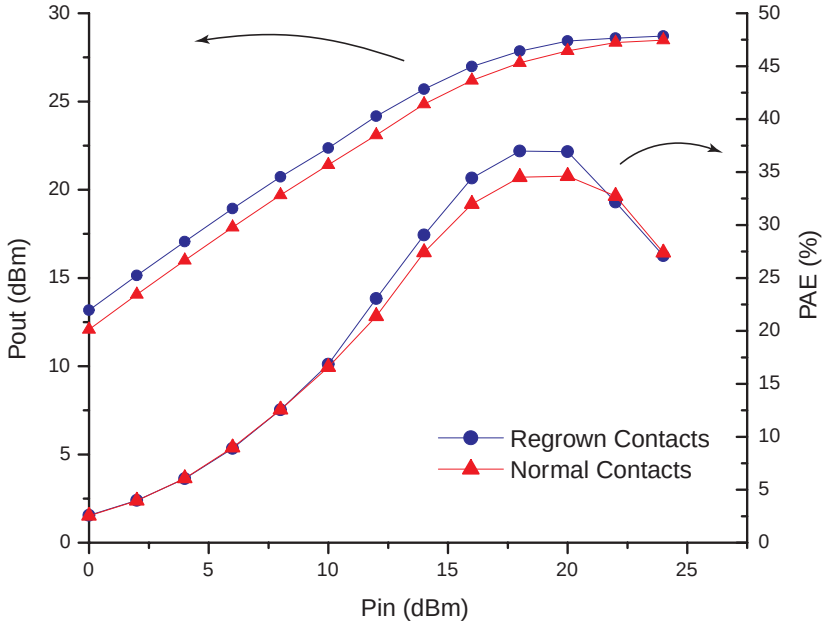

Figure 5.13: RF performance of device with source and drain regrown contacts (trench regrowth), compared to device with normal contacts, measured at 8 GHz. The bias conditions were: V_{ds} = 25 V, $I_{ds,regrowth}$ = 192 mA/mm, and $I_{ds,normal}$ = 153 mA/mm. For regrown contacts a maximum output power of 4.8 W/mm, and a maximum power added efficiency of 37%, was achieved. For normal contacts a maximum output power of 4.5 W/mm, and a maximum power added efficiency of 35% was achieved.

---

relatively low I_{max} obtained was not related to the contact regrowth process, but was due to a low sheet charge of the starting HEMT material.

HEMT devices were also fabricated for RF power measurements, using the trench regrowth contacts described in the previous section. The starting material was an $Al_{0.35}Ga_{0.65}N$/GaN HEMT grown on semi-insulating SiC substrate. The output power and the power added efficiency (PAE), as a function of input power, can be seen in Fig. 5.13, for both regular devices and devices with regrown contacts. For a source-drain bias of 25 V a maximum output power of 4.8 W/mm, and a max-

imum power added efficiency (PAE) of 37%, was achieved at 8 GHz, for the device with regrown contacts. The output power was limited by gate-drain breakdown, due to a relatively narrow gate-drain spacing of 0.7 μm. For the same bias conditions, devices with conventional source- and drain contacts showed similar performance, with a maximum output power of 4.5 W/mm, and a maximum PAE of 35%. The power performance was comparable for devices with both types of contacts, showing that the mass-transport growth did not measurably degrade the HEMT structure. The advantage of the technique will be most apparent in the next generation scaled devices with ultra-short gate lengths and gate-source spacings.

5.2.5 Summary of Ohmic Contacts by Mass-Transport Growth

Mass-transport growth was successfully used for n^+-GaN ohmic contact regrowth for AlGaN/GaN HEMTs. The growths were performed by annealing the samples in ammonia and hydrogen, without external supply of gallium. The autodoping from the SiO_2 mask was sufficient to supply high levels of n-type doping for the growth. The single edge contact is easy to make, since it can use the same lithographic mask plate as the ohmic contact layer. For good alignment of the contact to the metal edge, an average contact resistances of 0.4 Ωmm can be achieved. For improved performance, and when the contact metal needs to be stepped back from the regrowth edge, the trench growth can be used. With the metal edge aligned 0.3 μm from the regrowth edge, an average contact resistance of 0.3 Ωmm can be achieved.

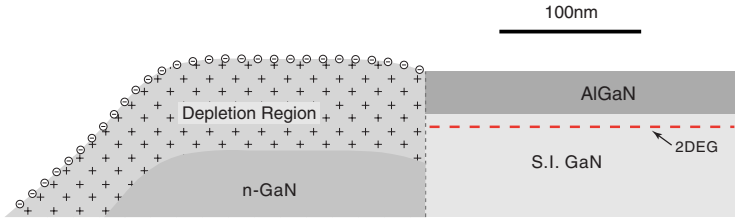

Figure 5.14: Surface depletion of a lightly n-type doped regrowth region. If depletion extends deeper than the 2DEG of the HEMT structure, the depletion can give rise to additional resistance for current flow from the regrowth region into the device channel.

Fabricated devices with both types of contacts showed normal device characteristics, when tested for DC and RF performance.

5.3 Surface Depletion of Regrowth

Surface depletion in the regrowth region can form a barrier for current flowing from the regrowth into the 2DEG of the HEMT structure. The scenario is illustrated schematically in Fig. 5.14 (to scale), showing the interface between a lightly n-type doped GaN regrowth and a HEMT structure. The c-plane of Ga-polar wurtzite GaN has been shown to exhibit pinning of the fermi-level at the surface, at approximately 1 eV below the conduction band.[38] The fermi-level pinning gives rise to a carrier depletion layer at the surface, with a depth depending on the doping density. For a doping density of 1×10^{18}, the depletion depth is 33 nm, and for a lower doping density of 1×10^{17}, the depletion depth is $\sim$ 100 nm. Once the depletion region extends deeper than the 2DEG in the HEMT structure, current flowing from the re-

grown region into the 2DEG has to pass through the depletion region, which gives rise to additional resistance. Surface depletion is not a problem for n^+-GaN regrowth for ohmic contact formation, but for lower doped regrowth it may pose a problem. A way around the problem is to deposit a thin $Al_{0.35}Ga_{0.65}N$ cap layer on top of the n-GaN regrowth. The large polarization field in the AlGaN screens the effect of the fermi-level pinning at the surface, for an $Al_{0.35}Ga_{0.65}N$ thickness of $\sim$ 4 nm or greater.[39]. For a thickness above 4 nm, a 2DEG is formed under the AlGaN, which may have the additional advantage of increasing the conductivity in the regrown region, as will be demonstrated in the following section. The formation of the 2DEG in the regrowth areas has not conclusively been shown, but the enhanced conductivity is a strong indicator.

5.4 Ohmic Contacts by Low-Profile Regrowth

In §5.2 an ohmic contact regrowth process was developed, with the aim at simplicity, and low cost. In this section a different type of process is developed, with the aim at high device performance, while simplicity and low cost was not a priority. The regrowth requires Ga and Al precursors, and can therefore not be performed in an annealing chamber, as the mass-transport growth can.

The most important figure of merit for an ohmic contact is of course the contact resistance, and for lateral devices it is best quantified by the *transfer* contact resis-

tance, measured in Ωmm. Another important factor can be the morphology of the contact after anneal, if the ohmic metal is to be used as alignment marks for e-beam lithography. Considering the use of the contact as the source terminal of a HEMT, another aspect becomes important. As was detailed in §5.1.1, there are reasons to align the gate very close to the source, and depending on the design of the source contact, there is a limit to how close alignment can be achieved. With regrown contacts, the gate can be positioned right at the regrowth edge, if the regrowth does not extend too high above the sample surface. For such close gate alignment, the ohmic contact metal has to be stepped back from the regrowth edge, which therefore requires the regrowth to be highly conducting, to keep the total source resistance low. The requirement of low contact resistance, together with high conductance, calls for an n^+-GaN regrowth, with an optional $Al_{0.35}Ga_{0.65}N$ cap, as suggested in §5.1.1. The 'low-profile' selective area growth developed in §4.7 is a suitable growth technique, since it allows large lateral growth without any vertical growth above the mask.

Low-profile SAG was performed on two HEMT samples; on one sample the growth consisted of only GaN:Si, extending $\sim$ 10 μm laterally from the regrowth edge, and on the other sample the identical GaN:Si growth was performed, with an additional 20 nm $Al_{0.35}Ga_{0.65}N$ cap on top. Contact metal deposition, and isolation, was performed in the manner described earlier. The contact resistance was measured, on TLM patterns with varying contact alignment (the spacing between the metal contact edge and the regrowth edge). The results are plotted in Fig. 5.15,

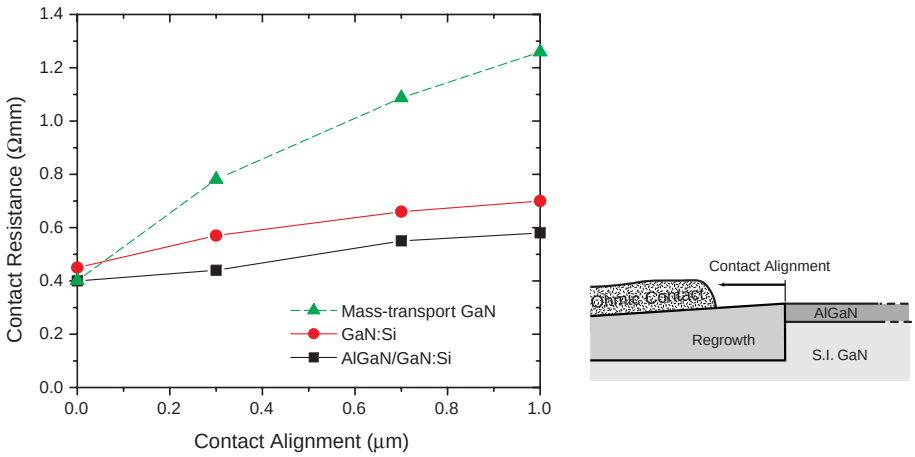

Figure 5.15: Contact resistance of ohmic contacts formed by low-profile selective area growth, as a function of contact alignment. The results of contacts formed by single-edge mass-transport growth are included as a comparison.

---

together with the results of the single-edge contacts performed by mass-transport growth (see §5.2.2), as a comparison. The sample with GaN:Si regrowth starts out at 0.45 Ωmm for zero contact alignment, and goes to 0.7 Ωmm for 1 μm alignment. The sample with AlGaN capped regrowth showed a somewhat lower contact resistance, starting at 0.4 Ωmm for zero contact alignment, increasing to 0.6 Ωmm for 1 μm alignment.

For further discussion of the results, the different components of the total contact resistance are illustrated in Fig. 5.16. The 'regrowth contact resistance' and the 'access region' are self-explanatory, and the '3D/2D transition' is the resistance associated with the transition from bulk conduction to the 2DEG of the HEMT structure, if any. Assuming that the regrowth contact resistance, and the 3D/2D transition

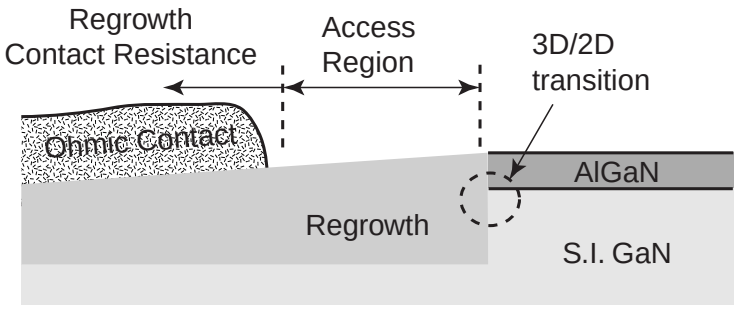

Figure 5.16: The different components of the total contact resistance.

stay constant, the sheet resistance of the access region can be obtained from the slope of the curves in Fig. 5.15. For the sample with Ga:Si regrowth, a value of 250 $\Omega/\Box$ was calculated, and for the sample with AlGaN capped regrowth, a lower value of 190 $\Omega/\Box$ was calculated. This is lower than the sheet resistance of a good HEMT structure, which usually is around 260 - 280 $\Omega/\Box$, a sign of a high Si doping level during regrowth. The measured contact resistance for zero contact alignment, 0.45 Ωmm for the GaN:Si regrowth, and 0.40 Ωmm for the AlGaN-capped regrowth, is the sum of the 'regrowth contact resistance' and the 3D/2D transition resistance. It is not possible to extract the individual resistances, from the data available for these two samples.

To clarify the influence of the 3D/2D transition on the contact resistance, low-profile contact regrowth was performed on a GaN MESFET structure. The structure consisted of a 0.4 μm GaN:Si layer, with a Si concentration of 1×10^{18} cm^{-3}, on a semi-insulating base-layer. The structure had no 3D/2D transition, since the device

channel is a 0.4 μm thick doped layer. The regrowth was identical to the AlGaN capped GaN:Si used previously for the HEMT structure. The resulting contact resistance at zero contact alignment was the same as for the HEMT, 0.40 Ωmm. This indicates that there is no significant resistance associated with the 3D/2D transition for contact regrowth to HEMT structures.

With the 3D/2D transition ruled out as a source of resistance, the 'regrowth contact resistance' alone must be responsible for the 0.40 - 0.45 Ωmm obtained for zero contact alignment. This contact resistance was not as low as could have been expected for this experiment. In other experiments, measuring the contact resistance with TLM patterns on highly doped GaN or AlGaN/GaN structures, very low values, down to $\sim$ 0.1 Ωmm, were sometimes obtained. The higher than expected contact resistances were probably an effect of the overall variation experienced for the ohmic contact process, also for non-regrown contacts. The variations can be addressed by using a more optimized metallization scheme,[8] and by exercising better process control. By doing so, in combination with optimization of the regrowth, I believe a total contact resistance of less than 0.2 Ωmm is achievable with the low-profile regrowth technique.

5.5 Drain Regrowth

RF dispersion is one of the major factors that can limit the RF power performance of AlGaN/GaN HEMTs. RF dispersion is the difference between the drain output curves obtained at a low gate modulation frequency, and those obtained at a high modulation frequency. Trapping of free charge from the channel, in slow traps, is the reason for the RF dispersion, and there is extensive evidence that the responsible traps are located on the sample surface. During the gate voltage swing, electrons migrate out onto the surface from the gate, towards the drain, occupying surface states. This creates a virtual extension of the gate, which can not be modulated at a high frequency due to the slow response time of the surface states. A surface passivation with SiN has been shown to be effective in removing the RF dispersion, but the exact mechanism with which the dispersion is suppressed is presently unclear. A detailed investigation of the RF dispersion, the role of surface states, and the SiN passivation, can be found in ref. [40].

To gain further insight into the problem of RF dispersion, an alternative solution to the SiN surface passivation, involving non-planar selective area growth, was developed. The structure is illustrated in Fig. 5.17a. The region under the drain, and between the gate and the drain, was subject to a selective etch, followed by selective area growth of Si doped GaN and a 20 nm $Al_{0.35}Ga_{0.65}N$ cap layer. The nominal planar thickness of the GaN layer was 170 nm, and the Si doping was 4×10^{17} cm^{-3}.

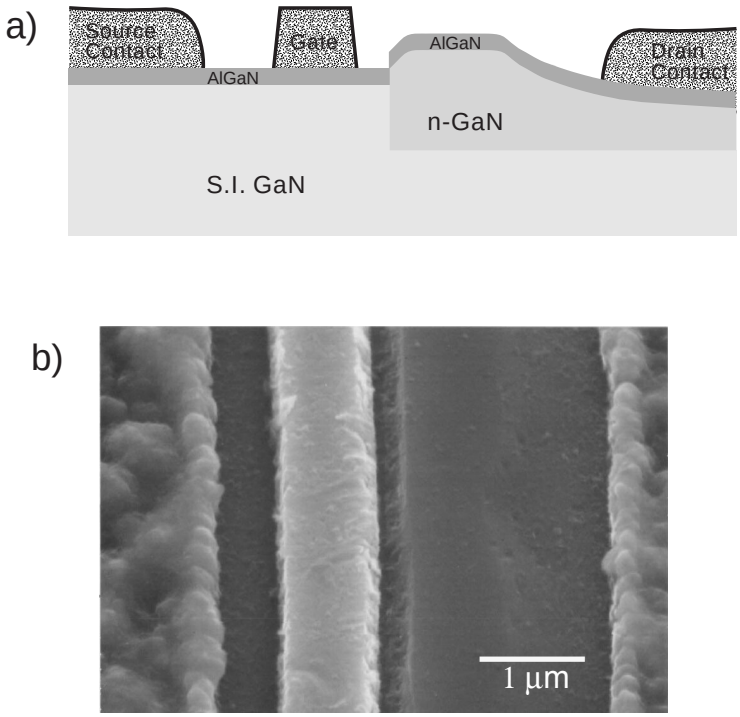

Figure 5.17: Device with drain regrowth, to eliminate RF dispersion. a) Schematic of device, with the gate to regrowth edge spacing L_{gr} marked. b) SEM image of fabricated device, taken at a 45° angle.

The spacing between the gate, and the edge of the drain regrowth, labelled L_{gr}, was varied between 0.12 μm, and 2 μm (the full gate-drain spacing). Fig. 5.17b shows an SEM image of the fabricated device, in this case with L_{gr} = 0.24 μm.

The regrowth was performed with an AlN mask, to eliminate auto-doping effects from the mask. Similar growth conditions to the study in §4.3 and §4.6 were used, notably a temperature of 960°C.

The purpose of the n-GaN/AlGaN regrowth was to provide additional charge in the gate-drain region. The Si-doping provided a nominal sheet charge of 7×10^{12} cm^{-2}

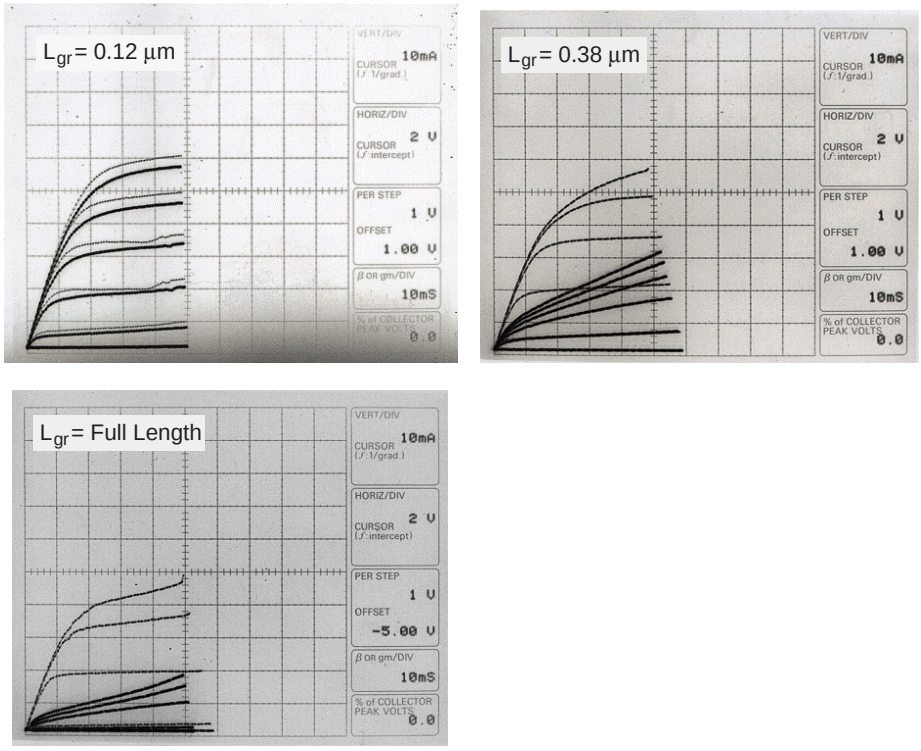

Figure 5.18: I-V curves for drain regrowth devices. The thin lines show the DC sweeps, and the thick lines show the 80 μs pulsed gate response. The device with the regrowth closest to the gate (L_{gr} = 0.12 μm) showed almost no dispersion

---

in the n-GaN, beneath $\sim 1\times10^{13}$ cm^{-2} in the 2DEG formed at the n-GaN/AlGaN interface. As charge trapped on the AlGaN surface depleted parts of the 2DEG, the additional bulk charge ensured that enough charge was available for unperturbed current transport.

Fig. 5.18 shows the I-V curves for fabricated devices with various L_{gr}. The device with no regrowth between gate and drain (L_{gr} = Full length), showed severe dispersion. As the regrowth edge was moved to a distance of 0.38 μm from the gate, a small improvement was seen, and for L_{gr} = 0.12 μm the dispersion was almost

completely eliminated. However, with the improvement in dispersion followed a reduction in breakdown voltage. For no regrowth between gate and drain, the three terminal breakdown voltage was over 70 V. As L_{gr} was reduced to 0.2 μm, the breakdown voltage was reduced to 25 V, and when L_{gr} was less than zero, the breakdown voltage was essentially zero. The reason for the low breakdown was the high charge density located near the drain side of the gate, giving rise to high electric fields. The nominal Si concentration of 4×10^{17} cm^{-3} was too low to cause the low breakdown voltages, however, as was covered in §4.6, the doping density near the regrowth edge is far higher than the nominal doping density far from the mask edge. Comparing the drain regrowth with the samples studied in §4.6, it can be estimated that the sheet conductance near the regrowth edge was at least 5 times higher than the nominal planar value. In terms of charge, the increase near the regrowth edge was higher, probably about 10 times the nominal planar value, due to the decrease in mobility with increased doping concentration. This would mean a doping concentration of $\sim 4 \times10^{18}$ cm^{-3}, which is high enough to cause premature breakdown.

The breakdown problem made the devices unattractive for power applications, but the experiment served to clarify the lateral extent of the surface trapping responsible for RF dispersion. The measurements clearly show that the surface trapping occurred only within $\sim$ 0.3 μm of the gate, an observation with impact on other device designs as well. For gate recess structures aimed at reducing dispersion, for example the p-GaN capped HEMT,[41] the gate-to-recess-edge spacing must be

much smaller than 0.3 μm to benefit from the recess structure.

5.6 Channel Degradation near Regrowth Edge

The regrown contacts discussed so far in this chapter have been characterized with respect to contact resistance, and the presented results were relatively consistent. There were other experiments, where the data was not so consistent, and no reliable contact resistance could be obtained. The inconsistencies were particularly severe for the device that will be presented at the end of this chapter, the hot electron HEMT (see §5.7). In this section, the inconsistencies will be discussed in some detail, and some experimental data will be presented that in part explains the observations.

The particular samples that will be discussed were part of the study in §5.7, where the devices have regrown sources, but regular drain contacts. In this section the regrown contact will therefore be referred to as the source, and the normal contact as the drain. A special type of TLM structure was designed to enable the measurement of the total source resistance. The 'total source resistance' is here defined as the sum of the contact resistance, the access resistance, and the resistance at the vertical regrowth interface (if any), similar to the components described in Fig. 5.16. The total source resistance acts as a parasitic resistance, affecting device properties such as current saturation, and f_T, as described in §5.1.

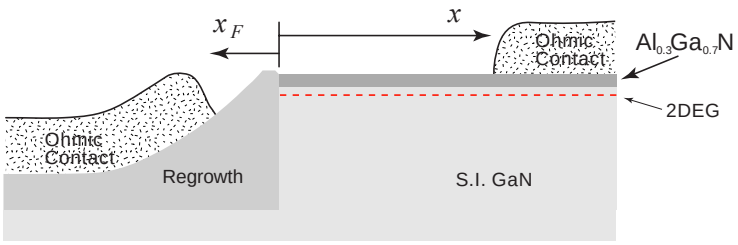

Figure 5.19: The element of a special TLM structure designed to measure the total source resistance of a device with regrown source. x_F is fix, while x is varied.

The basic element of the TLM structure is illustrated in Fig. 5.19. It has two contact pads, one located in the regrowth region (source), at a fixed distance x_F to the mesa edge, and the other one is located on the HEMT material (drain), at a variable distance x to the mesa edge. The total TLM structure consists of several basic elements, each with a different x. When plotting the measured resistances, as a function of x, the slope describes the sheet resistance in the HEMT material, while the intersect with the vertical axis equals the sum of the total source resistance, and the drain contact resistance. The drain contact resistance can be obtained separately from regular TLM measurements, performed entirely on HEMT material. By subtracting the drain contact resistance, the total source resistance can be obtained from the measurements.

When applied to samples with regrown source, the test-structure had limited success in measuring the total source resistance, but it served to illustrate another problem associated with the regrowth. Fig. 5.20 shows the result of measurements

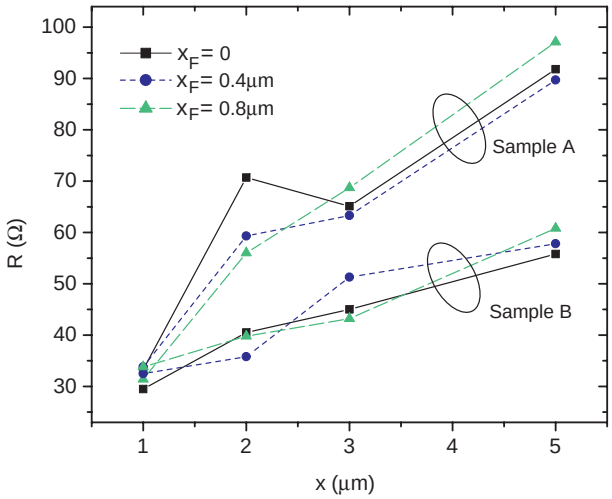

Figure 5.20: Result of TLM measurements on two different samples, using the structure illustrated in Fig. 5.19. Three separate TLM structures were measured per sample, each corresponding to a different value of x_F. Sample *A* was fabricated from HEMT material with sheet resistance 650 $\Omega/\Box$, and the source regrowth consisted of GaN:Si with a 20 nm $Al_{0.35}Ga_{0.65}N$ cap. Sample *B* was fabricated from HEMT material with sheet resistance 380 $\Omega/\Box$, and the source regrowth consisted of $Al_{0.05}Ga_{0.95}N$:Si, followed by a 20 nm $Al_{0.35}Ga_{0.65}N$ cap.

---

on two different samples. Three separate TLM structures were measured per sample, each corresponding to a different value of x_F. The sample marked *A* was fabricated on a HEMT sample with relatively high sheet resistance, 650 $\Omega/\Box$, and the source regrowth consisted of GaN:Si with a 20 nm $Al_{0.35}Ga_{0.65}N$ cap. The sample marked *B* was fabricated from a HEMT structure with a lower sheet resistance of 380 $\Omega/\Box$, and the source regrowth consisted of $Al_{0.05}Ga_{0.95}N$:Si, also with a 20 nm $Al_{0.35}Ga_{0.65}N$ cap. The sheet resistances were measured by standard TLM patterns, located far from the regrowth areas. The GaN and $Al_{0.05}Ga_{0.95}N$ non-planar selective area growths were performed according to conditions in §4.2 - §4.4, to a planar

thickness of 85 nm. In Fig. 5.20 the resistances did not show a linear dependence on x, in particular for sample A for x_F = 0 and 0.4 μm. A non-linear relation can mean one of two things: either the contact resistances varied with x, which seems unlikely, or the sheet resistance of the 2DEG was not uniform. A non-uniform sheet resistance could be caused by damage during growth, reactive ion etching, or during other processing. Furthermore, linear fits to the data gives an average sheet resistance of 1400 $\Omega/\Box$ for sample A, and 660 $\Omega/\Box$ for sample B, which is about twice the values measured on the HEMT material far from the regrowth.

It is presently not clear how to correctly interpret this data, but some trends can be identified. The difference in the regrowth structure should have only a marginal effect on the measurement, insufficient to cause the observed difference in characteristics between sample A and B. Instead, the difference is probably related to a certain small difference in the fabrication process prior to the source regrowth. On both samples, a photo-resist pattern was defined by exposure and development, followed by evaporation of the SiO_2 regrowth mask, and lift-off in solvents. For sample A, the SiO_2 was evaporated onto the sample right after the photo-resist patterning. On sample B, a 30 sec O_2 plasma etch was performed prior to SiO_2 deposition, to remove any remaining photo-resist residue from the developed areas. Although a subtle difference, the trend was true for other samples processed the same way as sample A or B. The presence of photo-resist residue under the SiO_2 mask can have the following effects. After lifting off the SiO_2, it was necessary to clean the sam-

ples before the Cl_2 RIE (see §3.2). During the clean, either by soak in developer, or by O_2 plasma etching, if photo-resist residue is present under the SiO_2 mask, it can get etched laterally, undercutting the SiO_2, causing poor sticking. Poor mask sticking was in fact observed at the mask edge, on a few occasions, when the cleaning was performed by soak in developer. During the subsequent growth, a poorly sticking mask may expose the active layer surface to the growth ambient, causing degradation of the channel transport properties.

Another experiment was conducted to confirm the degradation of the channel near the regrowth edge, in devices processed like sample *A*. The experiment used incremental conductivity measurements to gauge the quality of the HEMT material near the regrowth edge, performed on narrow etched of variable width, as illustrated in Fig. 5.21a. The same type of test structure was used in §4.6, to measure the sheet conductance of regrown material near the mesa edge, and the details of the technique can found there. For the present measurement, the mesas were aligned to measure the sheet conductance of the HEMT material, in the $0 < x < 1.4$ μm region for one die, and in the $4 < x < 5.4$ μm region for another die (x is the distance from the regrowth edge). The measured conductance *vs.* distance from the regrowth edge, is plotted in Fig. 5.21 for both dies. In the $4 < x < 5.4$ μm range (Fig. 5.21a), the measured points lie on an approximately straight line, with a slope of 3.4 mS·μm. The constant slope corresponds to a constant sheet conductance, and by taking the inverse, a sheet resistance of 295 $\Omega/\Box$ is obtained. This is consistent

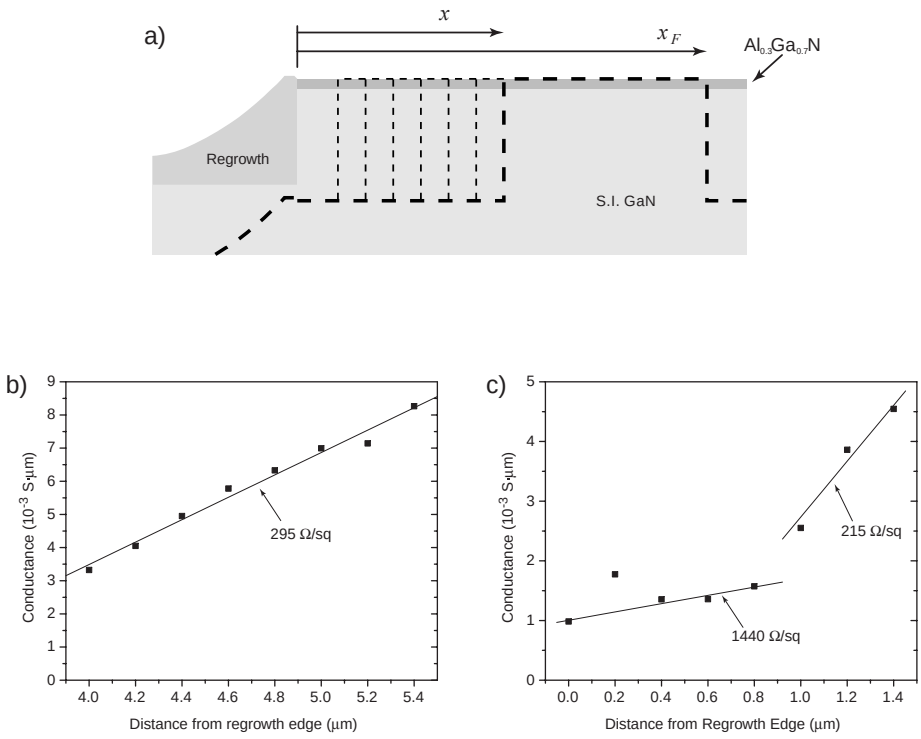

Figure 5.21: Incremental conductivity measurements of HEMT structure near regrowth edge, using mesas of variable width etched in the HEMT structure near the regrowth edge. a) Illustration of the etched mesas, marked by the dashed line. The dimension x_f was held constant, while x was varied. b-c) The slope of the data indicates the sheet conductance, and its inverse, the sheet resistance, is indicated in the plots. b) Measurements within 1.4 μm of the regrowth edge. c) Measurements between 4 and 5.4 μm from the regrowth edge.

---

with a sheet resistance of 289 $\Omega/\Box$ obtained by large area TLM measurements. In the $0 < x < 1.4$ μm range (Fig. 5.21b), the measured points do not form a straight line, they rather fall on two lines, one from 0 to 0.8 μm, with a slope corresponding to 1440 $\Omega/\Box$, and one from 0.8 to 1.4 μm, with a slope corresponding to 215 $\Omega/\Box$. The sheet resistance of 1440 $\Omega/\Box$ is 5 times higher than the value obtained from the large area measurement, indicating a severely degraded channel in the 0.8 μm

HEMT material closest to the regrowth edge. These measurements show that the previous measurements obtained using the test-structure in Fig. 5.19 are due to a degraded channel conductivity near the regrowth edge, probably caused by delamination of the SiO_2 mask near the mask edge.

5.7 Hot Electron HEMT

In §5.1.2, a device with an $Al_{0.05}Ga_{0.95}N$ regrown source was proposed, to address the generally low f_T observed for AlGaN/GaN HEMTs. In this section, the growth, fabrication, and characterization, of such a device is described.

A schematic of the proposed device structure is shown in Fig. 5.22a. The structure consists of a Si doped $Al_{0.05}Ga_{0.95}N$ source regrowth, with a 20 nm $Al_{0.35}Ga_{0.65}N$ cap layer, and an e-beam gate aligned very closely to the regrowth edge. The gate alignment, the spacing between the foot-print of the e-beam gate and the source regrowth edge, is labelled L_{gr}. The purpose of the source regrowth is to increase the electron drift velocity under the gate, through the high quasi-electron field at the vertical interface between the $Al_{0.05}Ga_{0.95}N$ regrowth and the GaN channel. To benefit from the momentum gained at the interface, the gate must be placed within a short distance of the regrowth edge, perhaps 0.3 μm or smaller (see §5.1.2). The e-beam gates used for the device had a foot-print of nominal length 0.2 μm, sufficiently small to place within 0.3 μm of the regrowth edge. To achieve close gate align-

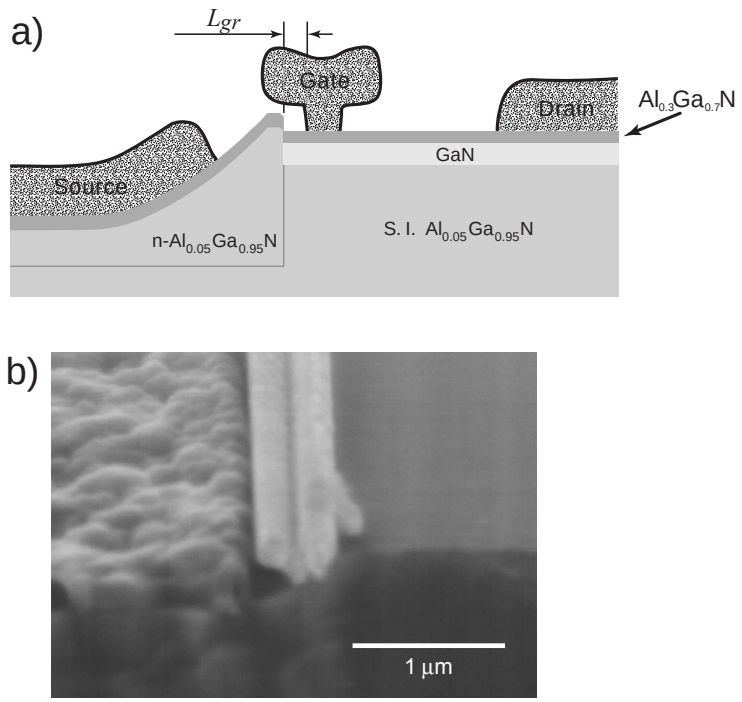

Figure 5.22: Hot electron device for enhanced electron drift velocity under the gate. a) Schematic of device cross-section, showing the $Al_{0.05}Ga_{0.95}N$ source regrowth, and the close aligned gate. The important gate-to-regrowth-edge spacing is labelled L_{gr}. b) SEM image of a fabricated device, here with L_{gr} = -0.18 μm (gate overlapping the source regrowth).

---

ment, each die contained several identical devices, with staggered gate alignment L_{gr}, nominally ranging from +0.12 μm to -0.24 μm in steps of 0.06 μm. With the staggered gates, at least one device would have an actual L_{gr} of 0.06 μm or less. The base-layer of the device was a semi-insulating $Al_{0.05}Ga_{0.95}N$ film, chosen instead of a GaN layer to ensure that the current injection from the regrown source occurred in the 30 nm thin GaN channel. Fig. 5.22b shows the SEM image of the source-gate region of a fabricated device. This particular device had a nominal L_{gr} of -0.18 μm, which means that the gate overlapped 0.18 μm onto the source regrowth.

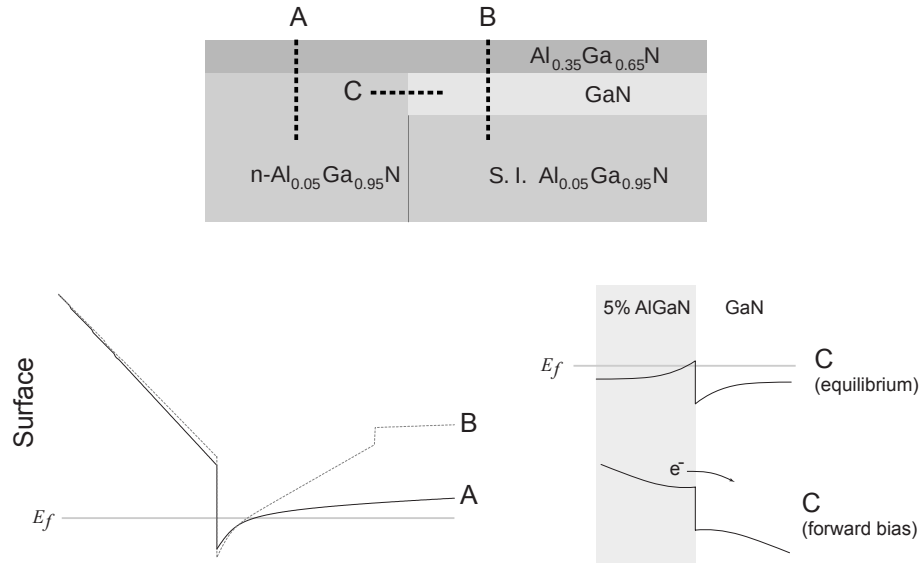

Figure 5.23: Schematic band diagram of hot electron HEMT.

To accurately model the band diagram of the device, a simultaneous solution of Poisson's equation and the Schrödinger equation, in 2 dimensions, is necessary. Short of that, some schematic band diagrams are presented in Fig. 5.23, showing the conduction band along several lines through the device structure. Lines A and B go vertically through the structure, in regrowth region and the masked region, far from the regrowth edge. The bands are drawn for equilibrium conditions, and look very similar in the region of the 2DEG. Along the 2DEG across the regrowth interface (line C), the crucial part of the device, it is difficult to draw the bands without the full 2D solution. However, a depletion and accumulation region must be present on either side of the conduction band discontinuity, as illustrated in Fig. 5.23. The lateral

extent of the depletion/accumulation regions depend not only on the doping densities in the respective materials, but also on the interaction with the $Al_{0.35}Ga_{0.65}N$ cap layer. If the depletion/accumulation regions are too short, the electrons can enter the channel from the regrowth region by tunneling, which would compromise the intended effect of the source regrowth.

The selective area growth of the $Al_{0.05}Ga_{0.95}N$ was performed similar to the $Al_{0.1}Ga_{0.9}N$ growth described in §4.4. Far from the regrowth edge, the nominal $Al_{0.05}Ga_{0.95}N$ thickness was 128 nm, and the Si doping concentration was 1.4×10^{18} cm^{-3}. TLM measurements on the fabricated device gave a drain contact resistance of 1.0 Ωmm, and a sheet resistance for the HEMT structure of 420 $\Omega/\square$. Contacts formed on the regrown material had a contact resistance of 0.3 Ωmm, and the sheet resistance of the regrown material was 670 $\Omega/\square$.

The transition from the regrown source to the HEMT material was tested, according to the method developed in §5.6. The first fabricated devices showed poor behavior, suggesting severe degradation of the HEMT material near the regrowth edge. After changing the fabrication procedure, as outlined in §5.6, some improvement was achieved, similar to the better sample presented in Fig. 5.20. However, the transition was still far from ideal, which, in the end, had detrimental effects on the device high frequency performance.

DC output characteristics are presented in Fig. 5.24, for a reference device without source regrowth, and for four devices with source regrowth, with varying gate

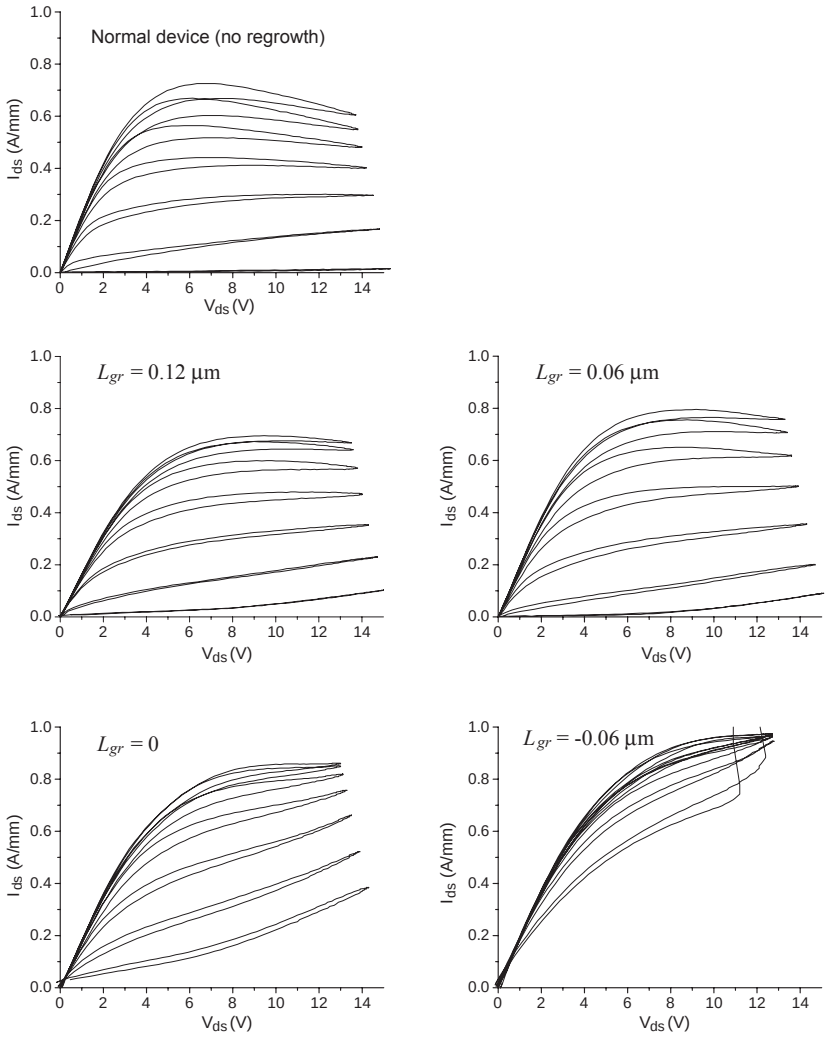

Figure 5.24: Drain output characteristics for a reference device without regrown source, and four devices with source regrowth. All devices showed relatively low currents, due to a low sheet charge in the starting material, and a higher-than-usual output conductance, consistent with the short gate length. The regrown devices with L_{gr} = 0.12 μm and 0.06 μm showed normal characteristics, while the devices with L_{gr} = 0 and -0.06 μm showed severe source drain leakage.

---

alignments. All devices, including the reference device, showed relatively low currents, due to a relatively low channel charge in the starting HEMT material, related to back-depletion by the 5% AlGaN base-layer. The fact that the current levels

were about the same, with and without regrowth, suggested that the source regrowth at least did not impair the basic device operation. All devices also had a higher than usual output conductance, due to the short gate length. The regrown devices with L_{gr} = 0.12 μm and 0.06 μm showed normal operating characteristics, but for L_{gr} = 0 the current could not be pinched off, and for L_{gr} = -0.06 μm, nearly all gate modulation was lost. The loss of pinch-off was attributed to the overlap of the gate footprint onto the source regrowth region, which was n-type doped.

S-parameters were measured on the functioning devices, after deposition of SiN surface passivation, as a function of frequency, to extract the unity current gain frequency f_T. The optimum bias conditions, with respect to f_T, were around V_{ds} = 10 V, and V_{gs} = -4 V (1 - 2 V above pinch-off), giving current densities of 0.20 - 0.25 A/mm. The current gain h_{21}, and the unilateral power gain (UPG), are given as a function of frequency in Fig. 5.25, for one normal and one device with source regrowth, biased at the optimum conditions. The usual 20 dB/decade extrapolation of h_{21} gives an f_T of 54 GHz for the normal device, and 44 GHz for the device with source regrowth (same for both L_{gr} = 0.12 μm and 0.06 μm). The devices with regrown source had *lower* f_T than the normal devices, suggesting that the $Al_{0.05}Ga_{0.95}N$ source regrowth did not have the intended effect. Following are some measurements, and discussions, trying to explain why an improvement was not achieved. It will be argued that the improvement, if any, was overshadowed by the parasitic source and drain resistances.

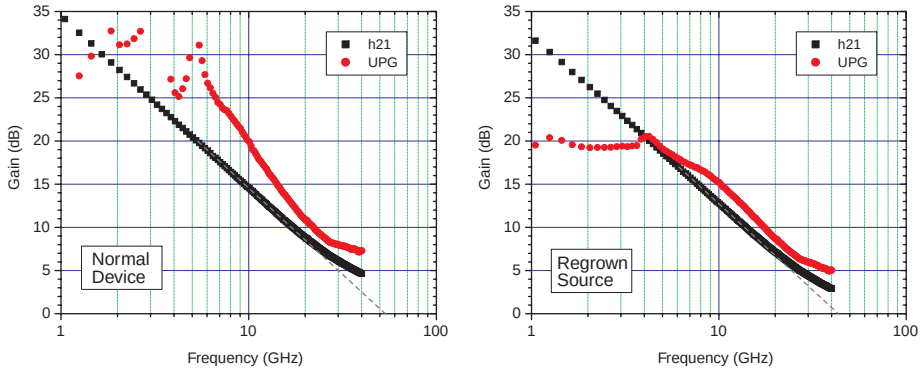

Figure 5.25: S-parameter measurements of devices with and without source regrowth, after SiN surface passivation. The unity current gain (f_T) can be obtained using the standard 20 dB/decade extrapolation of the short-circuit current gain. For the normal device an f_T of 54 GHz was obtained, and for the device with source regrowth, an f_T of 44 GHz was obtained.

To extract the parasitic resistances of the device, endpoint resistance measurements were performed. To measure the source resistance, a large current was forced from the gate to the source, while the potential of the drain, which was left floating, was recorded. Since no current flowed through the drain electrode, the drain could be used to probe the potential in the channel under the gate, and by relating this to the gate (source) current, an estimate of the source resistance could be obtained. Fig. 5.26 shows the results of a measurement on a normal device (without regrowth), with both the gate voltage and the drain voltage plotted as a function of the forced gate current. The gate voltage showed forward biased diode characteristics, while the drain voltage showed a linear dependence on the gate current, up to a gate current of about 0.3 A/mm. The average slope, in the range 0 to 0.3 A/mm, was 2.3 Ωmm, and is an estimate of the source resistance for low currents. At higher currents some

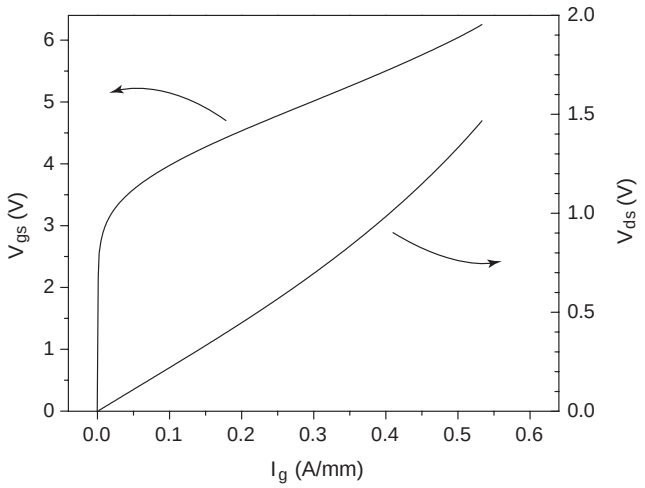

Figure 5.26: Measurement of source endpoint resistance. Gate and drain voltage are plotted *vs.* the forced gate current. The slope of the drain voltage curve gives the source resistance. The average source resistance over the current range 0 - 0.3 A/mm was 2.3 Ωmm for this particular device.

---

saturation in the current is evident, leading to a higher source resistance. Repeating the measurement, with source and drain exchanged, gave a value of 1.2 Ωmm for the drain resistance. The estimated source and drain resistances add up to 3.5 Ωmm, which compares to an on-resistance of 3.8 Ωmm obtained from the linear portion of the normal I_{ds} - V_{ds} curves. The fact that the drain resistance was smaller than the source resistance suggests that the gate of this device was located closer to the drain, due to misalignments.

The same measurements performed on a device with source regrowth resulted in a source resistance of 2.3 Ωmm, and a drain resistance of 2.2 Ωmm. These numbers add up to 4.5 Ωmm, which is identical to the on-resistance measured for the device. This resistance is higher than for the normal device, which may explain the lower f_T,

since f_T has a second-order dependence on the parasitic source and drain resistances (see §5.1.2). Furthermore, it can be noted that source and drain resistance was about equal, despite the close alignment of the gate to the source regrowth edge. In large area TLM measurements on the regrown material, the contact resistance was only 0.3 Ωmm, and the sheet resistance was 670 Ωmm. From these values, the expected source resistance calculates to only 0.6 Ωmm (for a 0.4 μm source access region). The large discrepancy between this value, and the measured value of 2.3 Ωmm, shows that the source regrowth is associated with a substantial resistance, either at the regrowth interface, or through degradation of the HEMT structure near the regrowth edge (see §5.6).

For both normal devices and regrown devices, the parasitic resistances were quite high. This was in part due to the high drain contact resistance of 1.0 Ωmm, probably caused by the $Al_{0.05}Ga_{0.95}N$ base layer of the HEMT structure, and in part to the long (3.5 μm) source to drain spacing. The high parasitic resistances reflect negatively on f_T; the measured values of 44 - 54 GHz are on the low side of published values for gate lengths of 0.2 μm, which range from about 50 to 90 GHz (see Fig. 5.5). It can therefore be concluded that f_T was to a large extent limited by the parasitic resistances, and any effect of the $Al_{0.05}Ga_{0.95}N$ source regrowth was therefore overshadowed.

In addition to the high source and drain resistances, there are a few more reasons why the $Al_{0.05}Ga_{0.95}N$ source regrowth may not have worked as intended. As

was shown in §4.5 for $Al_{0.1}Ga_{0.9}N$ selective area growth, the Al composition in the 0.6 μm closest to the regrowth edge was 7%, lower than the 10% obtained far from the regrowth edge. Analogous to that, the $Al_{0.05}Ga_{0.95}N$ regrowth used for the present device, probably resulted in an Al composition of $\sim$ 3% near the regrowth edge, which would lead to a smaller conduction band discontinuity than intended. Furthermore, the impurity incorporation was in §4.6 shown to be enhanced near the regrowth edge, for GaN regrowth. For a nominal Si doping of 1.5×10^{18} cm^{-3}, the sheet conductance near the mask edge was about 5 times higher than far from the mask. Assuming the same trend is true for $Al_{0.05}Ga_{0.95}N$ growth, and considering the decrease in mobility with increased doping concentration, it can be estimated that the n-type doping concentration was 10 times higher than the planar value, which would mean 1.5×10^{19} cm^{-3}. This high doping density at the regrowth edge would negate the effect of a conduction band discontinuity, by allowing the electrons to tunnel through to the HEMT channel. In retrospect, it can be concluded that an undoped $Al_{0.08}Ga_{0.92}N$ source regrowth would have been better, to reach the desired target composition, and to limit the n-type doping at the regrowth edge.

In conclusion, f_T of the 'hot electron' HEMT was largely limited by parasitic resistances, and no conclusions can be reached about whether hot electron injection under the gate is a good idea or not. In a way one can say that the hot electron HEMT was ahead of its time; the technology was not mature enough for the device to show its potential. At a later time, when the issue of current transport from regrowth to

channel has been addressed, it may be worthwhile to revisit the device.

5.8 Discussion and Future Work

An number of device structures utilizing selective area growth were demonstrated in this chapter, with the goal of improving certain device characteristics. The degree of success varied, in part due to problems associated with the current transport from the regrowth region into the HEMT channel. This is the most important issue to solve, and this must be done before any other device work can continue.

5.8.1 Current Transport across Regrowth Edge

The transport properties across the vertical regrowth edge showed inconsistencies throughout this work, probably due to process variations not under control. The highly doped ohmic contact regrowths presented early in this chapter functioned well, but there were instances of inconsistent transport behavior for similar devices. The less doped source regrowth, for the hot electron device, seemed to be more sensitive to the problem, and no good transport across the interface could be achieved in several processed devices.

In §5.6 it was shown that the transport properties in the HEMT structure near the regrowth edge could be severely degraded, as a result of delamination of the regrowth mask, or other factors. This degradation is the first problem that needs to be

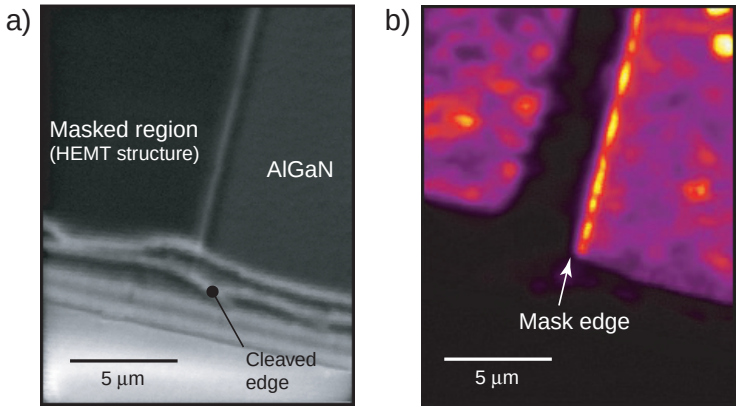

Figure 5.27: Cathodoluminescence microscopy of $Al_{0.1}Ga_{0.9}N$ non-planar SAG at a regrowth edge. a) SEM image. b) CL intensity image of the entire spectral region. The CL intensity is very low in the 3 μm masked region closest to the regrowth edge.

addressed, and as a tool to quickly quantify the damage, I propose using cathodoluminescence (CL) microscopy. Fig. 5.27 shows an SEM image, and a CL image, of the same area of an $Al_{0.1}Ga_{0.9}N$ regrowth sample, obtained as part of the Al composition gradient study in §4.5. The feature of interest here is the stripe of low luminescence intensity in the HEMT material closest to the regrowth edge, running parallel to the regrowth edge. The sample was processed identical to the 'bad' sample in Fig. 5.20 (see §5.6), and it is believed that the low intensity is related to the degraded transport properties in the same region. By characterizing samples with CL after each processing step, and by varying the process, it should be possible to determine when the damage occurs, and why. The large scale damage probably occurs during regrowth, caused directly or indirectly by photo-resist residues. On a shorter lateral scale, it is possible that the reactive ion etch causes damage, which

could perhaps be addressed by looking into alternative etching methods, such as inductively coupled plasma RIE, or photo-electro-chemical etching.

Once a satisfactory luminescence intensity can be obtained from the HEMT material near the regrowth edge, the electrical characterization tools developed in this dissertation can be used for further optimization. These tools include measuring the conductivity of thin slices of material, running parallel to the regrowth edge, as described in §4.6 and §5.6, as well as measurements across the vertical regrowth interface, as detailed in §5.6.

Another tool for characterizing the vertical regrowth interface is transmission electron microscopy (TEM), with which details of structural defects at the interface can be obtained.

5.8.2 Ohmic Contacts

Even among the devices that had consistent transport properties from the regrowth region into the HEMT channel, significant variation in the ohmic contact resistance could be observed. In some cases the variations were related to the contact metallization, due to a non-uniform deposition rate in the e-beam evaporator used for the contact metallization. It has been shown by Dario Buttari that the contact resistance depends strongly on the metal thicknesses,[8] and by controlling it carefully the variations can be minimized.

In some instances there were variations that could not be attributed to the met-

allization. In at least one case photo-resist residue between the contact metal and the semiconductor was responsible for an increased contact resistance. In my experience, the amount of photo-resist residue left after development, or photo-resist removal, varies substantially, perhaps due to improper photo-resist use, or use of aged photo-resist. By paying close attention to the details in the processing, and consulting with the manufacturer, this issue can probably be solved.

5.8.3 Ohmic Contacts by Mass-Transport Growth

Ohmic contact regrowth was successfully demonstrated using mass-transport growth. The growths were performed by annealing of samples in ammonia and hydrogen, without external supply of gallium. The autodoping from the SiO_2 mask was sufficient to supply high levels of n-type doping for the growth, eliminating the need for an external dopant source. The technique caters to the need for a cheap and simple contact regrowth technique, since it can potentially be performed in a simple ammonia annealing chamber.

The technique may also be useful for fabrication of high-performance HEMTs, in particular the next generation scaled devices with ultra-short gate lengths and gate-source spacings, after some further optimization. I would like to mention two aspects where I think there is room for improvements. As was suggested in §3.8, oxygen doping of the mass-transport growth could lead to increased n-type doping levels, which could help in lowering the contact resistance of the regrown ohmic

contacts, and would allow the metal edge of the contact to be stepped back further from the regrowth edge. The other factor, that has not been mentioned so far, is the mask layout, specifically the fill-factor. The fill-factor was small (most of sample area masked) for all mass-transport growths, except one. The sample with large fill-factor had relatively high contact resistance, presumably due to the presence of less SiO_2, from which the n-type doping originates. On the other hand, the supply of growth species was plentiful, coming from the large unmasked areas, which reflected in very good fill-in of the trenches used for contact formation, and a less temperature sensitive growth morphology. Before the mass-transport growth technique is launched into the mainstream HEMT process, the fill-factor should first be optimized.

5.8.4 Ohmic Contacts by Low-Profile Regrowth

The low-profile contact regrowth showed potential for reducing source and drain parasitic resistances, but more optimization is needed before it can offer a substantial advantage over regular annealed contacts formed directly to the HEMT structure. Part of the optimization lies in establishing better process control for the ohmic metallization, as described in §5.8.2, but there is also room for optimization in the layer structure of the regrowth. The bulk of the regrowth is GaN, which can be heavily Si doped, as was done for the present device, or oxygen doped (see §3.8). On top of the n^+-GaN, a cap layer can be deposited, either a plain 20 nm $Al_{0.35}Ga_{0.65}N$, as was

used in the present device, or any other structure that gives low contact resistance and a low sheet resistance. Potential cap-layers include GaN-AlGaN grades, InGaN, thin AlN, and n^{++} material doped so high that the morphology becomes rough.

After optimization of the contact resistance, the obvious step will be to fabricate a device, with an e-beam gate closely aligned to the source regrowth edge. Testing the device will show if device characteristics such as soft current saturation, high knee voltage, g_m compression, and low f_T, are improved, as was suggested in the motivation section of this chapter.

5.8.5 Hot Electron HEMT

The hot electron HEMT is an interesting device concept, but in the implementation described previously in this chapter, the high frequency performance was largely limited by parasitic resistances, and the true potential of the device could not be evaluated. Once the issues associated with current transport across the regrowth edge have been solved, a new attempt to fabricate the device can be made. However, a few things should be different from the device described in this chapter. The starting material should be a standard HEMT, with the lowest possible sheet-resistance, on a semi-insulating GaN base-layer. The 5% AlGaN base-layer used in the present device resulted in a high drain resistance, and a higher-than-usual sheet resistance. A shorter source to drain spacing, in combination with a low sheet resistance, and low contact resistances, will serve to minimize the parasitic source and drain resistances.

Also, devices with several different Al compositions, and several Si doping levels (including zero), in the source regrowth, should be fabricated to find the optimum combination.

As was clear from the attempt to draw the band diagram of the device at the regrowth/channel interface, a simulation of the device is needed. Our current simulation software from Silvaco does not include solving of the Schrödinger equation, which is necessary in this type of device. However, if the device is to be pursued, one may consider acquiring the appropriate software to allow accurate device modelling.

Instead of going straight to the complete device structure, the possibility of hot electron injection, and the duration of transient phenomena, could be investigated separately in a vertical structure. A vertical structure would give better control over layer thicknesses, doping, and Al composition in the AlGaN. The electron velocity, and transient behavior, could be measured with time-resolved electroabsorption measurements, as has been demonstrated by Wraback *et al.*.[29, 4] However, a vertical structure would be affected by the polarization present in the (0001) direction. For full accuracy the structure should be grown in a non-polar direction, which in the absence of GaN substrates is a difficult task.

References

[1] S. M. Sze. New York, NY: John Wiley & Sons, 2nd ed., 1981.

[2] J. S. Moon, M. Micovic, P. Janke, P. Hashimoto, W. S. Wong, R. D. Widman, L. McCray, A. Kurdoghlian, and C. Nguyen *Electron. Lett.*, vol. 37, p. 528, 2001.

[3] J. Kolník, I. H. Oğuzman, K. F. Brennan, R. Wang, P. P. Ruden, and Y. Wang *J. Appl. Phys.*, vol. 78, p. 1033, 1995.

[4] M. Wraback, H. Shen, J. C. Carrano, T. Li, J. C. Campbell, M. J. Schurman, and I. T. Ferguson *Appl. Phys. Lett.*, vol. 76, p. 1155, 2000.

[5] C. H. Chen, S. Keller, G. Parish, R. Vetury, P. Kozodoy, E. L. Hu, S. P. DenBaars, and U. K. Mishra *Appl. Phys. Lett.*, vol. 73, p. 3147, 1998.

[6] T. Furutsuka, T. Tsuji, and F. Hasegawa *IEEE Trans. Electron Dev.*, vol. ED-25, p. 563, 1978.

[7] H. M. Macksey, F. H. Doerbeck, and R. C. Vail *IEEE Trans. Electron Dev.*, vol. ED-27, p. 467, 1980.

[8] D. Buttari, R. Coffie, L. Shen, S. Heikman, S. Keller, and U. K. Mishra *submitted to IEEE Electron Device Letters*, 2002.

[9] V. Kumar, W. Lu, F. A. Khan, R. Schwindt, A. Kuliev, G. Simin, J. Yang, M. Asif Khan, and I. Adesida *Electron. Lett.*, vol. 38, p. 252, 2002.

[10] V. Kumar, W. Lu, F. A. Khan, R. Schwindt, A. Kuliev, J. Yang, A. A. Khan, and I. Adesida p. 25.1.1, 2001. International Electron Devices Meeting. Technical Digest, Washington, DC, USA 2-5 Dec. 2001 Piscataway, NJ, USA IEEE.

[11] V. Kumar, W. Lu, R. Schwindt, J. Van Hove, P. Chow, and I. Adesida *Electron. Lett.*, vol. 37, p. 858, 2001.

[12] W. Lu, Y. Jinwei, M. A. Khan, and I. Adesida *IEEE Trans. Electron Dev.*, vol. 48, p. 581, 2001.

[13] A. T. Ping, Q. Chen, J. W. Yang, M. A. Asif Khan, and I. Adesida *IEEE Electron Dev. Lett.*, vol. 19, p. 54, 1998.

[14] M. Micovic, N. X. Nguyen, P. Janke, W. S. Wong, P. Hashimoto, L. M. McCray, and C. Nguyen *Electron. Lett.*, vol. 36, p. 358, 2000.

[15] S. C. Binari, K. Ikossi, J. A. Roussos, W. Kruppa, D. Park, H. B. Dietrich, D. D. Koleske, A. E. Wickenden, and R. L. Henry *IEEE Electron Dev. Lett.*, vol. 48, p. 465, 2001.

[16] L. F. Eastman, V. Tilak, J. Smart, B. M. Green, E. M. Chumbes, R. Dimitrov, K. Hyungtak, O. S. Ambacher, N. Weimann, T. Prunty, M. Murphy, W. J. Schaff, and J. R. Shealy *IEEE Trans. Electron Devices*, vol. 48, p. 479, 2001.

[17] M. M. Wong, U. Chowdhury, D. Sicault, D. T. Becher, J. C. Denyszyn, T. G. Zhu, M. Feng, and R. D. Dupuis *Electron. Lett.*, vol. 38, p. 428, 2002.

[18] Y. Yamashita, A. Endoh, M. Higashiwaki, K. Hikosaka, T. Mimura, S. Hiyamizu, and T. Matsui *Japan. J. Appl. Phys., Part 2*, vol. 39, p. L838, 2000.

[19] Y. Yamashita, A. Endoh, K. Shinohara, M. Higashiwaki, K. Hikosaka, T. Mimura, S. Hiyamizu, and T. Matsui *IEEE Electron Dev. Lett.*, vol. 22, p. 367, 2001.

[20] K. Shinohara, Y. Yamashita, A. Endoh, K. Hikosaka, T. Matsui, T. Mimura, and S. Hiyamizu *IEEE Electron Dev. Lett.*, vol. 22, p. 507, 2001.

[21] K. Hikosaka, S. Sasa, N. Harada, and S. Kuroda *IEEE Electron Dev. Lett.*, vol. 9, p. 241, 1988.

[22] K. R. Hofmann, A. Lepore, H. Lee, M. Levy, E. Kohn, and A. Zlotnicka p. 381, 1989. 14th International Conference on Microlithography/Microcircuit Engineering 88 Vienna, Austria 20-22 Sept. 1988 Microelectron. Eng. (Netherlands).

[23] L. D. Nguyen, P. J. Tasker, D. C. Radulescu, and L. F. Eastman *IEEE Trans. Electron Dev.*, vol. 36, p. 2243, 1989.

[24] L. D. Nguyen, D. C. Radulescu, P. J. Tasker, W. J. Schaff, and L. F. Eastman *IEEE Electron Dev. Lett.*, vol. 9, p. 374, 1988.

[25] A. N. Lepore, H. M. Levy, R. C. Iiberio, P. J. Tasker, H. Lee, E. D. Wolf, L. F. Eastman, and E. Kohn *Electron. Lett.*, vol. 24, p. 364, 1988.

[26] P. C. Chao, P. M. Smith, K. H. G. Duh, J. M. Ballingall, L. F. Lester, B. R. Lee, A. A. Jabra, and R. C. Tiberio p. 410, 1987. 1987 International Electron Devices Meeting, IEDM. Technical Digeset, Washington DC, USA 6-9 Dec. 1987 New York, NY, USA IEEE.

[27] U. K. Mishra, S. C. Palmateer, P. C. Chao, P. M. Smith, and J. C. M. Hwang *IEEE Electron Dev. Lett.*, vol. EDL-6, p. 142, 1985.

[28] P. J. Tasker and B. Hughes *IEEE Electron Dev. Lett.*, vol. 10, p. 291, 1989.

[29] M. Wraback, H. Shen, J. C. Carrano, C. J. Collins, J. C. Campbell, R. D. Dupuis, M. J. Schurman, and I. T. Ferguson *Appl. Phys. Lett.*, vol. 79, p. 1303, 2001.

[30] J. Han, D. K. Ferry, and P. Newman *IEEE Electron Dev. Lett.*, vol. 11, p. 209, 1990.

[31] L. Shen, S. Heikman, B. Moran, R. Coffie, N. Q. Zhang, D. Buttari, I. P. Smorchkova, S. Keller, S. P. DenBaars, and U. K. Mishra *IEEE Electron Dev. Lett.*, vol. 22, p. 457, 2001.

[32] I. P. Smorchkova, L. Chen, T. Mates, L. Shen, S. Heikman, B. Moran, S. Keller, S. P. DenBaars, J. S. Speck, and U. K. Mishra *J. Appl. Phys.*, vol. 90, p. 5196, 2001.

[33] H. Kawai, M. Hara, F. Nakamura, and S. Imanaga *Electron. Lett.*, vol. 34, p. 592, 1998.

[34] Y.-F. Wu, D. Kapolnek, P. Kozodoy, B. Thibeault, S. Keller, B. Keller, S. Denbaars, and U. Mishra in *IEEE Twenty-Fourth International Symposium on Compound Semiconductors*, (San Diego, CA, USA), p. 431, IEEE, 1998.

[35] N. Maeda, T. Saitoh, K. Tusubaki, and N. Kobayashi *Phys. Stat. Sol. A*, vol. 188, p. 223, 2001.

[36] T. Paskova, E. M. Goldys, P. P. Paskova, Q. Wahab, L. Wilzen, M. P. de Jong, and B. Monemar *Appl. Phys. Lett.*, vol. 78, p. 4130, 2001.

[37] Y. F. Wu, S. Keller, P. Kozodoy, B. P. Keller, P. Parikh, D. Kapolnek, S. P. DenBaars, and U. K. Mishra *IEEE Electron. Dev. Lett.*, vol. 18, p. 290, 1997.

[38] A. Rizzi *presented at International Conference on Nitride Semiconductors 4, Denver, CO*, 2001.

[39] J. P. Ibbetson, P. T. Fini, K. D. Ness, S. P. DenBaars, J. S. Speck, and U. K. Mishra *Appl. Phys. Lett.*, vol. 77, p. 250, 2000.

[40] R. Vetury, *Polarization Induced 2DEG in AlGaN/GaN HEMTs: On the origin, DC and transient characterization*. Ph.d. dissertation, University of California, Santa Barbara, 2000.

[41] R. Coffie, D. Buttari, S. Heikman, S. Keller, A. Chini, L. Shen, and U. K. Mishra *submitted to Electron Dev. Lett.*, 2002.

6 Future Work

IN this chapter, the future work suggested in the previous chapters is summarized. In addition, some further work is suggested, which is not directly related to AlGaN/GaN HEMTs, the focus of this dissertation, but is still of scientific interest.

6.1 Fe Doping

Ferrocene was found to be an efficient precursor for Fe doping of GaN, capable of rendering GaN films on sapphire highly insulating. A slow doping response was observed, shown to be related to Fe surface segregation, or possibly Fe diffusion. To conclusively determine the role of Fe diffusion, if any, annealing studies of Fe doped samples need to be performed, followed by SIMS profiling. The anneals have to be performed for very long durations, at regular growth temperatures or above. To protect the sample surface during the anneal, the samples have to be covered with a suitable masking material, for example AlN.

It was shown that an acid etch can improve the slow Fe concentration turn-off,

but to further improve the sharpness of the turn-off, other etch techniques may be considered. On top of the desired Fe doped GaN layer, an undoped GaN sacrificial layer can be deposited (where the Fe concentration decays gradually), and be etched away with reactive ion etching, before continued growth. Alternatively, the sacrificial layer could be Fe doped, and the reactive ion etch would then have to etch through the Fe-rich surface layer, potentially causing a rough surface since the Fe compounds may not etch well in the Cl_2 etch chemistry typically used for GaN. One concern with the reactive ion etch approach is that the GaN:Fe layer will be subject to etch damage, potentially causing n-type conduction through the formation of nitrogen vacancies. However, recent etch and annealing studies of p-type GaN has showed that such effects of etch damage can be removed by annealing the sample in ammonia.[1] The heat-up of the sample for the following undoped growth would therefore serve to cure an damage incurred during the dry-etch. As for the slow turn-on, the effects of short ferrocene pre-flows need to be investigated. By depositing an appropriate amount of Fe on the sample surface before the growth of the Fe doped layer is started, it is conceivable that the turn-on can be improved.

Another interesting issue is the behavior of the Fe-rich surface layer at heterojunctions. In some of the HEMT base-layers discussed in Chapter 1.3, AlN and AlGaN layers were grown following Fe-doped GaN layers, and it is possible that they affect the 'surface riding' mechanism of the Fe. If the equilibrium ratio between surface and bulk is different for GaN and AlN, some accumulation or depletion of

Fe can be expected at the GaN/AlN interface. It is thus a possibility that an AlN layer can block a Fe surface layer from 'riding' further up in the growth structure. Some initial SIMS measurements indicate that AlN *does not* block the Fe, but due to the depth of the structure in the sample, the resolution was poor (see §2.3.3), and more measurements are needed to clarify the role of the AlN layer. The possible accumulation of Fe, or other similarly behaving dopants, at a heterojunction, can be of interest for ferromagnetic structures.

The electrical activity of the Fe impurity in GaN was investigated in a Si-Fe co-doping experiment, and the compensating activity of Fe was found to be 34%. Analogous to Mg doping of GaN, one may suspect that hydrogen passivation is the reason for the electrical activity of less than one. The samples in the co-doping study need to be annealed in a hydrogen free environment, similar to the $\sim 900^{\circ}$C activation anneal in N_2 for GaN:Mg, to determine whether hydrogen passivation plays a role in GaN:Fe.

When drawing band diagrams of structures involving GaN:Fe layers, one important piece of information is still missing: the position of the Fermi-level in semi-insulating Fe-doped GaN. The Fermi-level in the semi-insulating material is pinned somewhere relatively deep inside the band-gap, at a level governed by the Fe impurity levels. Transition metals like Fe are known to give rise to several levels within the band-gap,[2] due to the interaction between the impurity 3d states and the s- and p-like valence levels of the host semiconductor. In photoluminescence and photo-

luminescence excitation studies the $Fe^{3+/2+}$ acceptor level has been proposed to be located 2.6 eV and 3.17 eV above the valence-band maximum, respectively.[3, 4] Independent measurements are needed to more accurately identify the energy levels, and can be performed by deep level transient spectroscopy (DLTS), and deep level optical spectroscopy (DLOS). In fact, such measurements are already underway, in collaboration with researchers at Ohio state university.

6.2 HEMT Base-Layers

The base-layer study described in §2.4.3 was inconclusive, and left some important questions unanswered. A more thorough study needs to be undertaken, with built-in redundancy to account for random processing and growth fluctuations. Of particular importance is to establish what the relation between the strain of the base-layer, and the device performance, is.

6.3 Mass-Transport Growth

Some aspects of mass-transport growth were investigated, including the dependence on annealing conditions, the mechanism, the range, and the autodoping from the mask. Some geometric aspects were not covered, specifically the depth of trenches, and the aspect ratio. In §3.6 the growth morphology in 2 μm wide trenches was examined, at various levels of Ga source-supply, determined by the distance to

a large unmasked area. The experiment should be repeated for etched trenches with higher aspect ratio, e.g. 2 μm stripes etched deeper than 0.4 μm, or 0.4 μm deep trenches narrower than 2 μm. As the aspect ratio is increased, the redistribution of material in Ga-starved regions would result in differently shaped cross-sections. To achieve narrow trenches, holographic lithography may have to be used, and to etch deeper thicker masks, or different mask materials such as SrF_2, will be necessary.

In this work mass-transport growth of only binary GaN was performed, but one can speculate about the possibility of performing mass-transport growth of alloys with In or Al, or of InN or AlN. For InGaN or InN this is an intriguing idea, since material with very low carbon contents could potentially be synthesized this was. MOCVD growth of InGaN and InN has inherent problems with carbon incorporation, due to the low deposition temperature. With mass-transport growth, or 'nano-sublimation' as it may be called, the carbon presence in the gas phase is much reduced, since the group-III source atoms no longer come attached with three methyl groups. The InGaN or InN would first have to be deposited by MOCVD, containing large carbon concentrations, and would later be annealed, causing redistribution of material through nano-sublimation. In the redistribution, a large portion of the carbon in the starting material would go into the gas-phase in the form of methane, and would not get incorporated into the new material. The nano-sublimation would thereby act as a 'nano-purification' technique. The technique has good chances of working for binary compounds, but for InGaN, where evaporation of In and Ga hap-

pens at very different temperatures, I believe it will be difficult to get an appreciable source supply of both In and Ga, while keeping the temperature low enough to enable some stability for InGaN formation. However, with the enormous possibilities for structures with high purity InGaN quantum wires and dots, the nano-sublimation technique should not be ruled out before some experiments have been performed to study the evaporation behavior of InGaN. Nano-sublimation of InN on the other hand I believe has a higher chance to work. For this material one may consider using metallic In as on-wafer source rather than InN, due to the extremely poor quality of InN deposited by MOCVD, which may prevent effective evaporation. Also, activated nitrogen may be considered as nitrogen source instead of ammonia, since the hydrogen in ammonia can decrease the stability of the deposited InN.

6.4 Non-Planar Selective Area Growth

Growth evolution studies were preformed by multiple interrupted growths, a cumbersome and time consuming technique. In the GaAs and InP material systems, a much simpler technique has been used, involving marker layers, consisting of alloys, typically AlGaAs and InGaAs. For the nitrides, Si-doping could be used to mark layers, if a dopant selective wet-etch can be developed. Photo-electrochemical (PEC) etching is know to be sensitive to the conductivity type, and for properly optimized etch conditions, a working stain-etch can probably be devel-

oped. Mg doping, or Fe doping, can not be used to mark layers, due to their slow doping response. However, it would be possible to dope the entire structure with either of these dopants, and co-dope with Si in the marker layers, to create stronger conductivity contrasts between the marker layers and the layers in between.

6.5 Doping of Selective Area Growth

The doping of the various selective area growth techniques was either performed by actively supplying Si in the gas phase, or by autodoping from the SiO_2 mask. High doping levels were achieved, particularly for mass-transport growth, but for ohmic contact applications it is desirable to increase the n-type doping even more. High concentrations of Si tends to lead to rough morphology and faceting. Oxygen on the other hand, also an n-type dopant, is believed to have less morphology problems at high concentrations. The non-planar nature of the regrowth may favor oxygen incorporation, compared to planar growth of c-plane GaN, due to the expected strong doping anisotropy. Therefore, oxygen doping using O_2 as precursor is proposed to increase the n-type doping during selective area growth.

6.6 Current Transport from Regrowth into HEMT Channel

Before any further device work is performed, the current transport from regrowth region into the device channel needs to be optimized. In the present work, the channel conductivity near the regrowth edge would sometimes be degraded, related to processing details, severely limiting current transport into the device channel. Rather than characterizing the degradation electrically, which requires additional fabrication steps, cathodoluminescence (CL) microscopy is proposed as a tool to study the quality of the HEMT 2DEG. By characterizing samples with CL after each processing step, and by varying the process, the source of the damage can be identified. On a finer scale, associated with the vertical regrowth interface, the transport properties may also be non-ideal, and will have to be characterized by electrical test structures. The characterization include measuring the conductivity of thin slices of material, running parallel to the regrowth edge, as described in §4.6 and §5.6, as well as measurements across the vertical regrowth interface, as detailed in §5.6. For characterizing the structural properties of the vertical regrowth interface, transmission electron microscopy (TEM) may be used.

6.7 Ohmic Contacts

For future work on ohmic contact regrowth, the non-ideal transport from the regrowth into the HEMT channel needs to be addressed, as outlined in the previous section. In parallel with that, the metallization scheme, and the contact fabrication procedure, needs to be optimized with respect to reproducibility and performance. For regrown contacts, the structure of the regrown regions typically consists of an n^+-GaN region, with an optional cap layer. The contact metallization is best optimized on planar structures, grown to mimic the regrowth layer structure. Along with the metallization optimization, the epi-layer structure can be optimized, both with respect to contact resistance, and to lateral sheet conductance.

The use of mass-transport growth for ohmic contact formation was demonstrated, with a contact resistance down to 0.3 Ωmm. Apart from active oxygen doping, as mentioned previously, what needs to be studied next is the SiO_2 mask layout, and the geometry of the etch. A small fill-factor was used in all but one experiments, and was found to give better ohmic contacts. No effort was made to optimize the detailed layout, including aspects such as distance to open areas, size of open areas, and etch depth.

After optimization of the contact resistance, the obvious step will be to fabricate a device, with an e-beam gate closely aligned to the source regrowth edge. Testing the device will show if device characteristics such as soft current saturation, high

knee voltage, g_m compression, and low f_T, are improved, as was the intention of the regrowth.

6.8 Hot Electron HEMT

Further work on the hot electron HEMT needs to be postponed a few years, until reliable contact regrowth procedures exist, and f_T of devices has been maximized by eliminating the parasitic resistances. Once the work is continued, a few things should be different from the device fabricated in this work. The starting material should be a standard HEMT, with the lowest possible sheet-resistance, on a semi-insulating GaN base-layer. The 5% AlGaN base-layer used in the present device resulted in a high drain resistance, and a higher-than-usual sheet resistance. A shorter source to drain spacing, in combination with a low sheet resistance, and low contact resistances, will serve to minimize the parasitic source and drain resistances. Also, devices with several different Al compositions, and several Si doping levels (including zero), in the source regrowth, should be fabricated to find the optimum combination.

As was clear from the attempt to draw the band diagram of the device at the regrowth/channel interface, a simulation of the device is needed. Our current simulation software from Silvaco does not include solving of the Schrödinger equation, which is necessary in this type of device. However, if the device is to be pursued, one may consider acquiring the appropriate software to allow accurate device modelling.

References

[1] Y. T. Moon, D. J. Kim, J. S. Park, J. T. Oh, J. M. Lee, and S. J. Park *presented at 11th International Conference on Metal-Organic Vapour Phase Epitaxy, Berlin, June 3-7*, 2002.

[2] L. A. Hemstreet *Phys. Rev. B*, vol. 22, p. 4590, 1980.

[3] J. Baur, K. Maier, M. Kunzer, U. Kaufmann, J. Schneider, H. Amano, I. Akasaki, T. Detchprohm, and K. Hiramatsu *Appl. Phys. Lett.*, vol. 64, p. 857, 1994.

[4] R. Heitz, P. Maxim, L. Eckey, P. Thurian, A. Hoffmann, I. Broser, K. Pressel, and B. K. Meyer *Physical Review B*, vol. 55, p. 4382, 1997.